

A MODEL OF SHORT TERM SURFACE DEFORMATION OF
SOUFRIERE HILLS VOLCANO, MONTSERRAT
CONSTRAINED BY GPS GEODESY

by

ERIN ELIZABETH MCPHERSON


Presented to the Faculty of the Graduate School of
The University of Texas at Arlington in Partial Fulfillment
of the Requirements
for the Degree of

MASTER OF SCIENCE IN GEOLOGY

UNIVERSITY OF TEXAS AT ARLINGTON

August 2013

Copyright © by Erin Elizabeth McPherson 2013

All Rights Reserved 

Acknowledgements

First of all, I would like to thank Dr. Glen Mattioli for all of his wisdom, guidance and support during this process. I would also like to thank Dr. Merlynd Nestell and Dr. Ashley Griffith for their mentorship as members of my graduate committee. Their support and advice helped to make this project possible. To the members of the Fort Worth Geological Society, financial support of this project was greatly appreciated.

Throughout my academic journey, Dr. Merlynd Nestell and Dr. Galina Nestell have provided me so much support, both personally and academically, and taught me to always strive for excellence, and to accept challenges and always believe that anything is possible if you believe in yourself. I will be eternally grateful for their wisdom, guidance and friendship.

Thanks also go out to Professor Jamie Miller, who later became a trusted friend and colleague. She is one of the first professors to show me that my interest in rocks and minerals and the processes of the earth could be turned into a lifelong career that I have loved from day one.

Without a solid personal support system, academic achievement, especially as a non-traditional student, is almost impossible. I would like to extend my thanks to my friends and colleagues: Cathina Gunn de Rosas, Taylor Hughlett, Lisa Moran, Christina Munoz, Angie Osen, and many more for their support and friendships. My gratitude for the years of phone calls, emails, text messages, study sessions, and their constant encouragement cannot be expressed enough.

Lastly, I would like to thank the members of my family. I absolutely could not have done this without your constant love and support. As a wife and a mother, academic endeavors constantly conflict with family time and obligations. More often than not, school had to be prioritized over family time. Many thanks to my son, Riley, for putting up with the phrase "Mommy is really busy baby, I am sorry" and my husband, Mark, who pushed me to go for my dreams. Their sacrifice of family time and unconditional support helped make my academic success possible. Thank you for always believing in me even when I had trouble believing in myself. Your love is what kept me strong through this whole process.

And for my parents, Patricia Harris and Dace McPherson, they taught me to always fight for my dreams and to never dream small. Their unwavering belief in me and what I could accomplish helped keep my head above water, especially when I had my own doubts.

To all my extended family, I thank you from the bottom of my heart for the help you have provided; the babysitting, the shoulder to lean on, the ears to listen to my complaints and your constant encouragement. To you all I owe so much.

July 2, 2013

Abstract

A MODEL OF SHORT TERM SURFACE DEFORMATION OF SOUFRIERE HILLS VOLCANO, MONTSERRAT, CONSTRAINED BY GPS GEODESY

Erin Elizabeth McPherson, M.S.

The University of Texas at Arlington, 2013

Supervising Professor: Glen S. Mattioli

Geodetic surveying is a core volcano monitoring technique. Measurements of how the crust deforms can give valuable insight into the mechanisms and processes that drive an eruption, and the way in which they change (Odbert et al., 2012). Campaign and continuous GPS geodetic measurements on Soufrière Hills Volcano, Montserrat are reported here from 1995 to 2010, spanning three dome growth and repose episodes extending the results of Mattioli et al. (2010). Soufriere Hills Volcano (SHV), Montserrat, in the Lesser Antilles island arc, became active in 1995, and for nearly two decades, geodetic surveys have been conducted using both continuous and campaign GPS observations. Data have been collected and processed using the latest and most advanced geodetic instruments and techniques available. The NSF-funded CALIPSO and SEA-CALIPSO projects have allowed for some of the most in depth studies of the ongoing SHV eruptions to date, and many models for surface deformation and magmatic chamber configuration have resulted (Voight et al., 2013).

I focus on data gathered from the early stages of the SHV eruption in 1996 through the end of 2010 from two continuous GPS sites, Hermitage Peak (HERM – located ~1.6 km from the vent) and Montserrat Volcano Observatory 1 (MVO1– located ~7.6 km away from the vent). These data have been reprocessed using GIPSY-OASIS II (v. 6.1.2) with final, precise IGS08 orbits, clocks, and earth orientation parameters using an absolute point positioning (APP) strategy. The study is being conducted to re-examine spatial and temporal changes in surface deformation, constrained by GPS, and to better illuminate the short term (*i.e.* sub-daily to weekly) deformation signals noted amongst the longer, cyclic

deformation signals (*i.e.* monthly to annually) that have been previously reported and modeled. In addition, I have extended the time series for HERM and MVO1 to the end of 2010, beyond what has been previously analyzed and published by Mattioli et al. (2010). The reprocessed time-series show lower variance for daily APP solutions over the entire temporal data set; trends in the long-term inflation and deflation patterns are generally similar to those previously published (*e.g.* Elsworth et al., 2008; Mattioli et al., 2010; Odbert et al., 2012), but now superimposed, shorter term signals are more clearly visible.

Table of Contents

Acknowledgements	iii
Abstract	v
List of Figures	ix
List of Tables	xi
Chapter 1 Introduction.....	1
1.1 Background	1
1.2 Geologic and Tectonic Setting	2
1.2.1 Caribbean Plate	2
1.2.2 Lesser Antilles	6
1.2.3 Soufriere Hills Volcano, Montserrat	9
1.2.4 The CALIPSO Project	11
Chapter 2 Methods.....	16
2.1 Data Acquisition.....	16
2.2 Data Processing and Analysis.....	19
2.2.1 GD2P.PL Perl Script	20
2.2.2 GIPSY-OASIS Processing Version 6.1.2.....	21
Chapter 3 Previous Deformation Models	23
3.1 Voight et al. (1999) Model	23
3.2 Denlinger and Hoblitt (1999) Model.....	28
3.3 Mattioli et al. (1998) Dike Emplacement Model.....	32
Chapter 4 Results	33
4.1 A Damping Effect.....	35
4.2 Secondary Short Term Deformation Signal.....	41
4.3 A “Hitch” in the Cycle.....	48
4.4 New Site Velocities	56

4.5 HERM - A model of deformation due to dike emplacement	58
4.6 Reprocessing using GOA-II (ver.6.2)	69
Chapter 5 Conclusions	75
Appendix A GOA-II (Ver. 6.1.2) Time Series	77
Appendix B GOA-II (Ver. 6.2) Time Series	87
References	91
Biographical Information	99

List of Figures

Figure 1 Caribbean Plate Seismicity Map.....	4
Figure 2 New model of the tectonic setting of the northern Caribbean	5
Figure 3 Lesser Antilles.....	7
Figure 4 Topographic map of Montserrat.....	10
Figure 5 Montserrat GPS site location map.....	14
Figure 6 Cyclic CP2 tilt time series.....	25
Figure 7 Proposed chamber geometry of SHV.....	26
Figure 8 Simplified view of Voight et al. (1999) model.....	27
Figure 9 Conduit Model.....	29
Figure 10 Flux Rates and resulting cycle shapes.....	31
Figure 11 Time series for continuous site BGGY site processed using GIPSY (ver. 4.0).34	
Figure 12 Time series for continuous BGGY site reprocessed using GIPSY (v. 6.1.2). ..	34
Figure 13 MVO1 period and amplitude of long term deformation.....	36
Figure 14 Apparent Flux Rate vs. Time	37
Figure 15 Elsworth et al. (2008) flux rates	38
Figure 16 Short term signal periods and amplitudes	42
Figure 17 Short term, Voight et al. (1999) stick-slip correlation.....	47
Figure 18 MVO1 "hitch".....	49
Figure 19 First hitch episode.....	51
Figure 20 Second hitch period.....	52
Figure 21 Third hitch period.....	53
Figure 22 Dike Emplacement Hypothesis.....	59
Figure 23 Horizontal Displacement Vectors for dike opening 1 meter	61
Figure 24 Vertical Displacement	62
Figure 25 Vertical Displacement Vectors in 3D view	63
Figure 26 Horizontal view of Vertical Displacement vectors.....	64

Figure 27 Vertical Displacement Wire Frame Drape	64
Figure 28 Horizontal Displacement Vectors for 3 meter dike opening	65
Figure 29 Vertical Displacement	66
Figure 30 Vertical Displacement Vectors	67
Figure 31 Horizontal View of Vertical Displacement Vectors.....	68
Figure 32 Vertical Displacement Wire Frame Drape	68
Figure 33 Possible Third Deformation Signal	71
Figure 34 Possible Third Deformation Signal (2).....	72
Figure 35 Possible Third Deformation Signal showing little variation	73
Figure 36 Possible third signal at MVO1 correlated with signal at BGGY	74
Figure 37 HERM time series in GOA-II (ver. 4.0).	78
Figure 38 HERM time series processed with GOA-II (v. 6.1.2).	79
Figure 39 Extended HERM time series reprocessed with GOA-II (v. 6.1.2).....	80
Figure 40 MVO1 time series processed in GOA-II (ver. 4.0).....	81
Figure 41 MVO1 time series reprocessed in GOA-II (ver. 6.1.2).....	82
Figure 42 Extended time series for MVO1 site reprocessed using GIPSY (ver. 6.1.2). ...	83
Figure 43 Time series for continuous BGGY site reprocessed using GIPSY (ver. 4.0). ..	84
Figure 44 Time series for BGGY site reprocessed using GIPSY (ver. 6.1.2).....	85
Figure 45 Extended time series for BGGY site reprocessed using GIPSY (ver. 6.1.2)....	86
Figure 46 BGGY time series in GOA-II (ver. 6.2) with ambiguities.....	88
Figure 47 MVO1 time series in GOA-II (ver. 6.2) with ambiguities	89
Figure 48 HERM time series in GOA-II (ver. 6.2) with ambiguities	90

List of Tables

Table 1 Soufriere Hills Volcano GPS sites.....	15
Table 2 Period and amplitudes for the three cycles.....	40
Table 3 Short Term deformation period and amplitudes.	43
Table 4 Deflation “hitch” approximations	48
Table 5 Site velocities for ITRF05 and IGS08 processing.	57

Chapter 1

Introduction

1.1 Background

Since the early 1990s, Global Positioning System (GPS) geodesy has become common in volcano monitoring because of its high precision, relatively low cost, and ease of use in even the most challenging field environments (Dzurisin, 2007). Geodetic studies of ground deformation in volcanic areas include the construction of models to help constrain parameters such as locations, geometry, and pressure changes of crustal deformation sources. Deformation modeling has advanced from the revolutionary approaches of Anderson (1936) and Mogi (1958) to models accounting for complex source geometries; a recent review by Poland et al., (2006) discusses many of these models. Since activity began in July 18, 1995, the Soufriere Hills Volcano (SHV) has been studied with many ground breaking technologies, making it one of the most prolifically studied volcanoes in the world. The 1995 to present eruption of SHV on Montserrat has been, in many respects, an ordinary example of a Peléan dome eruption (Wadge et al., 2006) and many techniques have been used prior to and during the current eruptive episode on Montserrat to study and thus model surface deformations, and chamber configuration.

One of the advantages of Global Positioning System (GPS) geodesy over traditional survey methods is that data collection and analysis can be automated and thus only limited human involvement on active volcanoes is required. The initial GPS sites located on SHV were selected due to ease of access, horizontal distance (0.8 to 3.6 km) to the active vent, and their azimuthal distribution around the Soufriere Hills Volcano. Because GPS data can be linked to external reference frames, well outside of the active volcanic zone, satellite geodesy can provide unique constraints for modeling complex surface deformations (Mattioli et al., 1998). Using additional geodetic techniques in the CALIPSO project and up to date GPS and InSAR data, the understanding of the magmatic system underneath the island and surface deformation that has occurred at SHV is un-paralleled. Long term surface deformation of SHV has been modeled by many authors over the past nearly two decades, but this study will focus on the short term deformations noted at two sites, HERM and MVO1, located 1.6 and 7.6 km from SHV,

respectively. These deformations occur over time periods ranging from hours to days to a few weeks. The short term deformations recorded on this volcano have been noted in earlier research but never modeled. Some of these deformation signals, at the most proximal GPS site to the vent, HERM, when examined in detail do not follow the longer term cyclic cycles seen in the data collected from other, more distal GPS sites located on SHV. The data collected at these sites are due in part to non-eruptive activity occurring within the volcanic edifice and modeling these data could lead to a better understanding of surface and volcanic loading, as well as magma movement that occurs in the upper conduit of a volcano at the beginning of an eruption phase. The purpose of the models, used for comparison in this study, are to try and determine if the observed surface deformation could be due to a non-effusive dike emplacement below the vent, or possibly to a magmatic stick-slip occurring along the walls of the upper conduit.

1.2 Geologic and Tectonic Setting

1.2.1 Caribbean Plate

The geology of the Caribbean is both complex and varied, as the Caribbean plate is typified as an anomalously thick sequence of oceanic crust (Draper et al., 1994), with a thickness ranging from between 12 to 15 km, which is much greater than the typical 6 km ocean basin crustal thickness (Fox and Heezen, 1975). The present Caribbean Plate is thought to have formed from the Farallon-Phoenix-Pacific triple junction between 136 and 130 Ma (Ghosh et al., 1994), during the spreading of the North and South American Plates. Most Caribbean tectonic models show the approximate configuration of the present day plate boundaries being established during the Miocene (Mann et al., 1990). The major crustal boundaries were determined from refraction data and overlying sediment thicknesses were determined by seismic reflection data. The thickened area of the Caribbean can be compared to western Pacific plateaus, like Manihiki and Ontong Java, which are similar in scale and age (Mann et al., 1990), and this may help partially explain why the Caribbean is somewhat unusual among the tectonic plates (Sykes et al., 1982).

The present day boundaries of the Caribbean Plate were originally roughly defined by the distribution of seismic activity (Sykes and Ewing, 1965; Molnar and Sykes, 1969). It was at first thought that the northern boundary of the Caribbean was a single boundary with the North American plate and a

single southern boundary in contact with the South American plate. Several studies (see Jansma et al. (2000), Jansma and Mattioli, (2005), and Manaker et al. (2008)) have suggested that microplates occur between the North American and Caribbean plates. The most current study, done by Benford et al. (2012), uses a more spatially dense velocity field to better constrain the microplate boundaries west of Puerto Rico and the Virgin Islands. Benford et al. (2012) used elastic block modeling of 126 GPS site velocities from Jamaica, Hispaniola, Puerto Rico and other islands in the northern Caribbean to test for the existence of a Hispaniola microplate and estimate angular velocities for the Gônave, Hispaniola, Puerto Rico-Virgin Islands and two smaller microplates relative to each other and the Caribbean and North America plates. From the derived angular velocities, their model strongly suggests that there are indeed several microplates that are between the North American plate and the Caribbean plate (Figure 2). Similar studies have been done on the southern boundary of the Caribbean plate, to determine if there could be microplates situated between the Caribbean and South American plates as well. While these studies have not been completed yet, it is quite possible that microplates occur along this boundary zone as well. The eastern boundary of the Caribbean plate is in contact with oceanic crust of both the North and South American plates, while the western boundary is oceanic crust of the Cocos plate. Very generalized plate boundary tectonic configurations are as follows: Dextral and sinistral strike-slip motion with localized extension characterizes the southern and northern boundaries, respectively (Burke, 1988; Bird et al., 1993). It is very difficult to give an accurate and simple representation of the tectonics that occurs along the Northern boundary due to the microplate configuration and its complexity. Eastern and western boundaries are subduction zones where the Caribbean Plate is being under-thrust by the oceanic crust of the North and South American plates and the Cocos Plate, respectively.

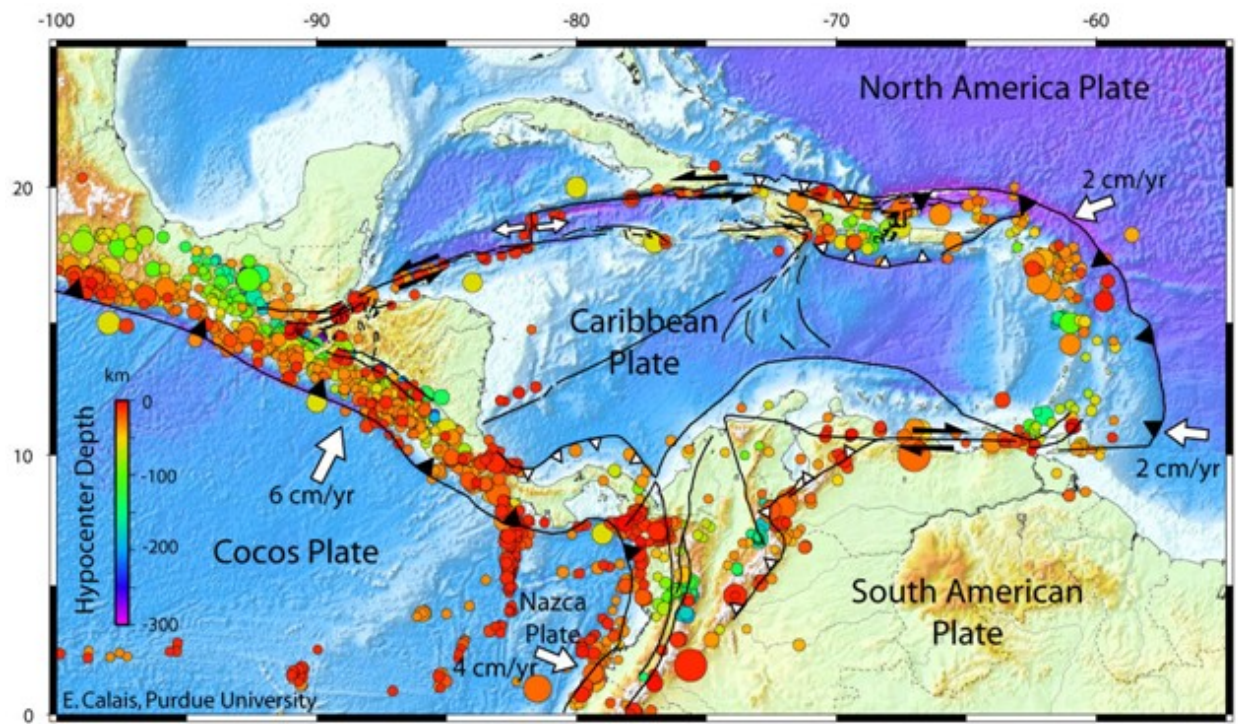


Figure 1 Caribbean Plate Seismicity Map

Caribbean plate boundaries showing the Cocos, Nazca, and North and South American plates. Earthquakes from 1900 to Present with known faults, topography, and bathymetry Credit: Eric Calais, Purdue University

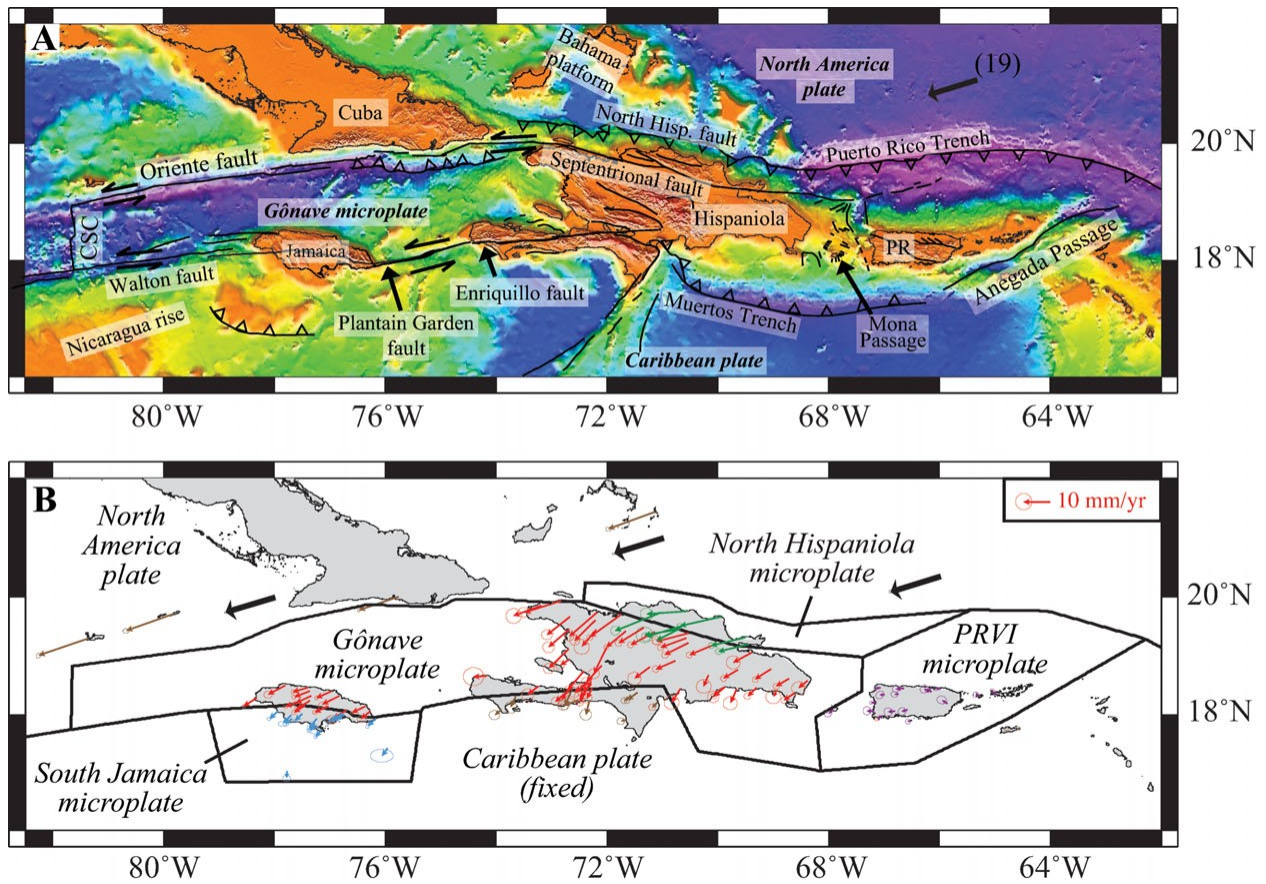


Figure 2 New model of the tectonic setting of the northern Caribbean (Benford et al., 2012).

Bold black arrows in panels (a) and (b) show MORVEL estimate of North America plate motion in mm yr^{-1} relative to the Caribbean plate (DeMets *et al.* 2010). CSC, Cayman spreading centre; PR, Puerto Rico. Two-minute seafloor bathymetry and land topography are from Sandwell & Smith (1997). (b) GPS site velocities relative to Caribbean plate, with 1σ , 2-D error ellipses. Velocities from Hispaniola are taken from Calais *et al.* (2010); velocities for PRVI are from Jansma and Mattioli (2005). Velocities are color-coded based on plate. Scale is shown in upper right corner. Black lines mark plate boundaries used for the analysis. All plates included in the analysis are labeled, PRVI microplate, Puerto Rico-Virgin Islands microplate.

1.2.2 Lesser Antilles

The Lesser Antilles Island Arc spans north to south from the island of Sombrero to the island of Grenada and is separated from the Greater Antilles by the Anegada Passage in the north and by the Venezuela continental margin, which begins just south of Grenada and is the result of westward subduction of oceanic crust of the North and South American plates beneath the Caribbean Plate (Wadge, 1994). The Lesser Antilles has been described as a true island arc: thus the islands are built largely by volcanism above a subduction zone (Tomblin, 1975), and also as a double arc (Fink et al., 1972). Arcuate in shape and convex eastward, the island arc is approximately 850 km long and subtends an angle of nearly 90° (Wadge and Shephard, 1984). North of Martinique, the island arc bifurcates into eastern and western segments. The eastern segment is referred to as the Limestone Caribbees and includes from north to south: Sombrero, Anguilla, St. Martin, Barbuda, Antigua, Desirade, and Marie Galante. These islands have not been volcanically active since the Oligocene and are capped by younger Cenozoic limestone (Draper et al., 1994), with the oldest volcanic rocks being Late Cretaceous in age.

In the Limestone Caribbees the ages of the exposed rocks increases as you move northward (Wadge, 1984), which implies that the change in the arc from the Limestone to the Volcanic Caribbees began in the north and propagated southward through time. The greatest distance separating the eastern and western segments of the Lesser Antilles is at a maximum distance in the north, reinforcing that idea that the divergence in the forearc began in the north and propagated south. It is unclear whether the separation is a result of extension within the upper plate or a westward migration of the subduction zone. A 10 My volcanically quiet period between the Oligocene and Miocene separates the Limestone Caribbees eastern arc from the volcanic active Volcanic Caribbees arc in the west (Wadge, 1984).

The western arm of the northern Lesser Antilles, along with the southern Lesser Antilles, are known as the Volcanic Caribbees. The Volcanic Caribbees are the active island arc and are the surface representation of rising magma that is being produced as the North and South American plates are being subducted beneath the overriding Caribbean plate. From north to south the Volcanic Caribbees is comprised of the islands: Saba, St. Eustatius, St. Kitts, Nevis, Redonda, Montserrat, Guadeloupe, Les Saintes, Dominica, Martinique, St. Lucia, St. Vincent, Bequia, Carriacou, and Grenada. The exposed

volcanic rock from Martinique and continuing south, date back to the Eocene, whereas, the oldest volcanic rock exposed in the northern portion of the Volcanic Caribbees are early Pliocene to latest Miocene in age. There are no active volcanoes south of Grenada (Maury et al., 1990). Montserrat is located in the northern region of the Lesser Antilles in the Volcanic Caribbees (Figure 3).



Figure 3 Lesser Antilles

Black triangles represent the volcanoes located on the islands of the Volcanic Caribbees. Red triangle indicates Soufriere Hills Volcano, Montserrat. Modified figure from Simkin and Siebert (1994).

Changes in seismicity associated with the subducting Atlantic oceanic crust allow the subduction zone to be divided into more seismically active northern and less active southern portion. This division occurs at the 14.5° N latitude, and it has been proposed by Wadge and Shephard (1984) that the change that occurs here is due to a change in the dip of the Waditti-Benioff zone and the depth to which the seismic activity occurs (*i.e.* seismogenic zone). Using hypocenters from intermediate-depth seismicity monitored on a telemetered network of seismic stations located along the island chain, Wadge and Shephard (1984) showed that the strike of the Benioff zone changes from NNE between St. Lucia and Grenada to NNW between Martinique and Saba in the north. In recent research using improved seismic networks, a reanalysis of the Waditti-Benioff zone has been conducted that shows that the dip of the subducting slab is much more complex than originally proposed by Wadge and Shephard. Their study concluded that from 11°N to 12°N, the Benioff zone that underlies the Venezuelan continental shelf is essentially vertical; slab dip between 13°N and 14°N is 45-50°; while the northern segment, defined as north of 14°, dips at angles of 50-60°. Matson (2007), however, it showed that there was a bias in the original data at depths of 10 km and 33 km. Matson, (2007) discovered that there were numerous earthquakes with hypocenter of depths of 10 km (2792 events) and 33 km (5907 events), as well as earthquakes that had no magnitude solutions (2963 events) or magnitudes less than 3.5 (5946 events) and these were eliminated from the data set. When these events were eliminated and the new data set reevaluated and compared with the previous data set, it was observed that the Waditti-Benioff zone shows much shallower subduction than previously proposed by Wadge and Shephard (1984). Matson's study suggests near vertical 11°N to 12°N southern region at 25.27°, the 13°N and 14°N region at 37.58°, and the northern segment at 33.64°. The new cross-sections also revealed a possible kink in the subduction zone at 14.5°N latitude with the dip of the subducting slab shallowing to the north and south. This is in contradiction to the data presented by Wadge and Shephard (1984), which indicated gradual southward steepening of the subducting slab (Matson, 2007).

1.2.3 Soufriere Hills Volcano, Montserrat

The island of Montserrat is located approximately 480 km east-southeast of Puerto Rico and 48 km southwest of Antigua, and has an aerial extent is 104 km² that is currently increasing in size due to the buildup of volcanic deposits on the southeast coast. Montserrat has volcanic centers dating as old as 4.3 Ma (Roobol and Smith, 1998; Harford et al., 2002; Smith et al., 2007). These are, from oldest to youngest: the Silver Hills in the north; the Centre Hills in the center; and the active volcano of the Soufriere Hills and South Soufriere Hills in the south (Roobol & Smith, 1998; Smith et al., 2007).

The island is primarily composed of andesitic lavas and volcaniclastic rocks produced by dome-forming eruptions, remnants of andesite lava domes and brecciated previous lava domes, pyroclastic flow deposits, lahar and debris avalanche deposits, and tephra fall deposits; however, the rocks of South Soufriere Hills are of basaltic to basaltic-andesite in composition. Deposits older than 4,000 years are lithified (Roobol and Smith, 1998). There are also zones of hydrothermally altered rock and active fumarole fields that occur on the Soufriere Hills Volcano (Smith et al., 1997; Young et al., 1998)

Historical eruptions for the SHV complex show a range from 1.1 to 0.25 Ma (Harford et al., 2002), between 24 – 16 Ka (Wadge and Isaacs, 1998), 4 Ka, and 325±50 years before present date (Young et al., 1998). Prior to the current eruption cycle, the SHV complex experienced three aborted eruption events: 1897-98, 1933-37 (Macgregor, 1938; Perret, 1939), and again in 1966-67 (Sheppard et al., 1971). These events showed an increase in hot spring and seismic activity (Shepherd et al., 1971; Young et al., 1998), which were interpreted by Young et al. (1998) as 30-year cycles with each one being marked by increasing seismicity.

The SHV began to show renewed activity again in 1992, with an increase in seismic activity that was recorded by regional monitoring seismic networks on Montserrat. From 1992 through June 1995, eighteen distinct earthquake swarms were recorded in the south of the island, with the largest swarm occurring in June 1994 (Montserrat Volcano Observatory). Prior to the onset of activity in 1995, the volcanic center was comprised of five distinct dome complexes: Castle Peak, Chance's, Gage's, Galway's, and Perche's (Figure 4). Castle Peak was located inside English Crater, remnants of a

breached sector collapse that is open to the Northeast and dated to ~4 Ka (Roobol and Smith, 1998). The present and still currently active eruption cycle of SHV began on 18 July 1995 (Young et al., 1998; Mattioli et al., 1998), with phreatic explosions from east of Castle Peak, a prehistoric andesitic dome sited within the horseshoe shaped English's Crater (Norton et al., 2002).

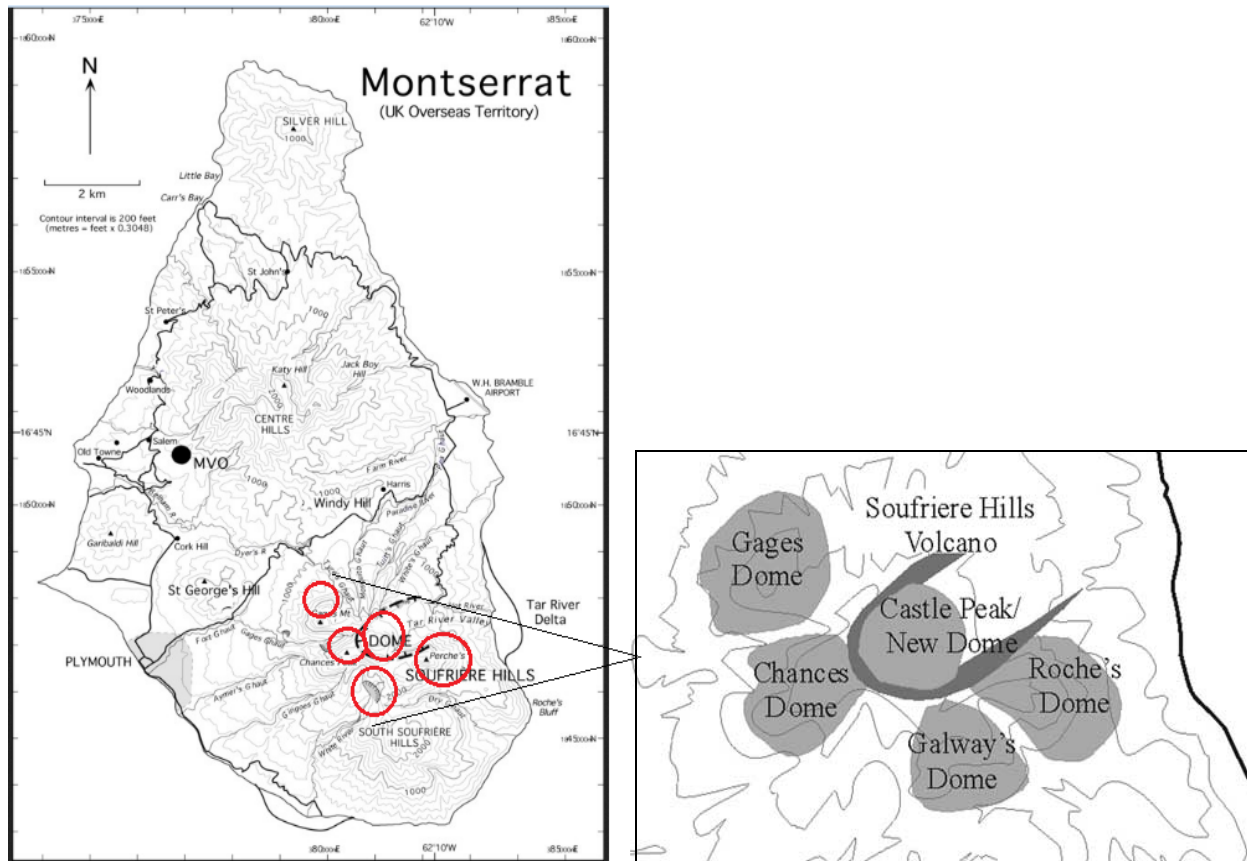


Figure 4 Topographic map of Montserrat.

Showing detailed geographical locations of volcanic domes prior to volcanic activity onset in 1995 (modified from Sparks and Young, 2002). Red circles enclose the five young domes that were present before current activity began in English Crater.

There was no increase in seismic or hydrothermal activity noted in the weeks prior to the onset of phreatic venting that began July 18, 1995, which began as multiple steam vents that were trending NNW in English Crater (Young et al., 1998). The phreatic explosions coalesced into one large vent on July 28 that created a phreatic explosion of steam, as well as an ash column that reached ~3 km in height. Three more phreatic eruptions occurred (August 21, October 31, and November 9), which covered the capital city of Plymouth, with a few millimeters of ash (Young et al., 1998). The first evidence of deep magma movement was recorded as volcano tectonic (VT) earthquakes, which showed an increase in number and were noted as occurring at much shallower depths (~6 km to the surface) from August to November of 1995 (Miller et al., 1998).

Seismic swarm periods, which were noted to occur for the same duration as the recorded surface deformation, recorded by tiltmeter data, were most commonly made up of hybrid earthquakes, and characterized by sharp onset, no identifiable S phase and having shallow foci of less than 2 km (Voight et al., 1999). Swarms began and ended abruptly and were interspaced with periods of no seismicity or of movement associated with rockfalls or pyroclastic flow due to dome collapse. The swarms started while inflations were occurring and stopped near peak inflation or when deflation began. Cycles lasted from 3 to 30 hours and were sometimes accompanied by visual dome growth and/or with spine formation, as well as enhanced degassing with non-explosive ash emissions (Voight et al., 1998). Before the first effusive emissions in late November/December 1995, there were multiple short term surface deformations that occurred. These short term deformation events were recorded at the CHPK and HERM GPS sites located ~0.8 and ~1.6 km from the SHV vent, respectively; however the CHPK site was destroyed by volcanic activity in 1996 and was not replaced due to hazardous conditions (Mattioli et al., 1998).

1.2.4 The CALIPSO Project

The ongoing eruption of the SHV, Montserrat has been exceptional for a number of reasons. Firstly, this eruption has been unusually long-lived. Whereas the median eruption duration for andesitic volcanoes is two to three years, the longevity of the SHV eruption ranks within the top 4% for all recorded dome-building eruptions (Odbert et al., 2012). The longevity of the MVO eruption enabled scientist from

around the world to study this volcano in greater depth than any other active andesitic eruption before. A major part of this study was performed under a project called CALIPSO, the Caribbean Andesite Lava Island Precision Seismo-geodetic Observatory. This was a collaborative project involving PIs from four U.S. institutions working together with the Montserrat Volcano Observatory (MVO) and scientists from two United Kingdom institutions. In November of 2002 installation of four 200 m deep boreholes around Soufriere Hills Volcano began, with drilling and instrument installation completed in late February 2003 (Mattioli et al., 2004). CALIPSO's purpose is to investigate the dynamics of the entire SHV magmatic system using an integrated array of specialized instruments in four strategically located boreholes in concert with several shallower holes and surface sites. The project was unique, as it represented the first, and at the time of emplacement, the only such borehole volcano-monitoring array deployed at an andesitic stratovolcano.

The sensor package at each CALIPSO site includes four instruments: a single-component, very broadband Sacks-Evertson dilatometer; a three-component seismometer designed by Duke/Carnegie Institution of Washington (~Hz to 1 kHz); a Pinnacle Technologies series 5000 tiltmeter, which consequently, all failed to work properly; and a surface Ashtech u-Z CGPS Continuous Global Positioning System (CGPS) station with choke ring antenna, precision Southern California Integrated GPS Network (SCIGN) mount, and tall radome (Mattioli et al., 2004). The Ashtech u-Z receivers were replaced with Trimble NetRS receivers in 2007 (Mattioli et al., 2010). The CALIPSO project instruments were integrated into the ongoing surface monitoring (seismic, geodetic, and gas) networks of the Montserrat Volcano Observatory and were used to track in near real-time the processes that occurred in and about the magma reservoir and its associated conduit system. The CALIPSO borehole instrumentation reduced noise and allowed for the ability to locate effective stations farther from the volcano than possible with surface instruments, and both features aid the sampling of both seismic and deformation signals from the deep transport, storage, and recharge systems. The borehole sites were selected at azimuths and distances to maximize scientific return, with some field adjustments required from preliminary plans because of changes in volcanic hazard zonation, and perceived needs to access line power and drill water (Mattioli et al., 2004).

In 2003, the CALIPSO project enhanced the GPS infrastructure at SHV, from the original six GPS sites with the installation of four more sites (Mattioli et al., 2004). The four new sites were installed at Air Studio (AIRS, ~5.2 km), Gerald's Yard (GERD, ~9.6 km), Olveston (OLVN, ~6.9 km), and Trants (TRNT, ~6.2 km, Figure 5). Between October 2008 and June 2009, the original six MVO-operated cGPS sites (HARR, HERM, MVO1, SOUF, SPRI, and WTYD) were upgraded with Trimble NetRS receivers. Trimble Zephyr Geodetic antennas have been phased-in to replace the choke ring antennas, but monuments have remained largely unchanged except for the few various times throughout the eruption, when the original equipment deployed in the field was damaged or destroyed by volcanic activity (Odbert et al., 2012).

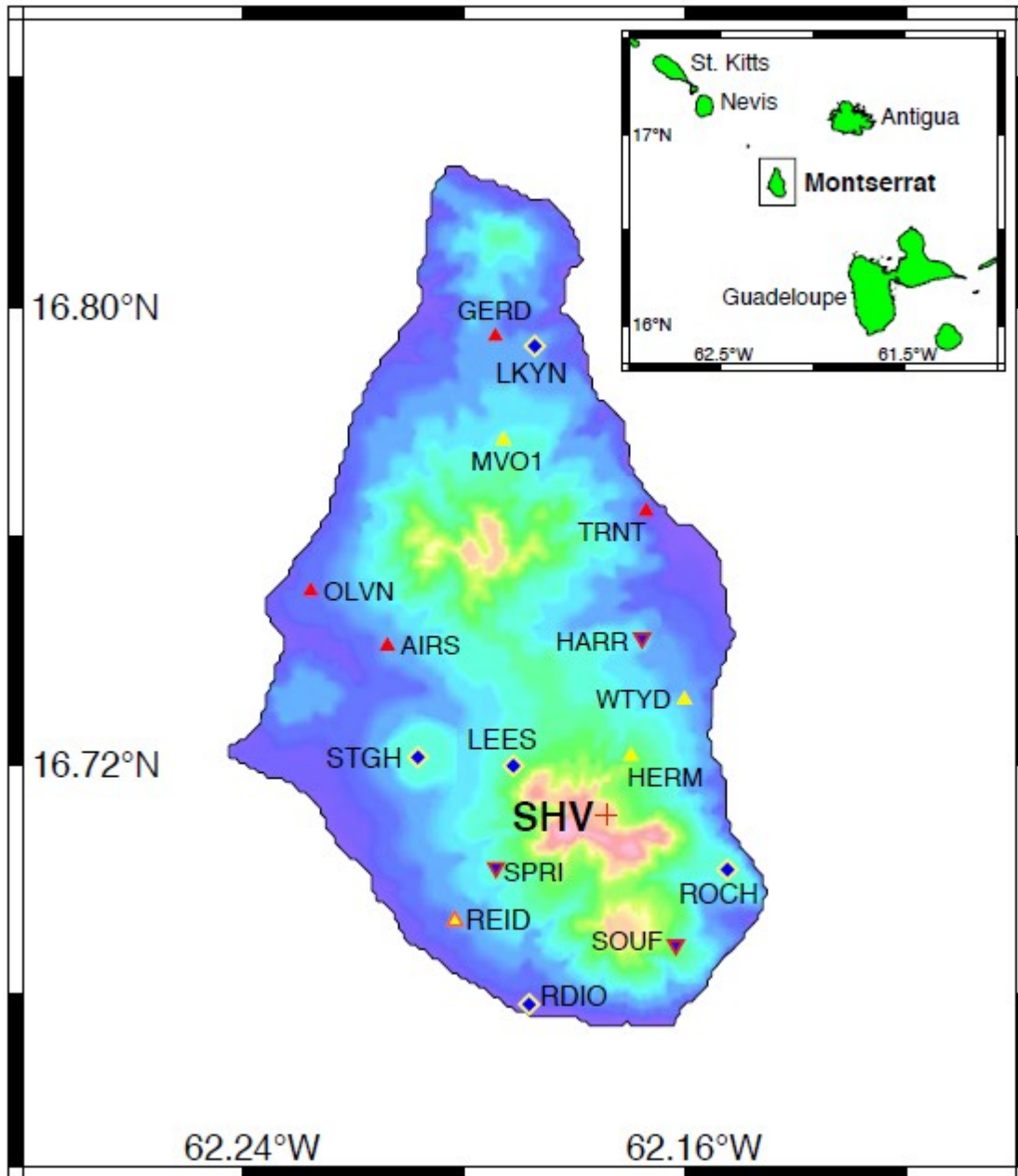


Figure 5 Montserrat GPS site location map.

Insert map shows location of Montserrat relative to other islands in the northeastern Caribbean. Sites are superimposed on digital elevation map created from GTOPO30 data. The approximate location of the vent and center of mass of andesite domes of Soufriere Hills Volcano is marked as a red cross labeled SHV. GPS sites are coded by type, with campaign sites shown as blue diamond with yellow outlines. These sites were abandoned after NOV 1999. Continuous sites are shown as upright or inverted triangles and are color coded based on receiver type and agency/project under which they were originally installed. Sites used in this study are marked by upright yellow triangles (HERM, MVO1 and were installed by UPRM with NASA funding in mid-1996 and were rehabilitated in early 1998 and deployed Trimble 4000SSi receivers. Figure modified after Mattioli et al. (2010).

Table 1 Soufriere Hills Volcano GPS sites -Modified from Odbert et al., (2012).

ID	Name	Location (WGS84)	Date	Equipment
AIRS	Air Studios	62.2139°W, 16.7408°N	2003	Trimble NetRS Receiver/ Ashtech Dorne Margolin CR Antenna +D
<i>BROD</i>	<i>Broderick's</i>	<i>62.2089°W, 16.6929°N</i>	<i>19 Nov 2009</i>	<i>Ashtech UZ-12 Receiver/ Leica AT504 CR Antenna</i>
<i>(CHPK)</i>	<i>Chances Peak</i>	<i>62.18°W, 16.71°N*</i>	<i>1995 (Aug '97)</i>	<i>Trimble 4000SSI Receiver/ Trimble CR Antenna</i>
<i>DRYG</i>	<i>Dry Ghaut/ Landing Bay</i>	<i>62.1480°W, 16.6920°N</i>	<i>3 Dec 2009</i>	<i>Ashtech UZ-12 Receiver/ Leica AT504 CR Antenna</i>
<i>FERG</i>	<i>Fergus Ridge</i>	<i>62.1774°W, 16.6928°N</i>	<i>17 Feb 2010</i>	<i>Ashtech UZ-12 Receiver/ Leica AT504 CR Antenna</i>
FRGR	Fergus Ridge	62.1774°W, 16.6928°N	27 Jul 2011	Trimble NetRS Receiver/ Trimble Zephyr Geodetic 2 Antenna +D
GERD	Gerald's	62.1943°W, 16.7948°N	2003	Trimble NetRS Receiver/ Ashtech Dorne Margolin CR Antenna +D
HARR	Harris Lookout	62.1678°W, 16.7413°N	7 Oct 1995	Trimble 4000ST CR Antenna
			20 Nov 1996	Trimble CR Antenna
			11 Aug 1997	Leica AT302 Antenna
			17 Nov 2000	Trimble Dorne Margolin TurboRogue CR Antenna
			16 Jan 2003	Ashtech UZ-12 Receiver/ Leica AT504 CR Antenna +D
			5 Nov 2008	Trimble NetRS Receiver/ Leica AT504 CR Antenna +D
			7 Apr 2009	Trimble NetRS Receiver/ Trimble Zephyr Geodetic Antenna +D
✦ HERM	Hermitage Estate	62.1698°W, 16.7216°N	12 Jul 1996	Trimble 4000SSI Receiver/ Trimble CR Antenna
			18 Jan 1997	Trimble 4000SSI Receiver/ Leica AT302 Antenna
			19 Feb 1998	Trimble 4000SSI Receiver/ Trimble CR Antenna
			16 Jan 2003	Trimble 4000SSI Receiver/ Trimble 4000ST CR Antenna +D
			3 Oct 2008	Trimble NetRS Receiver/ Trimble Zephyr Geodetic Antenna +D
<i>(LEES)</i>	<i>Lee's Estate</i>	<i>62.191°W, 16.72°N*</i>	<i>1996</i>	<i>Trimble 4000SSI Receiver/ Trimble CR Antenna</i>
<i>LGFM</i>	<i>Long Ground Farm</i>	<i>62.1585°W, 16.7248°N</i>	<i>--</i>	<i>Leica SR9500 Receiver/ Leica AT302 Antenna</i>
			<i>9 Apr 2010</i>	<i>Ashtech UZ-12 Receiver/ Leica AT504 CR Antenna</i>
<i>LGRD</i>	<i>Long Ground (Clinic)</i>	<i>62.1615°W, 16.7244°N</i>	<i>19 Nov 2009</i>	<i>Ashtech UZ-12 Receiver/ Leica AT504 CR Antenna</i>
<i>(LKYN)</i>	<i>Lookout Yard</i>	<i>62.188°W, 16.79°N*</i>	<i>1996</i>	<i>Trimble 4000SSI Receiver/ Trimble CR Antenna</i>
✦ MVO1	MVO Mongo Hill	62.1929°W, 16.7767°N	18 Feb 1998	Trimble 4000SSI Receiver/ Trimble CR Antenna
			16 Jan 2003	Trimble 4000SSI Receiver/ Trimble 4000ST CR Antenna +D
			1 Oct 2008	Trimble NetRS Receiver/ Trimble CR Antenna +D
			16 Jul 2010	Trimble NetRS Receiver/ Trimble Zephyr Geodetic Antenna +D
<i>MVO2</i>	<i>MVO Flemmings</i>	<i>62.2126°W, 16.7486°N</i>	<i>26 Nov 2009</i>	<i>Ashtech UZ-12 Receiver/ Leica AT504 CR Antenna</i>

Details of GPS sites installed on Soufrière Hills Volcano since 1995, showing dates of installation and equipment changes. Not a complete listing, Stations which have been destroyed or otherwise decommissioned appear in parentheses (the end date, where available, is also in parentheses). Episodic GPS (eGPS/ campaign) sites appear in italics. Orange cross represent the two sites used in this study.

Chapter 2

Methods

2.1 Data Acquisition

All data for this analysis was gathered by or for Dr. Glen Mattioli as part of a study that was initially funded by a NASA grant and then was subsequently funded by several NSF awards. In the 1990's GPS became the primary tool for geodetic surveys. According to Blewitt (1993) the main reasoning behind this switch was: (1) easy access to economically affordable hardware and software; (2) ease of portability; (3) an international civilian tracking network that allowed easy collaboration; and (4) the development of millimeter precision for baselines in the 10's of kilometers and centimeter precision for baselines in the 100's of kilometers. By the late 1990's dense networks of GPS receivers had been deployed along seismogenic zones in populated regions to measure surface deformation, with data used to understand strain accumulation as well as aid in hazard assessments.

Before the 1995 eruption of SHV, the U.K. Department of Ordnance Survey (DOS) operated a triangulation network on Montserrat. Surface deformation measurements on SHV using GPS geodesy began in August 1995 at the onset of unrest (Mattioli et al., 1998). GPS data were initially collected in campaign mode from six sites distributed around the SHV. These six sites were chosen at azimuths and horizontal distance to SHV (0.8 to 3.6 km) to maximize scientific return, in relation to volcanic hazard zonation, access to power lines and availability of water during drilling operations (Mattioli et al., 2004). The original DOS monuments were comprised of a small cylindrical or rectangular concrete pedestal, with a central 25 cm diameter steel pipe driven to refusal, that was buried ~1-2 m below ground surface. A rigid plastic (PVC) insert, with a clearly defined central mark, was created to insure a tight fit with the steel pipe and then inserted to allow for easy antenna set up (Mattioli et al., 1998; Odbert et al., 2012).

According to Mattioli et al. (2010) and reiterated by Odbert et al. (2012) these early GPS observations at SHV can be divided into four distinct phases:

- 1) Network establishment with L1-carrier phase and C/A code observations during August 1995;
- 2) Daily L1/L2 phase and code observations between October 7, 1995 and December 29, 1995;
- 3) Network densification and expansion with nearly daily L1/L2-carrier phase and code observations between May 14, 1996 and August 8, 1996;
- 4) Installation of two continuous GPS sites in July 1996 and intermittent reoccupation of all network sites from September 1996 to June 1997.

The initial GPS observations were made in late August 1995 using two Trimble GeoExplorer, 6-channel, L1 carrier phase receivers with internal antennas. The study was conducted to determine if any measurable displacement or strain greater than position uncertainties of the original DOS survey had occurred on SHV between the time of last adjustment in 1974 and August 1995. Site coordinates, transformed to the WGS 84 reference surface, were provided by the DOS along with an estimated uncertainty of ± 9 cm for baselines of 3 to 8 km (Mattioli et al., 1998). GPS L1 baseline repeatability during the August 1995 survey was 3-5 cm for occupations lasting several hours at each site. Within these error limits, no statistically significant (1σ) deformation had occurred on SHV DOS baselines between 1974 and 1995 (Mattioli *et al.*, 1998). When surface deformation data were reexamined at a later date, looking at changes based only on GPS observations, deformation was clearly observed. In the summer of 1996, a continuously-operating GPS (cGPS) stations was installed at Hermitage Estate (HERM, ~1.6 km from SHV). It was destroyed by volcanic activity in 1996, and has been damaged and repaired several times and then worked nearly continuously since 1998. In early 1998, a new cGPS sites was installed at what was then the Montserrat Volcano Observatory (MVO1, ~7.6 km from SHV on Mongo Hill). The cGPS network at the end of 1999 consisted of 6 sites. In 2003, the CALIPSO project enhanced the cGPS infrastructure at SHV with the installation of four more sites (Mattioli et al., 2004). Since 2002, all of the CALIPSO cGPS sites have been equipped with choke-ring antennas and SCIGN hemispherical radomes.

Observations are routinely logged at 30-second intervals in 24-hour sessions. Between October 2008 and June 2009, the original six MVO-operated cGPS sites (HARR, HERM, MVO1, SOUF, SPRI, and WTYD) were upgraded with Trimble NetRS receivers and the network was upgraded with new FreeWave Ethernet radios (Table 1). The new configuration provided improved remote access to the receivers for configuration and data download. Trimble Zephyr Geodetic antennas have been phased-in to replace the choke ring antennas at the three original sites installed by Mattioli with NASA funding and the three sites installed by BGS, but monuments have remained largely unchanged (personal communication with G. Mattioli). Since mid-2010, receivers at all of the MVO-operated cGPS stations have been configured to record two parallel 24-hour sessions: one logging observations at 30-second intervals and the other at 1-second intervals. Earlier data archives contain only lower rate (30-second) observation files.

Various challenges make GPS monitoring at SHV difficult. The loosely-consolidated volcanoclastic deposits, which comprise the bulk of Montserrat's geology, are not ideally suited for the installation of high-precision survey stations (Odbert et al., 2012). Optimally a GPS antenna monument would be 'fused' to the bedrock via a drilled and braced frame for example similar to UNAVCO standards used for PBO or COCONet. A particular style of monument has been adopted on Montserrat to account for the absence of solid bedrock and the logistical and safety considerations that render deep drilling impractical on the volcano's flanks. These were built by manually digging a pit with a depth of up to about 2 m then constructing a reinforced foundation using blocks, cement and rebar, with maximum possible mechanical coupling to the surrounding ground. Vertical rebar rods connect the foundation to a concrete pillar extending about 1-1.5 m above ground level and about 30 x 30 cm in cross section. A threaded, metal antenna mount rod is built in to the pillar, extending vertically such that the antenna is installed about 10-30 cm above the top of the pillar (Mattioli et al., 2010; Odbert et al., 2012).

At Mongo Hill (MVO1), a similar concrete pillar was built on the corner of the roof of a small building in the garden of the old observatory building. According to Odbert et al. (2012) there is an enhanced susceptibility at this site to multipath effects due to the surrounding buildings since the layout and extent of the surrounding construction have changed since installation however an in-depth

evaluation of the M1/M2 signals for this site in comparison to others was not done for this study. The potential for multipath – whereby satellite signals reach the antenna via multiple direct and reflected paths, thus introducing path length ambiguity – and this should be a concern for installation and subsequent use of any future GPS site. Despite this potential problem, this site has yielded excellent data and has the longest un-interrupted time series of any GPS site on SHV.

GPS data were originally processed using NASA's GPS Inferred Positioning System-Orbit Analysis and Simulation Software (Lichten and Border, 1987), (GIPSY-OASIS II or GOA-II) version 4 using a non-fiducial, absolute point positioning strategy. All raw GPS observations were processed with final, precise satellite orbits, clocks, earth orientation parameters, and X-files from the Jet Propulsion Lab (JPL) to estimate the 3D position for each cGPS site per 24 hr UTC day in ITRF05 (Mattioli et al., 1998; Mattioli et al., 2010 SOI).

2.2 Data Processing and Analysis

GPS data were reprocessed with GOA-II version 6.1.2, which is a collection of UNIX based software programs developed at the Jet Propulsion Laboratory (JPL) that uses precise clock and orbit parameters also provided by JPL. The initial calculated positions are non-fiducial, and in the free frame or satellite reference frame. These positions are then translated, rotated, and scaled into the International GNSS Service 2008 (IGS08), the realization of the International Terrestrial Reference Frame (Altamimi et al., 2011), using x-files from JPL (Zumberge et al., 1997), and then into a more useable, plate-based reference frame with the Demets et al. (2000; 2007) version of the GPS-derived Caribbean plate to examine site velocities relative to the fixed Caribbean plate.

GOA-II was developed at JPL to solve for precise positions from GPS data collected in the field. It consists of numerous individual programs and modules and can be tailored to suit the needs of any user. For GOA-II to be used, the raw data, or GPS observables, must be converted from the receiver specific formatting to the Receiver Independent Exchange Format (RINEX) (Estey and Meertens, 1999), and named according to GIPSY format, which then allows the data to be processed in an automated manner

using a UNIX script that was initially authored by Charles DeMets and then later significantly modified by Glen S. Mattioli. Turner (2003) presents a detailed description of the steps involved in the processing of GPS data using GOA-II software to calculate precise point positions. The discussion below is taken from Turner (2003) and reproduced here with minor modifications.

1. The program *Ninja* translates the rinex files into a FORTRAN binary file, removes outliers, and detects cycle slips. The data are decimated into 300 second intervals and data for each satellite are merged into a *qm* file.
2. Individual *qm* files are merged into a single file, the *QMfile*, by the program *merge_qm*. A namelist is created from the *QMfile* called *qregress.nml*.
3. The *qregress.nml* namelist is used to derive *qregress*, which does the physical modeling of the receiver measurements. In our analysis scheme, *qregress* uses final precise satellite orbits, clocks, and earth orientation parameters provided by JPL. *Qregress* applies the physical models (receiver location time dependence, tidal effects, polar motion and earth rotation, nutation, procession, perturbation, rotation, geocenter offset, and coordinate scaling) to the orbits and observations and outputs a regress file, *rgfile*, which contains the parameter partials and nominal values.
4. The *rgfile* is used by the program *wash_nml* to create a *wash.nml* file. The *rgfile* and the *wash.nml* files are the input for the preprefilter, prefilter, and filter modules. The filter module runs the Square Root Information Filter, which processes small batches of data sequentially and produces the *accume.nio*, *smooth.nio*, and *uinv.nio* files.
5. *Smapper* follows the filtering process and smoothes and maps the covariance, sensitivity, and solution of the parameter estimation.
6. *Postfit* computes the post-fit data residuals.
7. *Postbreak* searches for cycle slips missed by *Ninja* and modifies the *QMfile* if cycle slips are detected and reruns GIPSY.
8. *Edtpnt2* adds or deletes data points to or from the filtered solution to remove outliers. After *Edtpnt2* is run, *smapper* and *postfit* are rerun.
9. The *stacov* module produces the final solution files in text format.

2.2.1 GD2P.PL Perl Script

Information below is from a training class given by the JPL in December 2008 and is presented with little modification.

According to JPL, gd2p Perl script (gd2p.pl - GPS data 2 Position) is a high level GIPSY interface for processing data from a single GPS/GLONASS receiver. GOA-II version 6.1.2 uses gd2p.pl. as it is a

more modern code, written in modern programming language known as perl, and is the preferred processing code for single receiver data due to the ease it allows in making changes to an existing run, (e.g. run_again), as well as offering better error detection. Gd2p can be used for Static Point Positioning, Kinematic Point Positioning, and Precision Orbit Determination (POD), clock estimation, and troposphere estimation. For POD gd2p is able translate data from Dual Frequency, Single Frequency, Single Antenna, and Multiple Antennas.

2.2.2 GIPSY-OASIS Processing Version 6.1.2

This latest version of GOA-II at the time this study was used to reprocess the raw GPS data for the HERM, MVO1, and BGGY sites. Listed below are the changes made to the program in comparison to Version 4, as outlined from the GIPSY 6.1.2 Release Notes of January 18, 2012, (Jet Propulsion Laboratory, California Institute of Technology) and reproduced here with little modification.

New or Updated Models

IAU80. The IAU80 model can be applied by setting PreNut = 'IAU80' in either the \$earth_orientation namelist group or in the Info line of a GIPSY Earth Orientation Parameter (GEOP) file.

IERS2010 tidal displacement models added or verified identical to IERS2003. IERS2010 is the default displacement model. The most significant effect for a receiver on the surface of the Earth is the effect of the IERS 2010 model for the mean pole location on the pole tide. The change to the mean pole location model results with differences (w.r.t. the previous model) of < 0.1 arcseconds from 1990-2015, which then causes change of < 3 mm in vertical and < 1 mm in transverse positions from the pole tide. This difference will manifest as a cubic function before 2010 and as a linear function after 2010 and thus changed the pole tide Love number from 0.6027 to IERS2010 value of 0.6207.

Replaced previous subroutine for ocean load tides (hardisp.f) with new version (hardispjg.f). The new subroutine is a modification of the program hardisp.f that is provided with the IERS2010 standards, with the following modifications:

IERS2010 program hardisp.f made a subroutine named hardispjg.f,

All real numbers changed to double precision.

MDAY subroutine removed and replaced with GIPSY's DOYOYR subroutine.

TOYMD, JULDAY, LEAP, and ETUTC subroutines removed and replaced with GIPSY subroutines for computing IERS2010 models of fundamental tidal arguments and

frequencies, and for converting UTC time to ephemeris time. As such, modifications are not needed for future leap seconds.

IERS2010 tidal potential models added were verified as identical to IERS2003. IERS2010 is the default model. Also includes adopting the IERS2010 model for the mean pole location, which affects the solid Earth and ocean pole tide models.

All products are provided in formats native to GIPSY.

Products include information to enable single receiver ambiguity resolution with the GIPSY-OASIS software. The table above indicates the current availability of the product file (wlpb) that is required to enable single receiver ambiguity resolution. However, a reanalysis of historical GPS data is underway to generate wlpb files (see section 6.2).

Daily Rapid and Final products span a 30-hour window centered at noon of each day.

All orbit estimates are provided with respect to the Earth's instantaneous center of mass. When applying ocean load tide corrections, users are advised to use a model that is defined with respect to the instantaneous center of mass. The option "- add_ocnld" in gd2p.pl allows the user to specify a specific coefficient file with ocean loading coefficients.

Ultra-Rapid, Rapid, and Final clock products all include 5-minute clock solutions. Final products also include high-rate (hr) 30-second clock estimates. Reprocessed Final products released in 2011 will include high-rate clock estimates for the entire product set. Rapid products also include high-rate (hr) 30-second clock estimates starting in July 2011. The high-rate clock estimates are available about two hours after delivery of the standard Rapid products.

All three products may be automatically fetched with gd2p.pl using the `-orb_clk` flag.

Orbit/clock products for the GLONASS constellation are expected to be available in 2012. GIPSY 6.1.x should be capable of performing precise positioning with those GLONASS products.

Chapter 3

Previous Deformation Models

3.1 Voight et al. (1999) Model

A model by Voight et al. (1999) proposes that a stick-slip situation occurring in the upper conduit of the SHV, could cause surface deformation of the edifice, as well as lead to aborted eruption events. This model finds its basis in cycles that lasted from hours to days, which were proposed to have been initiated when degassed stiff magma retarded flow in the upper conduit. It is thought that this stick-slip situation is controlled by two processes: 1) degassing and crystallization create a viscoplastic magma plug that inhibits conduit flow; and 2) pressurization occurring under the plug of the gasses and magma, which eventually exceeds the tensile strength of the plug resulting in extrusion and explosive activity. The Voight et al. (1999) model is based on the idea that the rheology of the magma changes over time, due to degassing and expansion of the magma, leading to the cyclic pressure changes in the upper conduit, and thus edifice deformation recorded on the tilt stations. It was estimated that the undegassed magma had a viscosity of about 10^6 Pa s, and the completely degassed dome lava had a viscosity of about 10^{14} Pa s with the material behaving as a non-Newtonian fluid and with yield strength. Using evidence that there have been stable lava spines of (~100m) or greater on SHV, the assumption was made that the shear strength of the extruded lava dome was ≥ 1 MPa. Gas exsolution from the ascending magma and microlite crystallization caused an increase in magma viscosity thus forming the rheologically stiffened plug that restricted conduit and caused edifice deformation to occur (Voight et al., 1999). The idea that the plug was being formed from heat loss due to conductive cooling was ruled out due to the short time span of the process so while latent heat was being liberated during the degassing-promoted crystallization, temperatures taken from pyroclastic flow show dome lavas still exceeding temps of $>700^\circ\text{C}$.

Because of the magma plug, the pressure buildup in the upper conduit caused edifice inflation, which was then used as a pressure gage. Using tiltmeters stationed at 630 and 770m from the dome, and using the ratio of the tilt inflations from both (avg 1.28), a model of the depth to pressurization was

created. It is typically assumed that for a strain source embedded in a homogeneous elastic half-space you would expect a depth of pressurization of 770m with a spherical shape. However since this is almost certainly not the case at Montserrat, it was determined that a better model would be one of a finite line source in an elastic half-space, such as a pressurized vertical conduit. Using this idea it was proposed that the minimum depth to the top of the pressurizing part of the conduit, or the base of the plug, is around 400 m from the top of the dome, and it was noted that little changed with shifts of <200 m from the assumed vent location.

Using this information, compression tests were performed on altered Soufriere Hill's tuff and thus it was concluded that the pressure change in the conduit during inflation has an upper bound of 60 MPa, which is greater by a factor of ~2 from the upper bounds derived from ballistic launch velocities testing previously done (Voight et al., 1999) These data imply that the hybrid earthquakes that begin during inflations start when a pressurization threshold is exceeded and stop when the pressure is released and drops below this threshold. Calculations suggest a seismic threshold overpressure of ~ 3 to 8 MPa, which are very similar to the tensile strength seen in intact andesite on the volcano, thus it is hypothesized that hydrofracturing and the release of pressurized gas from the upper conduit are the cause for the earthquake swarms (Voight et al., 1999). Eventually the overpressure increased enough to remove the plug, usually explosively, from the conduit and thus the cycle begins all over.

The conduit pressure gradient is constrained by the dimensions of the conduit, extrusion and intrusion flux rate, and magma viscosity. It has been determined that all play a significant role in the eruption, and that a larger conduit alone does not lead to larger eruptions, but that viscosity plays an important role in the amount of magma and type of eruption that occurs. The model concluded that a minimum conduit outlet pressure of Soufriere Hills (at the time the model was created) is constrained by the pressure exerted by the 250 m thick dome, and is around 5 MPa, and with a magma chamber depth of ~ 5km, the magma chamber over pressure is approximately 11 to 25 MPa. These results suggest that shallow conduit overpressures may be equal to or may even exceed magma chamber over pressures, and thus the pressure gradient in the conduit of andesitic volcanoes is highly nonlinear.

Correlations made between accelerated ascent rate and the cyclic behavior seen at Montserrat is consistent with a reduced rate of degassing during ascent, with rates >1 km/day. Thus highly volatile rich magmas have reached the surface in less than 5 days, where steady flow became unstable due to pressure decreasing as the velocity increased, and slip occurs, as does deflation, providing a first order stick-slip description of the cyclic behavior noted at Montserrat.

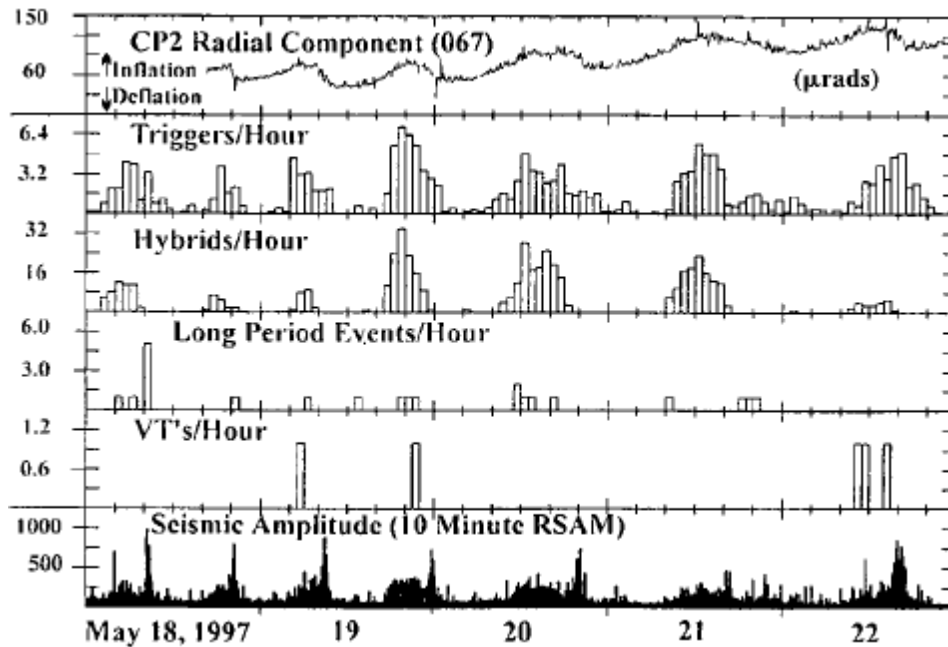


Figure 6 Cyclic CP2 tilt time series.

Correlation of cyclic CP2 tilt time series (radial component, 067 azimuth) with triggered earthquakes, hybrid earthquakes, LP earthquakes, VT earthquakes, and seismic amplitude RSAM for 18 to 22 May 1997. RSAM provides a simple real time quantitative measure of seismicity but does not discriminate between event types; large spikes reflect pyroclastic flows. Triggered earthquakes are the numbers recorded at a given station during 10-min periods with data presented as triggers per hour; they are a measure in real-time of hybrid earthquake swarms (Voight et al., 1999).

Figure 7 shows a proposed configuring of the magmatic system beneath Soufriere Hills Volcano, as proposed Mattioli et al. (1998) and modified by Hautmann et al. (2010). If this geometry is taken as the most likely for the magmatic system situated under the volcano, the stick situation described by Voight et

al. (1999) would occur in the upper portion of the conduit. The green line in the image represents the magmatic plug in the upper conduit, which would cause inflation and deflation of the edifice as pressures built and dropped beneath it. Figure 8 is a simplified diagram of the proposed model using the magmatic configuration of Figure 7.

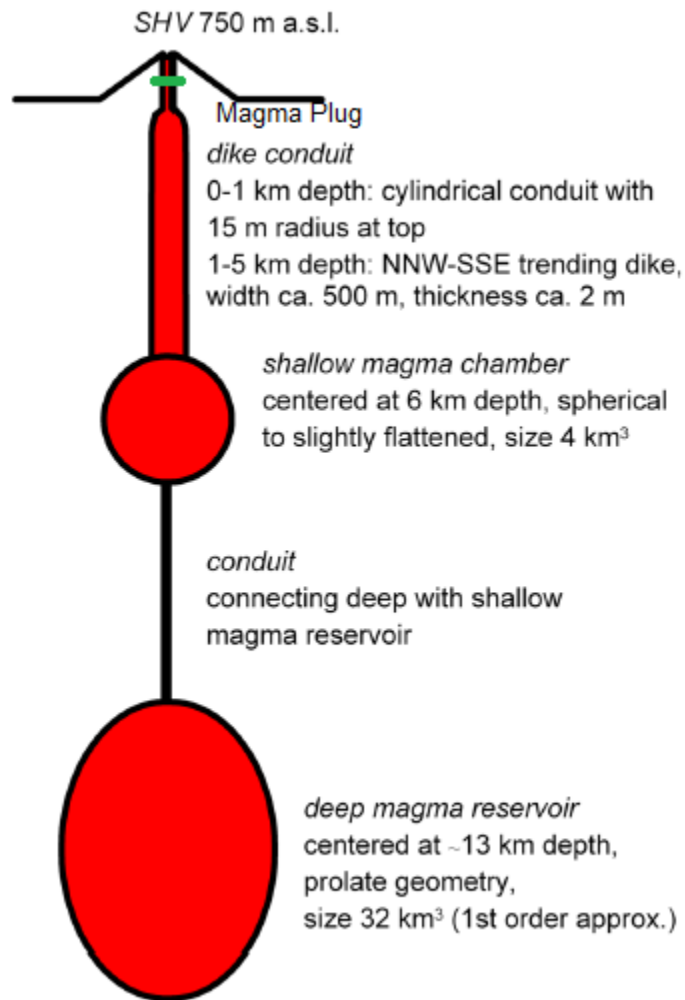


Figure 7 Proposed chamber geometry of SHV

Geometry of SHV magma chamber as proposed by Mattioli et al., (1998) and modified by Elsworth et al., (2008). Figure is from Hautmann et al., (2010) Small green line is proposed stiffened magmatic plug in upper conduit.

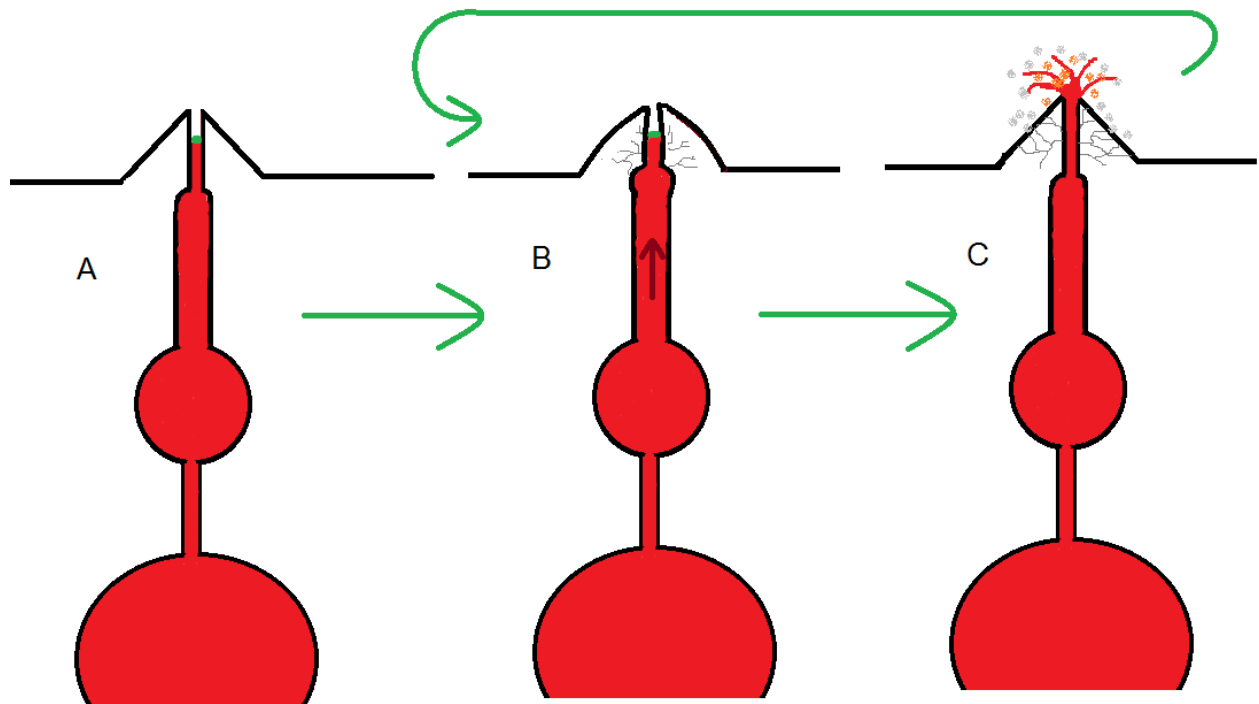


Figure 8 Simplified view of Voight et al. (1999) model.

A. Volcano as plug is initially formed, little to no pressure build up behind plug. **B.** shows the edifice beginning to inflate and crack as the pressure builds behind the plug. Degassing and crystallization begins. **C.** Pressure exceeds the tensile strength of the plug, magma and gasses are extruded as slip occurs in the conduit. This continues until magma degasses and crystallizes until the viscosity increases to the point that a new plug is formed and the cycle begins all over again.

3.2 Denlinger and Hoblitt (1999) Model

Denlinger and Hoblitt (1999) also developed a model to explain observed deformation cycles that were hours to days long. Their model is based on experiments on extrusion of industrial polymer melts, which are known to show periodic oscillations when extruded at high pressures through a small conduit. The foundation for this model was developed after eruptions at SHV and Mount Pinatubo, where it was seen that the two volcanic edifices inflated and deflated during short term eruption cycles. Based on polymer melt experiments, Denlinger and Hoblitt (1999) made the assumption that silicic magmas behave according to a Newtonian rheology, and thus the rheology stays constant, which is also supported by experimental data showing that silicic magma is Newtonian at eruption temperatures (Hess and Dingwell, 1996). This difference in rheological behavior of the magma in the upper conduit is a major distinction between this model and the Voight et al. (1999) model.

Denlinger and Hoblitt (1999) infer that as magma rises, shear stress exerted against the conduit wall reaches a threshold or detachment point, where the wall-strength is overcome and magma slip occurs. The onset of slip only slightly affects the magnitude of the shear stress along the wall, but it greatly increases the shear rate. Because the magma behaves as a Newtonian fluid, when the wall slip event occurs, the fluid has an abnormally high flow rate for the same pressure drop in the conduit. If flow rate through the conduit exceeds magma supply, then the pressure in the conduit, or flow resistance abruptly drops, thus the flow rate jumps even higher and the compressed magma expands. Thus the output flux decreases until slip ceases when magma reattaches to the conduit wall and the cycle begins all over again (see figure 9).

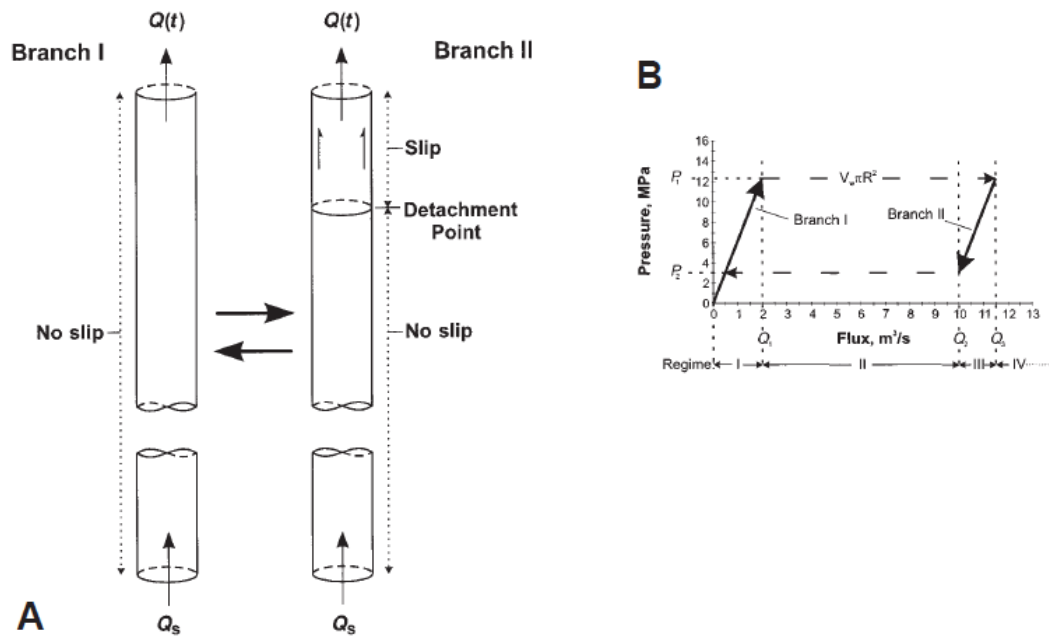


Figure 9 Conduit Model

A: Conduit model. Along branch I in B, melt adheres to conduit wall. Along branch II in B, melt slips along near-surface portion of conduit (hundreds of meters) while adhering to remainder of conduit. B: Hysteresis in flow resistance that drives oscillatory flow. Nonoscillatory flow occurs for supply rates $Q_s < Q_1$ (2 m³/s) or greater than Q_2 (10 m³/s). For supply rates between Q_1 and Q_2 , oscillatory flow occurs as pressure (P) and flow rate follow path shown by arrows. Pressure increases along branch I with melt adhering to wall everywhere. At Q_1 , P_1 melt slips along conduit wall above detachment point and flux jumps from branch I to branch II as wall slip enhances flow rate. Along branch II, melt production exceeds supply and pressure decreases. Eventually melt readheres to conduit wall at Q_2 and P_2 , flux switches to branch I, and cycle begins again. Such behavior is observed in high-pressure extrusion of polymer melts Denlinger and Hoblitt (1999).

Denlinger and Hoblitt (1999) applied the polymer model, and concluded that a change in flux through the conduit changed the shape and period of the waveform of the efflux and pressure oscillations; rapid flux ($10.5 \text{ m}^3/\text{s}$) resulted in a sharp peak with a long release time, while slow flux ($2.5 \text{ m}^3/\text{s}$) resulted in a low sloping rise and quick drop. Thus it was noted that the key elements for the oscillations to occur are: 1) that the magma is fed into the conduit at a constant rate and that the magma is compressible, and 2) that the magma is Newtonian and will slip on the conduit wall when supply rate exceeds the threshold shear stress (Figure 9). Because the magma is a Newtonian fluid, compressibility is required for the oscillations to occur, as energy can be stored and released as the magma alternately sticks and slips along the conduit wall (Denlinger and Hoblitt, 1999). Figure 10 shows the waveforms created by an increase in flux rate from low flux rate to high flux rates.

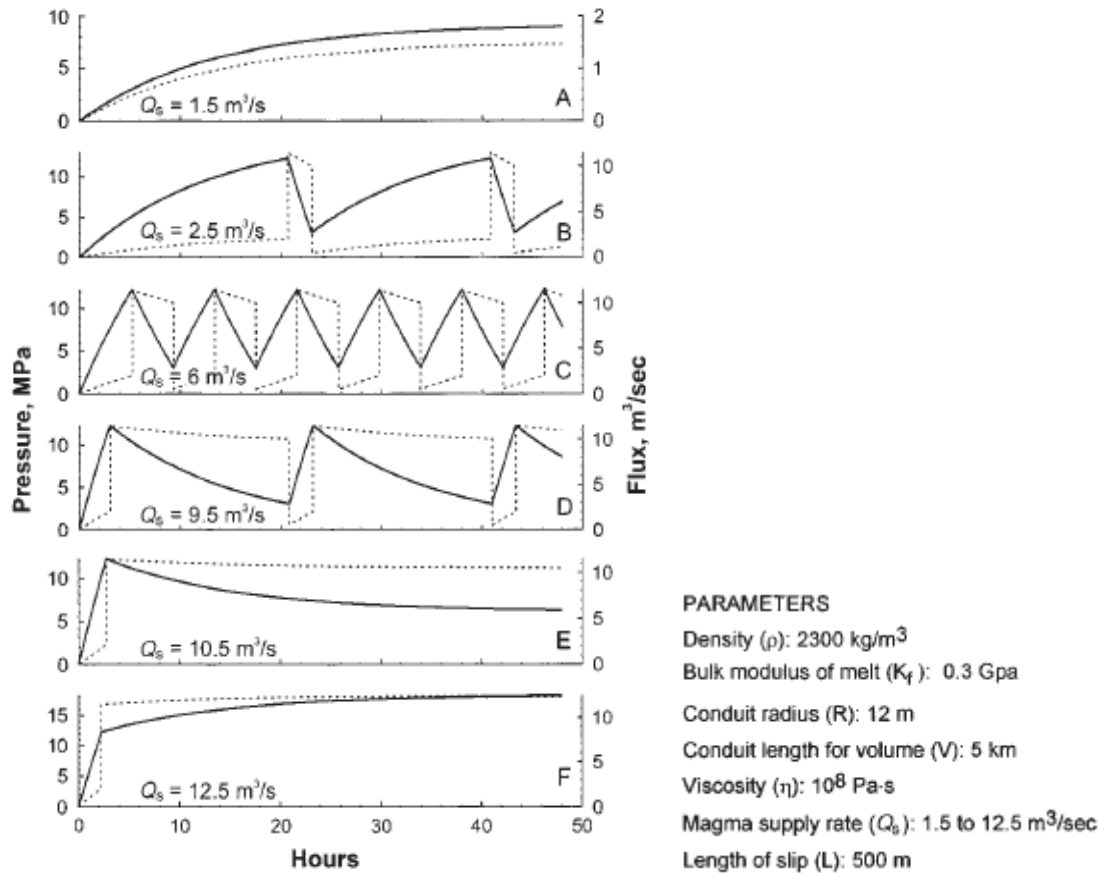


Figure 10 Flux Rates and resulting cycle shapes.

Modified from (Denlinger and Hoblitt, (1999). Changes in pressure cycle shape that result from varying supply rate for hysteresis loop. Supply rates ($< 2 \text{ m}^3/\text{s}$) and ($> 10 \text{ m}^3/\text{s}$) do not produce oscillations. Solid waveform line represents the surface deformation and is produced by the changes in pressure that occur in the upper conduit during the stick-slip cycle. Waveform asymmetry results from supply rate closer to one end of hysteresis loop than the other. This provides paradigm to interpret oscillatory behavior of erupting volcanoes. Dashed lines show change in flux rate that occurs during the inflations and deflations caused by the stick-slip in the conduit.

3.3 Mattioli et al. (1998) Dike Emplacement Model

An alternative model that could explain the short term deformation seen SHV could be due to the opening of a dike below the conduit of SHV. Feeder dikes bring magma to the surface, while non-feeder dikes become arrested and never reach the surface (Geshi et al., 2010). The presence of a shallow dike beneath SHV was first proposed by Mattioli et al. (1998), to explain non-axially symmetric, horizontal displacements and decreasing subsidence observed at SHV from October 1995 to July of 1996. It was proposed that a shallow vertical dike (<3 km), which expanded >1 meter, was coupled with a deflating Mogi source located at about 6 km depth to best explain the observed GPS derived velocities. This model is based on GPS data from 1995 to 1997.

This model was derived from the inversion of recorded ground deformation data and resulted in a proposed dike –conduit system that is trending NW-SE to NNW- SSE (Mattioli et al. 1998). This geometry was supported by later studies including Hautmann et al. (2010) and Linde et al. (2010). As there was no effusive activity seen before November 1995, this dike would be considered to be a non-feeder dike initially that transitioned to a feeder dike. It has been noted that during periods of volcanic unrest, when a dike may have been injected into the upper edifice from a magma chamber, an eruption does not always occur (Geshi et al., 2010). I propose that a dike emplacement model could explain the short term deformations recorded at HERM and show that as this volcano was becoming active, a non-feeder dike opening in the region below the vent could be an alternative and more likely scenario for the surface deformation events recorded at HERM. The HERM GPS site sits nearest to the vent of SHV, and as such, this site does not conform to the cyclic deformation recorded at sites further from the vent, thus it has always been excluded from other models.

Chapter 4

Results

Deformation recorded in the continuous sites HERM and MVO1 are shown in the time series in Appendix A for the GOA-II (ver. 6.1.2) reprocessing. Each time series has three panels, showing the latitudinal, longitudinal, and vertical components of 3-D positions and least squares linear best fits to velocities relative to the fixed or stable Caribbean plate. To derive the site rate with respect to the Caribbean plate, the observed best site rate in IGS08 is subtracted from the site rate predicted by the Caribbean plate model in IGS08. These time series represents GPS data collected over the period [1995-2010] at Soufrière Hills Volcano (SHV), Montserrat, West Indies, arguably the most extensive surface deformation dataset from any actively erupting, andesitic, composite stratovolcano (Mattioli et al., 2010). For comparison, time series data from the BGGY site from Antigua are included and these show little, if any, surface deformation relative to a fixed Caribbean. The improved time series can be seen clearly in the BGGY time series, after a new antenna was installed in 2008. Overall the GOA-II (ver. 4.0) time series (Figure 11), the data shows less variance in the plot when compared to when the data was rerun in GIPSY ver. 6.1.2 (Figure 12). This is caused by the fact that the linear model used is no longer adequate to model these sites. Due to the amount of surface deformation recorded at these sites, using the linear model will cause higher noise errors, however the reprocessing does show the “structure” of the surface deformation much clearer with GOA-II (ver. 6.1.2). The higher precision of the daily position estimates are due to better processing procedures, improved corrections for ocean loading, antenna models, and recomputed orbit. This has in part led to a higher "apparent" variance relative to a simple linear velocity model, (per G.S. Mattioli).

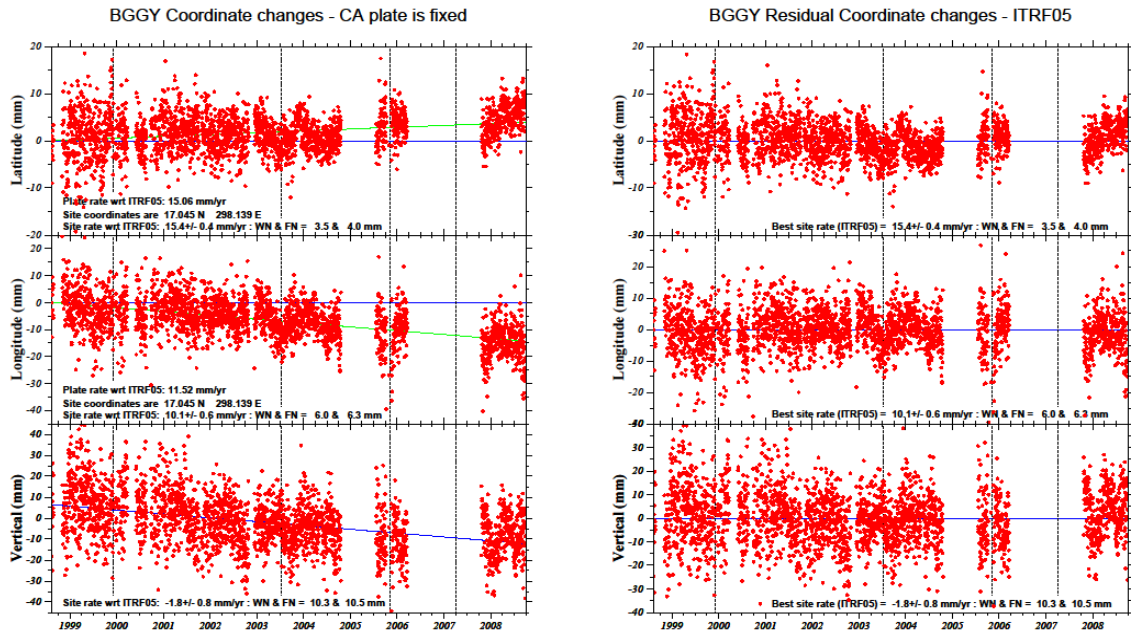


Figure 11 Time series for continuous site BGGY site processed using GIPSY (ver. 4.0). Red dots are UTC daily position solutions. The blue lines are the predicted Caribbean plate rates in ITRF05 held fixed (horizontal). The green lines are the least squares best fit site rates in IGS08. WN = white noise, FN = flicker noise.

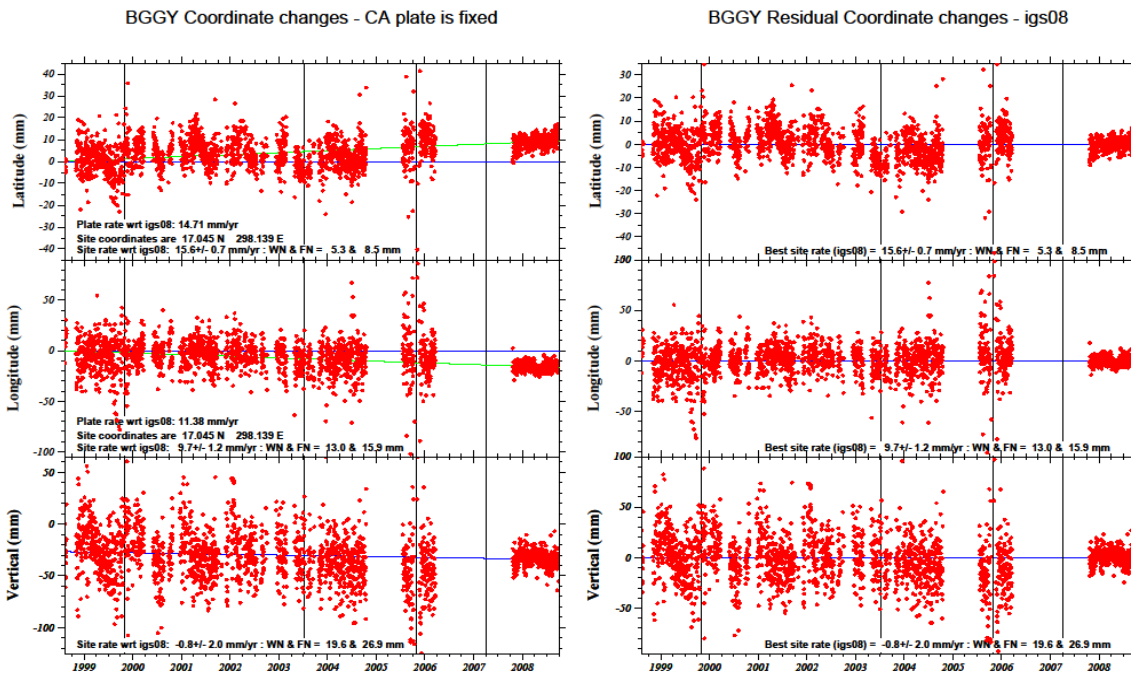


Figure 12 Time series for continuous site BGGY site reprocessed using GIPSY (v. 6.1.2). Red dots are UTC daily position solutions. The blue lines are the predicted Caribbean plate rates in IGS08 held fixed (horizontal). The green lines are the least squares best fit site rates in IGS08. WN = white noise, FN = flicker noise.

4.1 A Damping Effect

After reprocessing the data, along with adding the additional years of data to the time series, it was noted that SHV appears to be undergoing a cyclic damping effect. The duration of the volcanic period, or length of time the edifice is undergoing inflation and deflation, is decreasing with each successive cycle. By projecting the data back in time (Figure 13) to the period before the GPS site at MVO1 was installed, it can be seen that the length of time for inflation and deflation has decreased over the last two cycles. This projection of the data recorded at MVO1 goes back to the beginning of activity recorded at SHV, late 1995. Figure 13 shows that initially $V_{North}^{inflate} = V_{North}^{deflate}$, with V being the rate or length of time the SHV is undergoing inflation and/or deflation of the edifice, but with time the deflation rate is seen to dramatically decrease and becomes much shorter in duration than the inflation rate for the respective cycle. Volcanic eruptions are episodic despite being supplied by melt at a nearly constant rate and for three cycles of effusion followed by discrete pauses, supply of the [SHV] system from the deep crust and mantle was continuous (Elsworth et al. 2008). The long term deformation seen at SVH can be related back to the Denlinger and Hoblitt (1999) model that shows flux rate of magma in a system could lead to cyclic oscillations. While the Denlinger and Hoblitt (1999) model is used to describe short term oscillations ranging from hours to days in length, taking the model and applying to long term deformations that appear to follow the same cyclic oscillations is not such a long stretch, with the idea that the magmatic system is maintaining an average flux rate that falls into the parameters of the short term cycle model.

MVO1 Residual Coordinate changes - igs08

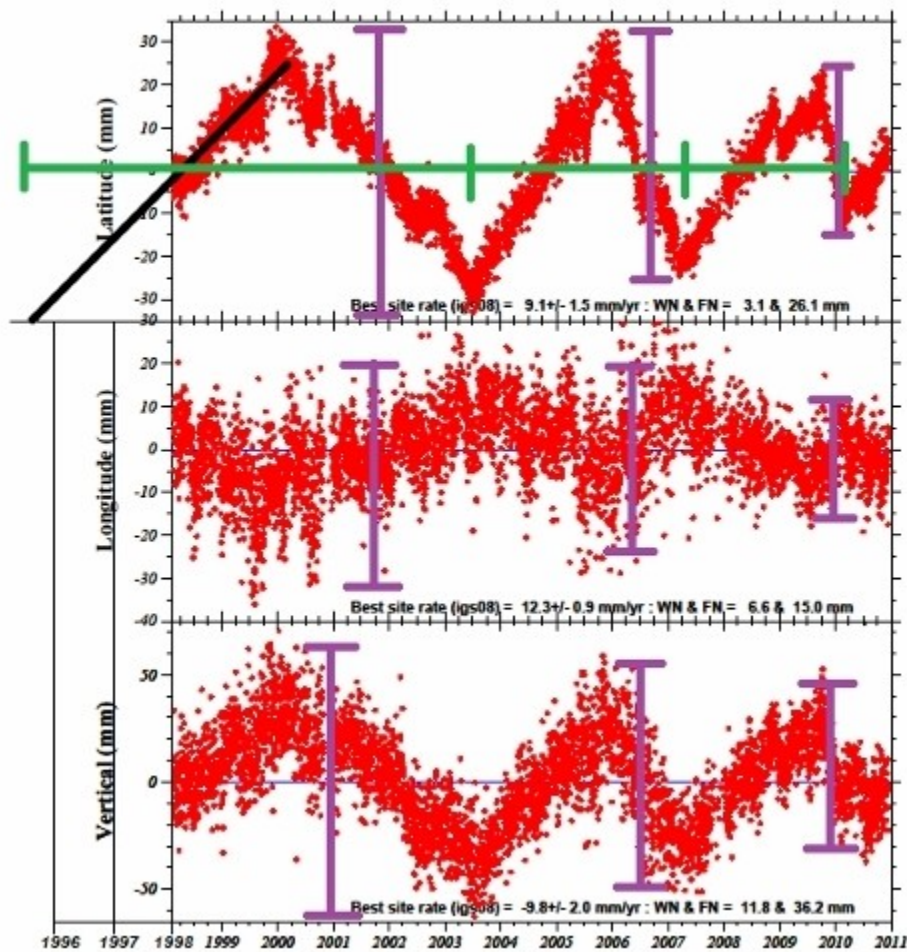


Figure 13 MVO1 period and amplitude of long term deformation.

The black line is the projected inflation for the first period, projected out prior to MVO1 placement. Green in the latitude graph shows the period from beginning of inflation to end of deflation. The purple bars are the amplitudes of each period.

In Figure 13, it is noted that in the first long term deformation cycle the inflations period and deflation period are roughly symmetric, as the data shows that it took SHV roughly the same time to inflate as it did to deflate. This observation is of course only an approximation as the data had to be projected back in time to before the monitoring began. In the Denlinger and Hoblitt (1999) model symmetric oscillations could be observed when the flux rate is at an intermediate input of approximately 6

m^3/s . If the flux rate of the magma from the mantle into the lower magma chamber and then into and through the second smaller chamber and onto the surface had an average flux rate of $\sim 6 \text{ m}^3/\text{s}$, it is highly plausible that the resulting data recording nearly symmetric deformation over the course of ~ 7.5 years, could in fact be due to the system maintain a steady flux rate. The second cycle of data recorded at SHV shows a change in the oscillation, with the deflation period occurring at a faster rate than the inflation. In this cycle, when compared to the Denlinger and Hoblitt (1999) model (figure 10) this cycle would fall in between the slow and intermediate flux, as the oscillation recorded does not look like either the $6 \text{ m}^3/\text{s}$ or the $2.5 \text{ m}^3/\text{s}$ cycle shapes, so perhaps it could be for a flux rate of around $4 \text{ m}^3/\text{s}$, though this of course is only speculation. The third data cycle at SVH resembles the cycle shape of the Denlinger and Hoblitt (1999) model for a flux rate of ($2.5 \text{ m}^3/\text{s}$), as in this cycle the deflation period was much more rapid than that of the inflation. The implications of this relate back to the Denlinger and Hoblitt (1999) experiment, and show that the flux rate of magma into the chamber is decreasing from a rate of approximately $6 \text{ m}^3/\text{s}$ in the first inflation-deflation cycle to around $2.5 \text{ m}^3/\text{s}$ in the third cycle (Figure 14). This slowing of flux rate is consistent with a volcano that is undergoing a damping cycle.

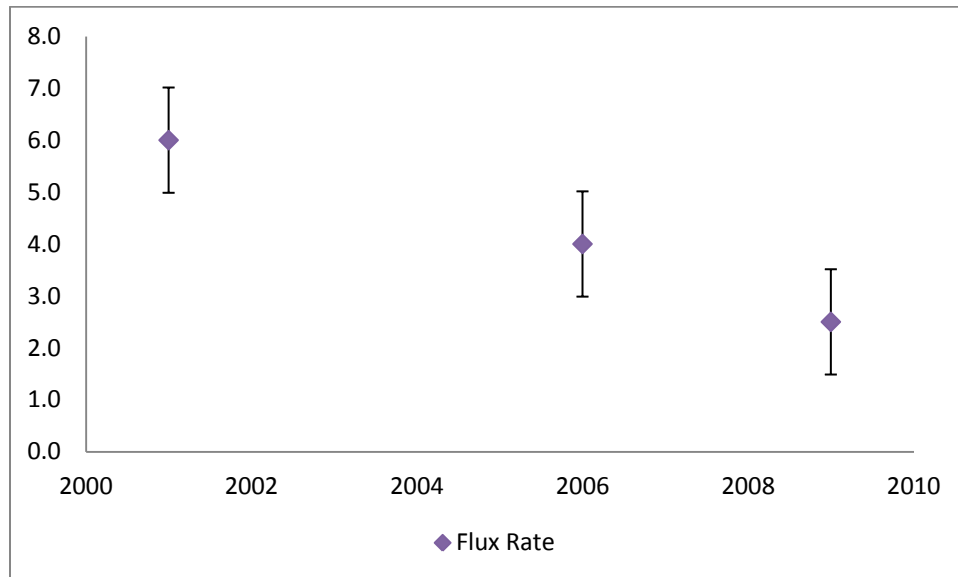


Figure 14 Apparent Flux Rate vs. Time

Apparent flux rate change over time from beginning of first deflation period in the first cycle in 2001 to the start of the deflation period in the third cycle in 2009.

When comparing the conclusions of this study based off of the Denlinger and Hoblitt (1999)

model for flux rate to the Elsworth et al. (2008) model, they are similar in the fact that both seem to agree that the flux rate during the deflation or repose periods is slower during the second eruption cycle than during the first cycle. However, in the Elsworth et al. (2008) model, the flux rate jumps to an even higher rate during the third cycle than that of the rate for the first cycle which does not agree with the Denlinger and Hoblitt (1999) model. The Elsworth et al. (2008) model has the first efflux cycle having an average rate of $4 \text{ m}^3/\text{s}$ and the second cycle having an average rate of $2.5 \text{ m}^3/\text{s}$. The third cycle however, is shown to have an average rate of $6 \text{ m}^3/\text{s}$ (Figure 15). This jump in rate does not agree with Denlinger and Hoblitt (1999) due to the fact that the long term surface deformation during the third cycle shows a much faster deflation period in respect to the inflation period, where as the if the rate were $6 \text{ m}^3/\text{s}$ then it should show more symmetric deformation. There could be another factor such as stiffening of the upper chamber that caused the non-symmetric deformation, but further study would need to be done to confirm or deny this idea.

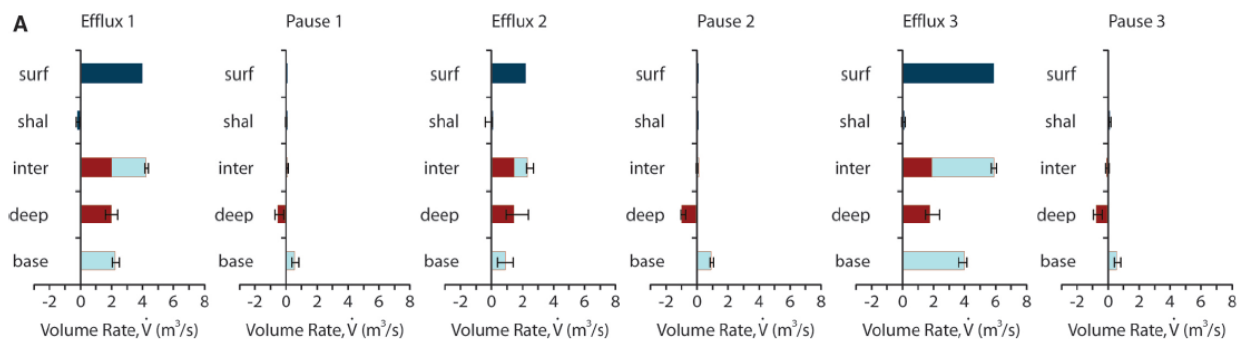


Figure 15 Elsworth et al. (2008) flux rates

Average interchamber, basement supply, and chamber inflation rates recovered from co-inversion of surface efflux and geodetic data for dual-chamber geometry. Flux rates are in cubic meters per second of dense rock equivalent (DRE), with surface efflux measured and all others calculated. Error bars denote the spread obtained from using data from the longest-aperture station (MVO1) together with data from stations SOUF, HARR, and WYTD. Chamber volume change rates (red, lower chamber; dark blue, upper chamber) are positive for deflation. Surface (surf, dark blue), interchamber (inter, red/blue), and basement (base, light blue) fluxes are each positive for upward flow. Shal is shallow. Interchamber flux is equivalent

to the sum of lower chamber deflation and basement supply (which passes through the lower chamber). Surface efflux is the sum of upper chamber deflation and interchamber transfer (pass-through).

What could be causing the flux rate to drop? Is the mantle melt in this region being depleted, or could the volcano be stiffening as the magma in the chambers cool, and thus the flux rate cannot be maintained as the chambers no longer have the same capacity? More modeling would and should be done to try and determine the likely cause for the dampening occurring at SHV.

Table 2 shows the total period length, amplitudes, and individual inflation and deflation lengths for the MVO1 sight for each long term period of deformation recorded in north, east, and the vertical. The first cycle recorded has a total period length of ~7.50 years, including the time span of the projected period, with a deflation period of ~3.48 years, or ~ 46.4% which is close to half the cycle time, thus this period is nearly symmetric (Figure 13). The second cycle has a total period of ~3.72 years, with the deflation period lasting ~ 1.42 years, which is a little more than ~ 38% of the time length of the cycle. The total period length for the third cycle is ~ 2.84 years, with the deflation period lasting only ~.32 year, or ~11.27% of the time length of the cycle. The data also show that not only is the volcano deflating at a much faster rate with each cycle, and that it is also failing to deflate to the same position it obtained in the previous deflations. The amplitude of each cycle is also damping. The volcano is inflating nearly the same amount with each cycle, with the loss in inflation significantly less dramatic than that of the deflation. SHV shows a loss in amplitude between the first cycle deflation to the third cycle deflation that is close to half in the north, east and vertical directions (Figure 13). This again causes us to ask the question of why? Is this related to a decrease in flux rate? Is there less magma being injected in to the system due the magmatic system cooling? Has the magma in the crustal storage zones cooled to the point that more solid rock is now under the volcano and thus the entire system is stiffening so that the edifice can no longer respond elastically and return to its former position? More study of this system is definitely called for to fully answer these questions.

Table 2 Period and amplitudes for the three cycles.

Long Term deformation cycles: period and amplitude of Soufriere Hills Volcano, MVO1 Site											
First Deformation Cycle				Second Deformation Cycle				Third Deformation Cycle			
Period (yrs)	Amplitude	Inflation (yrs)	Deflation (yrs)	Period (yrs)	Amplitude	Inflation (yrs)	Deflation (yrs)	Period (yrs)	Amplitude	Inflation (yrs)	Deflation (yrs)
~7.529 ^a	N 70 mm	~ 3.945 ^b	3.584	3.7210	N 55 mm	2.304	1.416	2.841	N 40 mm	2.523	0.318
~7.529 ^a	E 55 mm	~ 3.945 ^b	3.584	3.7210	E 40 mm	2.304	1.416	2.841	E 25 mm	2.523	0.318
~7.529 ^a	V 120 mm	~ 3.945 ^b	3.584	3.7210	V 100 mm	2.304	1.416	2.841	V 80 mm	2.523	0.318

a) This length includes the projected time for inflation prior to the site at MVO1 being placed.

b) This length includes the projected time for inflation prior to the site at MVO1 being placed.

Long-term surface deformation period and amplitudes for the cycles recorded at MVO1 site on SHV.

4.2 Secondary Short Term Deformation Signal

When comparing the older MVO1 time series from SHV using GOA-II (ver. 4.0) versus the new time series from GOA-II (ver. 6.1.2), the daily position solutions show only a slightly lower variance, however there was a greater definition of the “structure” of the entire plot that allowed for a higher frequency short term deformation signal that is superimposed on the longer term deformation of the volcanoes to be clearly noted. In Figure 16, the short term signal seen in the first cycle of MVO1 is shown, the inflation on the left and deflation on the right, with periods and amplitudes marked. The high frequency signal is shown to have an average period of 4.83 months and average amplitude of 52.3 mm change in deformation in the vertical for the inflation period of the first long term deformation cycle. There is an 11.5 month average period and 66.5 mm amplitude for the deflation period during the first long term deformation cycle. The average period and amplitude in the vertical for the inflation during the second long term deformation period are 5.88 months and 43.0 mm, respectively, and for the deflation there is an average change of 44.0 mm. The data are too scattered in the vertical component to constrain the high frequency signal period. In the inflation period of the third long term deformation cycle, the high frequency signal has an average period of 6.00 months and an average amplitude of 36.5 mm, whereas the deflation has an average period of 4.50 months and an average amplitude of 36.0 mm. All computed periods and amplitudes, as well as the averages for the three long term cycles in the latitudinal, longitudinal, and in the vertical can be seen in Table 3.

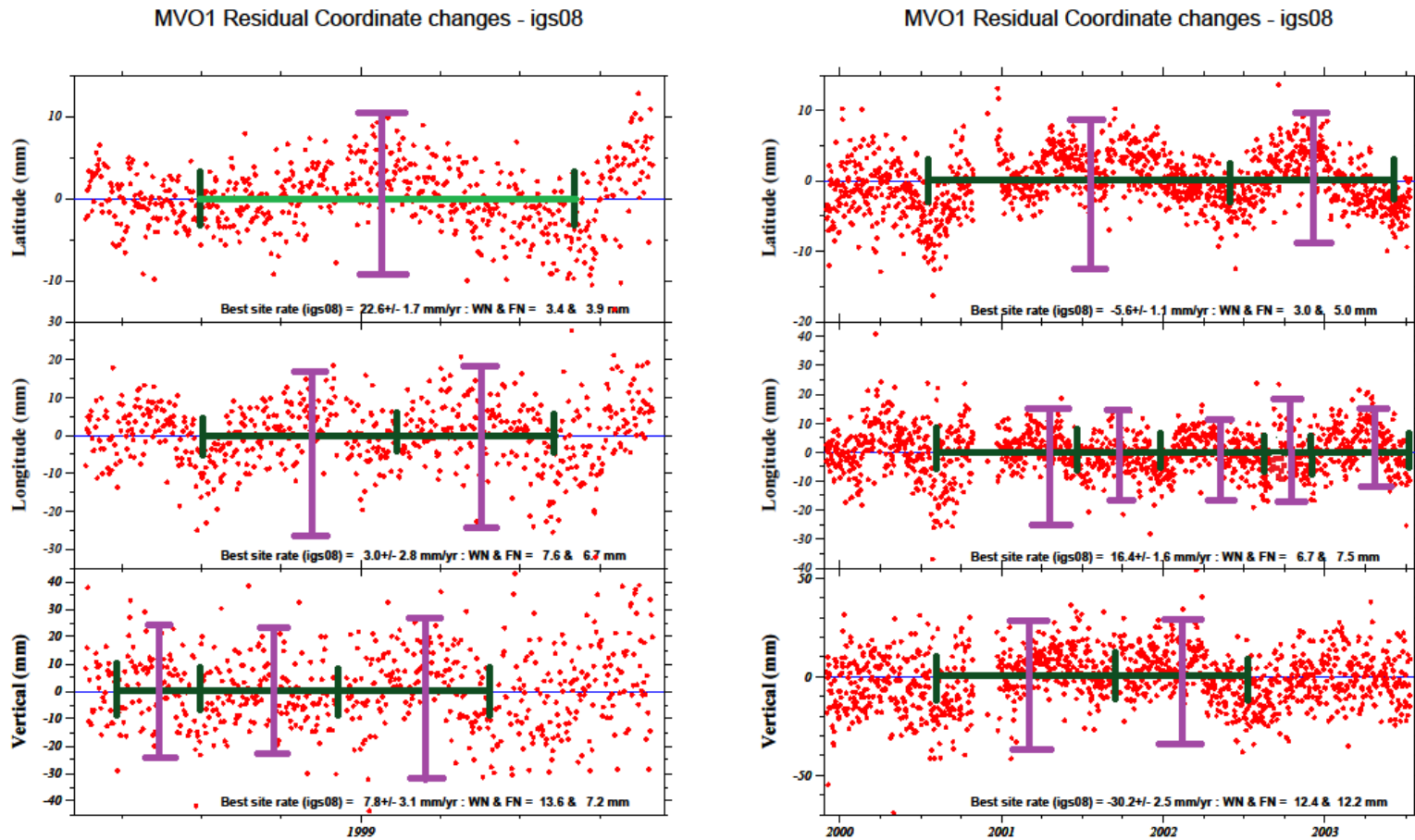


Figure 16 Short term signal periods and amplitudes

MVO1 - first long term deformation period showing short term signal amplitudes in purple and periods in green for the North, East, and Vertical components of both the inflation (left) and deflation periods (right).

Table 3 Short Term deformation period and amplitudes

High Frequency Signal, Short Term Deformation: Periods and Amplitudes																
First Cycle					Second Cycle					Third Cycle						
Cycle Date	Direction	Period (mth)	Amplitude (mm)	AvG (P A)	Cycle Date	Direction	Period (mth)	Amplitude (mm)	AvG (P A)	Cycle Date	Direction	Period (mth)	Amplitude (mm)	AvG (P A)		
Jan98-Nov99	N	14.0	16.5	15.0 16.5	Jul03-Nov05	N	9.50	10.00	8.50 12.67	Apr07-Oct09	N	7.0	10.0	6.63 10.75		
	E	7.5	44.0	7.0 44.0		N	7.00	10.00			N	7.0	10.0			
	E	6.5	44.0			N	9.00	9.00			N	7.5	12.0			
	V	3.5	50.0			E	8.00	25.00			N	5.0	11.0			
	V	5.0	45.0			4.83 52.33	E	6.00			25.00	6.38 25.25	E		5.5	23.0
	V	6.0	62.0			E	4.50	16.00			E	6.0	22.0		E	5.5
E	7.0	35.00	V		5.50	22.00	E	6.0	18.0							
Dec99-Jul03	N	22.5	22.0	17.5 20.5	V	5.50	45.00	5.88 43.00	E	6.0	16.0					
	N	13.0	19.0	V	7.00	40.00	V	7.5	44.0							
					Nov05-Apr07	N	7.50	22.00	7.5 22.0	Apr07-Oct09	V	5.0	41.0	4.5 36.0		
	E	10.5	40.0	E		6.00	37.00	6.0 32.0	V		3.0	31.0				
	E	6.5	32.0	E	6.00	27.00	6.0 32.0	V	5.0		35.0					
	E	8.0	27.0	7.3 32.4	E	6.00	27.00	V	4.0		37.0					
	E	4.5	36.0	V	Scattered	44.00	44.00	V	2.5		28.0					
	E	7.0	27.0					Oct09-Feb10	N		1.8	8.0				
	E	5.0	22.0						E	2.0	15.0	2.0 15.0				
	V	13.5	68.0	11.5 66.5					V	1.3	28.0					
	V	9.5	65.0						V	0.7	28.0	.99 28.00				

* P|A is the average period | average amplitude for each component

** Dates are grouped by little or no surface flux (pink) and dome growth (blue)

The high frequency, short term deformation signal super imposed on the long term cycles seen at MVO1 site.

The stick slip situation modeled by Voight et al. (1999) was used to explain short term deformation that occurred in the upper edifice of the volcano (~<1 km of depth) and lasted from several hours to a little longer than a day. However, when you look at the data from MVO1 and pull out individual epochs of the time series, where the short term signal can be clearly seen, and then correlate this signal with the observed surface volcanic activity recorded by the MVO on Montserrat, we may infer that the same stick-slip situation due to a magmatic plug in the conduit could be controlling this longer duration cyclic deformation. Examining Figure 17, which is the inflation period of the first cycle of MVO1 site on the left, and the deformation period from the first cycle on the right, you can see the short term deformation signal clearly. When comparing this time series to the record of events from the MVO a clear pattern emerges. During periods of little to no dome growth the cycle shows inflation, and during times of dome growth, venting and/or ash emissions, and frequent pyroclastic flows the cycle shows deflation. These events are occurring during the over all long term deformations. So while the entire island of Montserrat is undergoing a long term inflation period there are actually shorter periods, recorded in the short term signal, of deflations that are occurring.

According to Foroozan et al. (2010) from 1995-2009, the SHV system has erupted ~ 1 km³ of mainly andesitic material but the presence of small amounts of basalt mixed in with the erupted andesite implies that there is a deeper supply of hot mafic magma (Elsworth et al., 2008). According to Elsworth et al. (2008), during periods of reinitiated high surface efflux, magma rose quickly and synchronously from a deflating mid-crustal reservoir (at about 12 km) augmented from depth and during repose, the lower reservoir refilled from the deep supply, with only minor discharge transiting to the upper chamber to the surface. Elsworth et al. (2008) used a combination of GPS data with known SHV efflux data and assumed a magmatic system with two Mogi sources, one fixed at 6 and one fixed at 12 km similar to Figure 7 of this study. The additional constraint added from including lava efflux allowed for estimation of fluxes at the base of the crustal magma system, and estimation of the volume changes and fluxes of the two crustal chambers. Elsworth et al. (2008) concluded that the deeper chamber dominated the overall geodetic signal, and that there is a valve mechanism situated between the lower and upper chambers that controlled the magma movement between them. This is a similar idea to the Voight et al. (1999) model, just occurring much deeper in the system. The valve closes off the lower magma chamber and as it

continues to fill with magma from the mantle pressures will build beneath the valve. While the valve between the lower and upper chamber is closed, only the magma that is currently in the upper chamber can be extruded. Based off of the small deformational signal from the upper reservoir Elsworth et al. (2008) inferred that either pressure changes are small and the upper system is largely open, or the upper reservoir is smaller and more geometrically rigid than the lower chamber. Using this geometry, if no magma is being moved from the lower chamber into the upper, this could account for the small extrusions that are occurring during the longer inflation cycles. The larger chamber is inflating, yet none of the magma being stored there can move up the system, so the pressure builds from below, forcing the small chamber to undergo small extrusion and thus deflate. Eventually, the pressure from below will reach a point where the valve can no longer hold, and the magma will be forced up into the upper chamber, and perhaps at that point also be extruded on the surface. However, Mattioli et al. (2010), after comparing numerous models trying to define the SHV magmatic plumbing system, concluded that defining the Mogi sources beneath the SHV based on GPS data alone cannot be done. Complex geometries that include deep, multiple Mogi sources (or by extension of our analysis, other types of deformation sources, for example dikes or sills), are not justified statistically over simpler models. Any number of plausible geometries fit the data equally well when only GPS data are used to condition the model (Mattioli et al. 2010). So in the case of SHV it is highly plausible that there are several different situations occurring in the plumbing system that cause the deformation signals recorded at the GPS sites.

Since the long term signal and the short term signal noted in the MVO1 time series seem to be showing very similar patterns, just on different time scales, it can be inferred that they may in fact be controlled by the same type of situations. If the long term signal is being controlled by the influx of magma into the lower, much larger magma chamber and how often it is moved into the upper and extruded onto the surface, then it is not much of a stretch to infer that the short term signal could be controlled by a similar situation (*i.e.* the Voight et al. (1999) model) occurring in the upper conduit. But if the short term signal is controlled by the stick-slip situation created by a stiffened magmatic plug, why are there even smaller episodes of inflation and deflation occurring during the short term deformations? This could be due to degradation of the plug, but only enough to allow seepage of magma around the edges or through cracks, thus a short period of dome growth occurs during an overall period of inflation. It stops when the

magma degasses and crystallizes to a point to patch the defect in the plug. If this were happening at the same time that the lower chamber were valved off from the upper chamber as Elsworth et al. (2008) suggests occurs, this would account for very short lived events. The small pressure build up from below would dissipate quickly with extrusion and degassing allowing for the magmatic plug to solidify again. This process would work in reverse for long term deflation periods, when short term inflations occur due to cessation of dome growth, due to flux rate slowing because the upper chamber is once again valved off from the lower as it is replenished from the mantle. This decrease in flux could allow for a thin, weak plug to be formed. Such decrease in flux rate can be seen recorded in Figure 17, in section 6, that began in May 2002. The inflation continues through December of 27, 2002 even though flux rate increases a small amount during this time from $\sim 0.1 \text{ m}^3\text{s}$ by the end of July to $\sim 0.86 \text{ m}^3\text{s}$ by September 2002 (MVO). Flux rate jumps higher and several large lobes and a large spine are extruded from the very end of December 2002 through July of 2003. This deflation period ends abruptly in mid July of 2003 with a major dome collapse, and several Vulcanin eruptions with the losing approximately 120 million m^3 in pyroclastic flows, the largest volume event of the current eruption (MVO). The short term signal can be correlated with MVO observations through the entire current eruption.

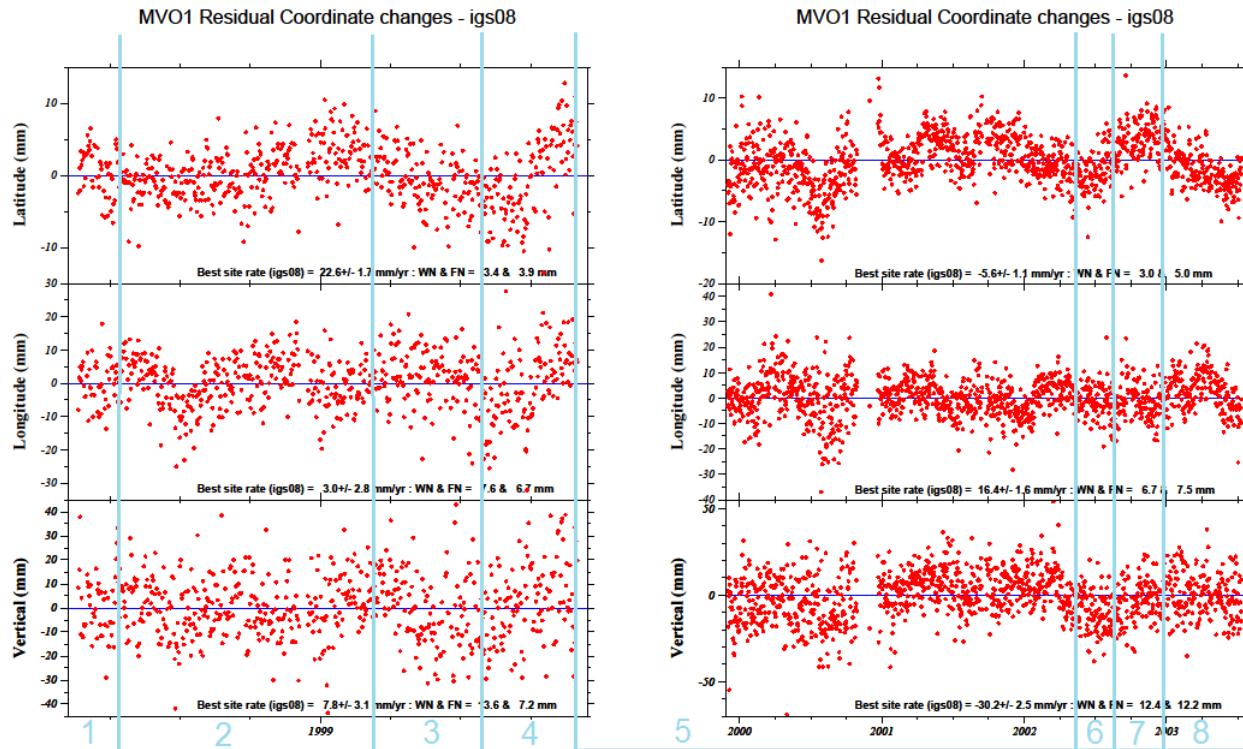


Figure 17 Short term, Voight et al. (1999) stick-slip correlation

MVO1 site inflation and deflation periods, respectively, of the first cycle. Blue lines demarcate record of dome building and repose from visual observations made of volcanic edifice that are correlated to MVO records. Link below is chronological history of SHV eruption from start to present day.

<http://www.mvo.ms/about-volcanoes/soufriere-hills-volcano/chronology-of-current-eruption>

1. Dome growth noted on SHV
2. Dome growth ceases and begins to degrade. Small collapses and pyroclastic flows occur
3. Major venting and ash emissions occurring with pyroclastic flows, increase in seismic activity
4. Activity decreases, dome continues to degrade, no new growth
5. Begin new dome growth, intermittent collapses and pyroclastic flows
6. Decline in activity, magmatic flux rate estimated at $\sim 0.1\text{m}^3/\text{s}$
7. Dome growth rate increases, several major collapses occur from end of September- December
8. Dome growth resumes with several new lobes developing.

4.3 A “Hitch” in the Cycle

While quantifying the period and amplitude of this higher frequency signal of the individual epoch time series of the MVO1 site, an interesting signal was discovered. During each of the inflation, or repose periods of SHV, there appears to be a “hitch”, or hiccup in the inflation that occurs during the last third to quarter of the cycle, where the volcanic edifice undergoes a small deflation period before resuming the inflation (Figure 18). This small deflation “hitch” also appears to be increasing in amplitude, with SHV undergoing a greater deflation before resuming inflation, as each cycle occurs. This was previously undetected in the data as the variance in the position estimates were too high to clearly see this trend and the extended time series has made this discovery even more pronounced. In the individual time series for MVO1 during the repose period, Figure 19, the vertical change in the first cycle, January 1998 – November 1999, is ~ 40 mm. In Figure 20, the vertical change of the second cycle, July 2003 – November 2005, is ~ 45mm, while in Figure 21, the vertical change in the third cycle, April 2007 – October 2009, is ~ 50 mm. Table 4 shows an estimation of the deformation changes (in mm), which occurred during the deflation “hitch” in for each period in the north, east, and vertical.

MVO1 Residual Coordinate changes - igs08

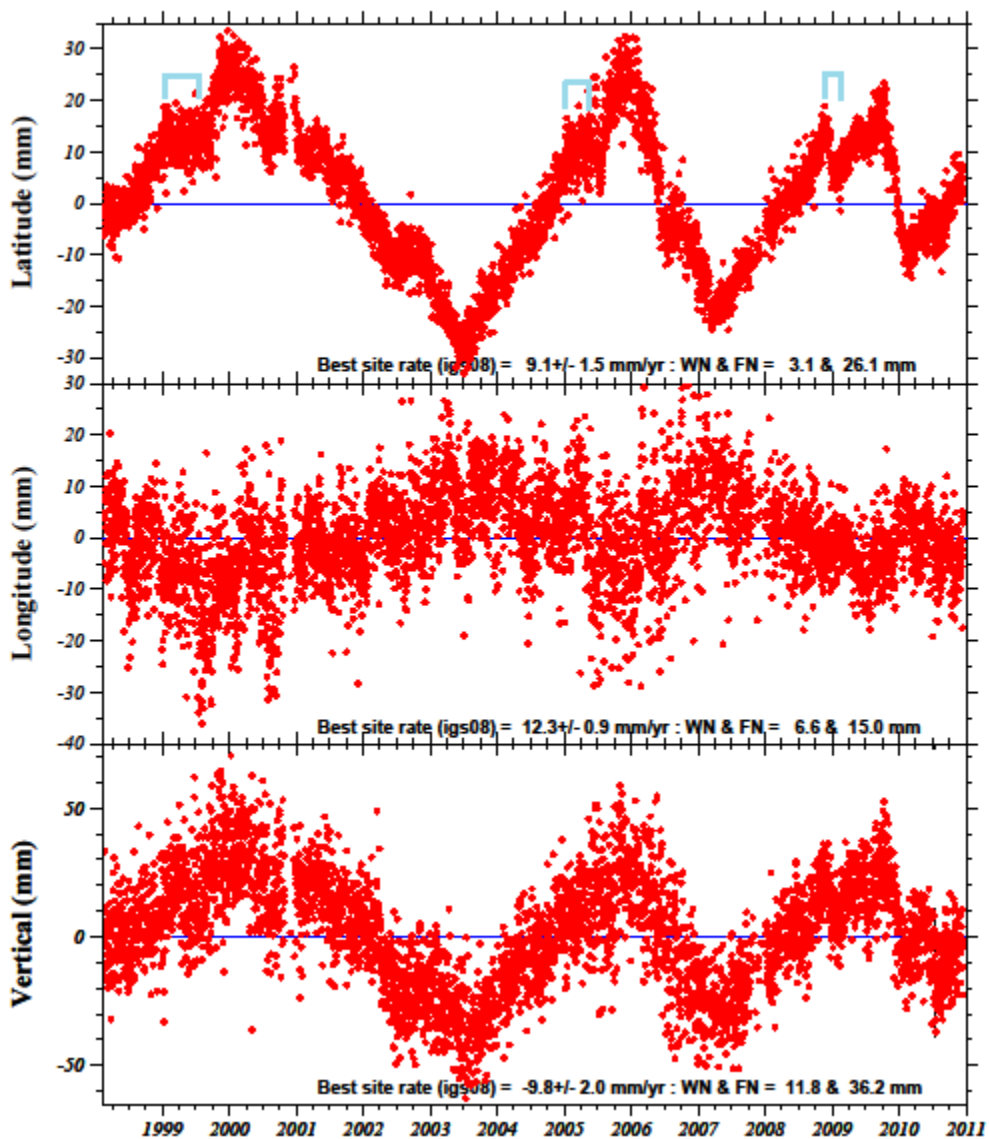


Figure 18 MVO1 "hitch"

MVO1 extended time series showing the "hitch" period denoted by the blue lines.

Table 4 Deflation "hitch" approximations.

Aproximation of Deformation occurring during deflation "Hitch" period during repose cycles								
First Cycle			Second Cycle			Third Cycle		
Epoch Dates	Deflation (mm)	Time to Peak*	Epoch Dates	Deflation (mm)	Time to Peak*	Epoch Dates	Deflation (mm)	Time to Peak*
Jan98-Nov99	N 10.0	~ 9.5 months	Jul03-Nov05	N 17.0	~ 8.0 months	Apr07-Oct09	N 17.0	~ 11.5 months
	E 22.0			E 36.0			E 17.0	
	V 40.0			V 45.0			V 50.0	

* Time to Peak is the an approximation of the start time of the hitch occurrence with respect to the peak of inflation during the cycle

Approximated deformation in millimeters and approximation of start time to peak of inflation

MVO1 Residual Coordinate changes - igs08

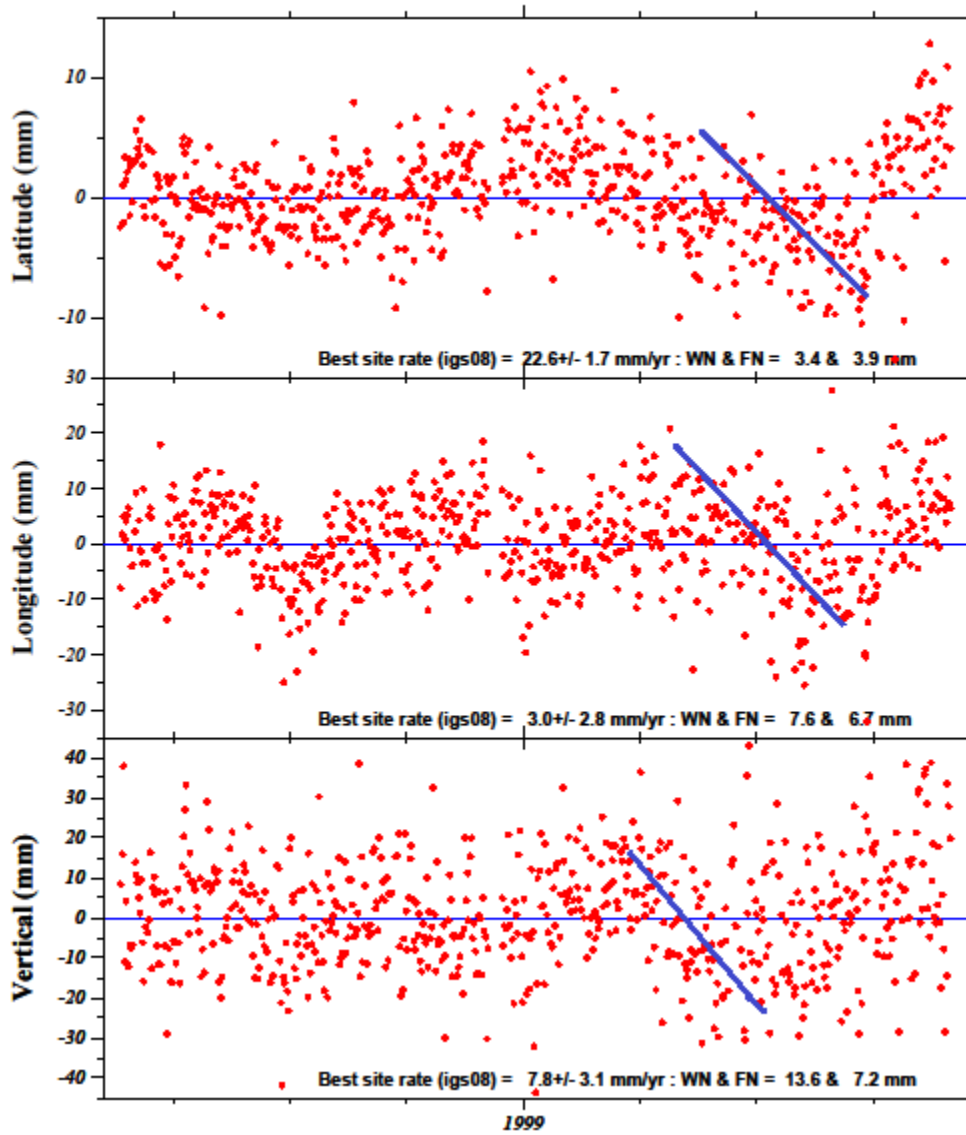


Figure 19 First hitch episode.

MVO1- Inflation period during first long term cycle. Blue line represents the "hitch" deflation period, but does not represent the quantification of the deflation.

MVO1 Residual Coordinate changes - igs08

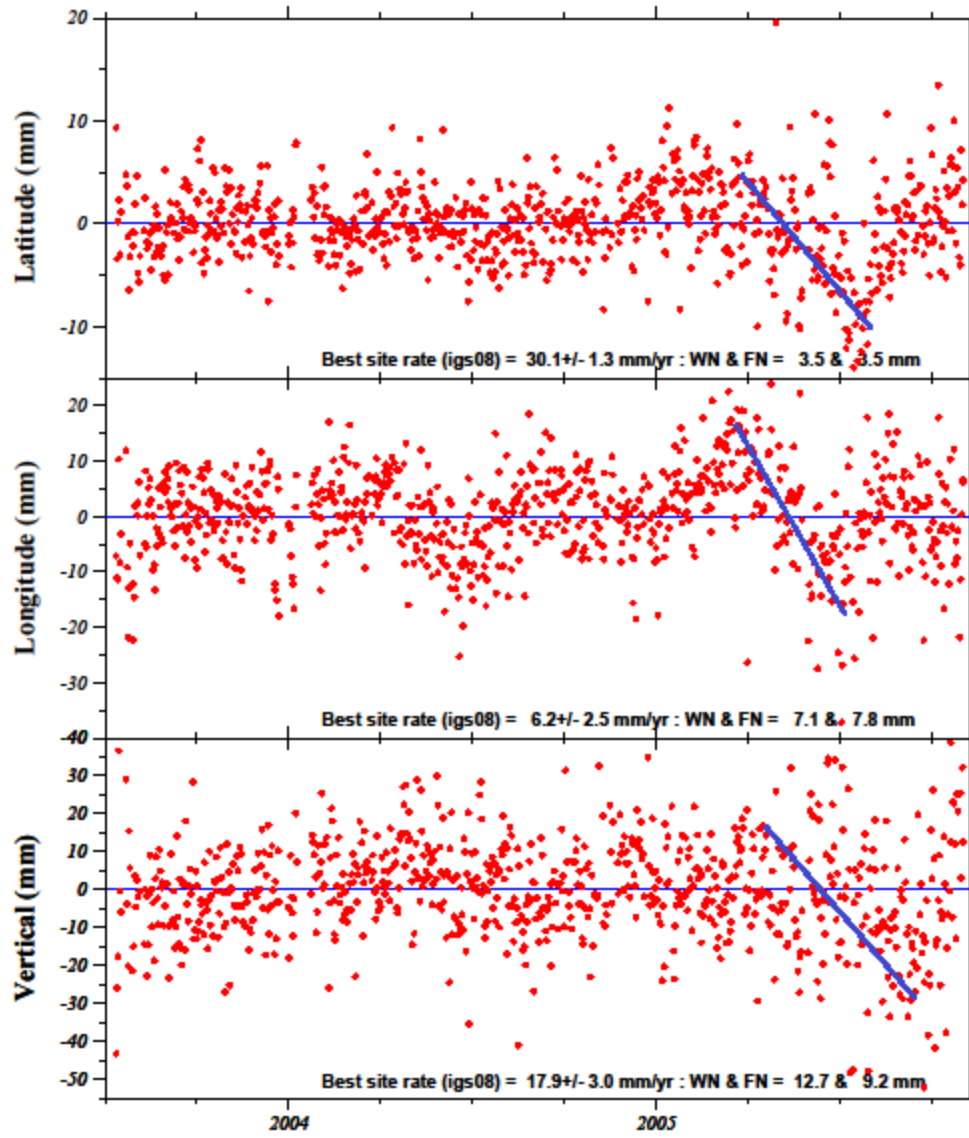


Figure 20 Second hitch period.

MVO1- Inflation period during the second cycle. Blue line represents “hitch” deflation period, does not represent the quantification of the deflation.

MVO1 Residual Coordinate changes - igs08

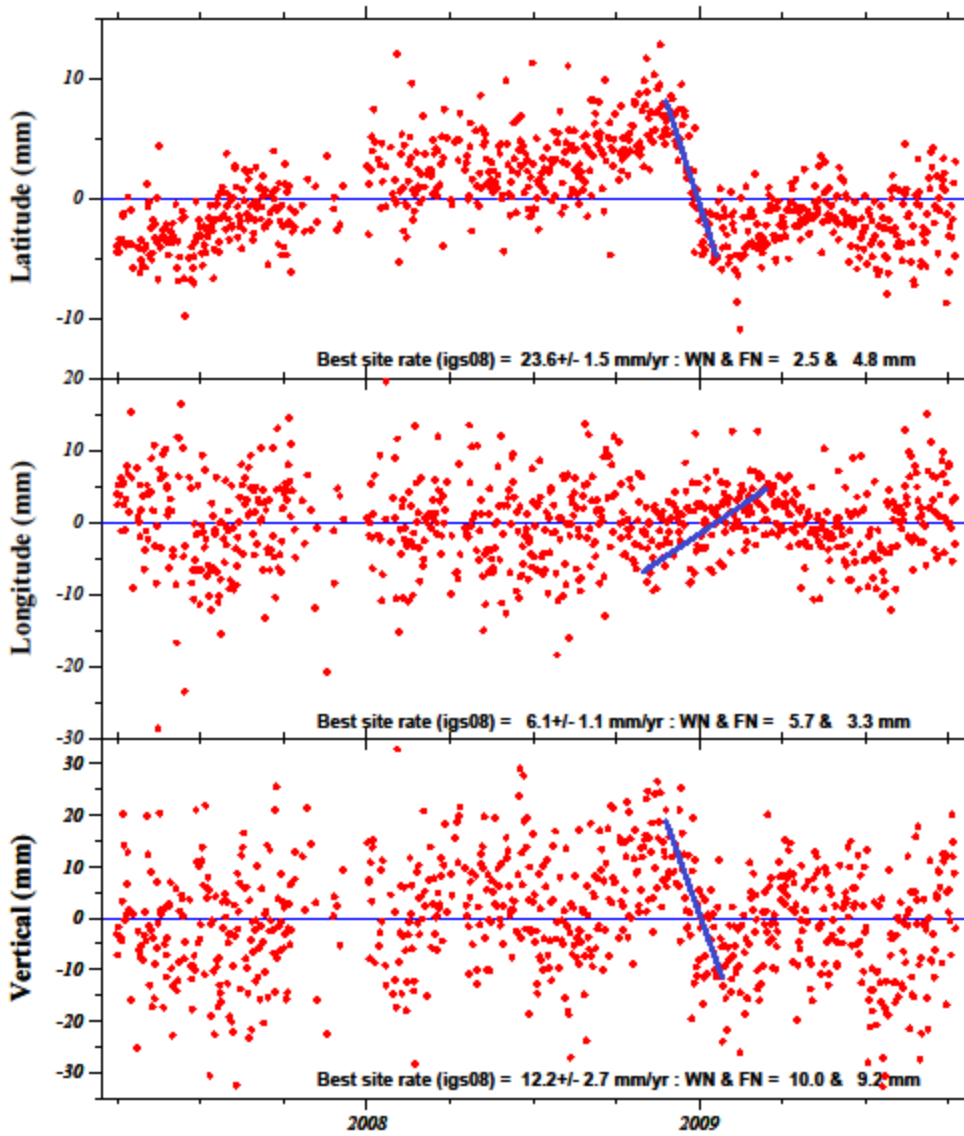


Figure 21 Third hitch period.

MVO1 - Inflation period during third cycle. Blue line represents the "hitch" deflation period, does not represent the quantification of the deflation. Green stars are an estimation of an average position for the beginning and end of the "hitch" period

This “hitch” in the overall inflation period could be related back to the model proposed by Voight et al. (1999) as well, and could be due to failure of the magmatic plug. As previously noted when correlating the short term cycle to surface volcanic observations recorded by the MVO it was noted during the time period that is the “hitch” the volcano is indeed undergoing a release of pressure. In all three of the inflation “hitch” periods there is an increase in seismic activity as well as an increase in ash emissions and phreatic explosions occurring. In both the first and second cycles the SHV is noted to have new gas vents opening in the craters as well as increased ash emissions. The last cycle, which has the largest deflation to date, it is noted that there are several large phreatic explosions that occur during December of 2008 as well as a new large dome being formed. All such activity ceased on January 4th of 2009, when the deflation ceases and inflation resumes. It is reasonable to assume that these episodes of the volcano releasing pressure could indeed be due to a partial magmatic plug failure occurring when the pressure in the upper conduit reached a point too great for the plug to withstand. As for the duration and amplitude change of the “hitch” period increasing with each successive cycle, this could be due to degradation of the magmatic system as a whole. With each cycle, the edifice of the volcano becomes more highly fractured due to weakening from earthquakes and fracturing from degassing and thus it takes less pressure build up to cause the slip situation to occur again and the plug to be removed from the conduit. It could also in part be due to the cooling of the system as a whole and the influx rate of magma from the lower chamber into the upper chamber being less, thus the system takes a longer time to reestablish inflation. Lower flux rate of hot magma and greater ability to degas and for the magma to expand would cause the magma to stiffen more quickly once the inflation resumes and thus the pressure to build more quickly and the plug fails much quicker after the inflation resumed. This would explain why the volcanic edifice is failing to show the same amount of overall “inflation” deformation for each successive cycle.

This overall cooling would also explain why the deflation period of each cycle is also occurring at a significantly faster rate with each progressive cycle. As the magma around the edges of the upper chamber and the conduit to the surface cools and solidifies, the volume of the chamber is reduced. If the flux rate of magma from the lower chamber into the upper chamber is also decreasing with each cycle then the upper chamber will deplete more quickly and then would it take a longer to refill in comparison to the time it takes for it to empty and the edifice to deflate.

In the Elsworth et al. (2008) model, they proposed that the third cycle showed the highest flux rate of the three cycles to date. If this model is correct and the flux rate did in fact jump to a higher rate, perhaps the lack of symmetric deformation, that according to Denlinger and Hoblitt (1999) you should see with an average flux rate of $6 \text{ m}^3/\text{s}$, and the fact that the edifice failed to return to even close to the same pre – inflation position could be that this was not the “true” repose period. This deflation could have just been a longer sustained, second “hitch” period, as the edifice deflated to $\sim -18\text{mm}$, only a 10 mm greater deflation, in the vertical component, than that of the first “hitch in the cycle (Figure 18). In the second deflation period SHV returned to nearly the same pre-inflation position. In the first cycle it is unknown if the edifice also acted as elastically as it did in the second cycle, but can be inferred that it did when you look at Figure 15, and projected line for inflation. This second “hitch” occurring in the third cycle could be due to a further degradation and failure of the magmatic plug that took the system longer to recover from, since the flux rate was much higher than that in the second cycle. Or this could be due to the proposed valve between the upper and lower chambers being open at the time and thus there was a much larger volume of magma brought to the surface allowing for a much greater deflation. During this time the MVO has record of an increase of large VT/hybrid earthquakes, and increase in dome building and pyroclastic flows occurring from late October of 2009 through early January of 2010. From January 8, 2010- February 11, 2010 there were several large earthquake swarms accompanied by large vulcanian eruptions, pyroclastic flows and dome collapses. Since we do not have access to any of the data the periods of time after the end of December 2010 this theory is hard to prove, however based off of record from the MVO public record, it does appear that SHV has continued to undergo inflation up through the end of the record to date of March 23, 2012. Thus the inflation that begins again in mid February of 2010 could indeed just be a continuation of the third cycle inflation and a complete deflation of the system has not in fact, occurred.

4.4 New Site Velocities

Reprocessing the raw data also produced new site velocities with respect to a fixed Caribbean plate. Table 5 shows these site velocities and errors calculated using GOA-II (ver.4) and for comparison the new site velocities for HERM and MVO1 that were generated using GOA-II (ver. 6.1.2). Included are the extended time series velocities and errors as well. Table 5 shows that the velocities have changed a small amount with the reprocessing, but not significantly enough to make any real difference with respect to the Caribbean plate as compared to the analysis in 2010.

Table 5 - Site velocities for ITRF05 and IGS08 processing.

Calculated GPS site velocities for HERM and MVO1 for 1995-2010 - adapted from Mattioli et al., 2010.																								
ITRF2005 data is original data from Mattioli et al., 2010.																								
Site ID	Time Span Years	Number Sta.-Days	ITRF2005 (mm/yr) - No Common Mode Correction ^a													CAR rate ^b (mm/yr)		CAR Fixed Velocity ^c (mm/yr)					Epoch ^d	
			Vn	Error	WN	FN	Ve	Error	WN	FN	Vv	Error	WN	FN	RWN	Vn	Ve	Vn	Error	Ve	Error	Vv		Error
HERM	0.5028	61	62.1	11.9	5.9	6.8	-3.6	17.0	8.5	9.7	-75.5	28.3	16.8	15.4	1.0	14.96	11.63	47.14	11.90	-15.23	17.00	-75.50	28.3	01OCT95-31DEC97
HERM	1.7370	433	90.4	4.6	5.8	10.8	75.8	4.6	8.8	10.7	2.0	5.0	16.6	11.1	1.0	14.96	11.63	75.44	4.60	64.17	4.60	2.00	5.0	01JAN98-30NOV99
MVO1	1.7753	609	26.0	1.7	5.0	3.8	6.1	2.7	8.4	6.2	7.4	4.4	14.3	10.5	1.0	14.95	11.60	11.05	1.70	-5.50	2.70	7.40	4.4	01JAN98-30NOV99
HERM	3.4658	992	69.7	2.8	4.2	13.5	56.4	3.5	7.4	16.6	-56.3	3.7	14.1	17.4	1.0	14.96	11.63	54.74	2.80	44.77	3.50	-56.30	3.7	01DEC99-12JUL03
MVO1	3.6110	1240	-4.3	1.2	3.7	5.6	17.0	1.2	6.9	5.3	-33.3	2.5	13.0	12.2	1.0	14.95	11.60	-19.25	1.20	5.40	1.20	-33.30	2.5	01DEC99-12JUL03
HERM	2.3041	664	21.5	4.4	3.7	14.0	25.9	4.4	7.2	13.9	20.7	3.3	12.9	10.2	1.0	14.96	11.63	6.54	4.40	14.27	4.40	20.70	3.3	13JUL03-01NOV05
MVO1	2.2932	725	29.3	1.2	3.0	3.3	4.3	2.0	6.7	6.0	22.4	2.4	11.2	7.1	1.0	14.95	11.60	14.35	1.20	-7.30	2.00	22.40	2.4	13JUL03-01NOV05
HERM	0.8658	230	16.0	3.0	4.0	3.0	-1.6	6.2	8.1	6.8	-81.6	6.9	14.1	6.9	1.0	14.96	11.63	1.04	3.00	-13.23	6.20	-81.60	6.9	02NOV05-14SEP06
MVO1	1.3945	337	-27.1	1.7	3.0	2.7	25.3	2.5	8.5	3.9	-60.2	4.2	12.1	7.1	1.0	14.95	11.60	-42.05	1.70	13.70	2.50	-60.20	4.2	02NOV05-01APR07
MVO1	1.5021	330	29.1	1.3	3.1	2.0	5.1	2.6	9.3	4.3	20.3	3.5	11.0	6.3	1.0	14.95	11.60	14.15	1.30	-6.50	2.60	20.30	3.5	01APR07-01OCT08
Site ID	Time Span Years	Number Sta.-Days	IGS08 (mm/yr) - No Common Mode Correction ^a													CAR rate ^b (mm/yr)		CAR Fixed Velocity ^c (mm/yr)					Epoch ^d	
			Vn	Error	WN	FN	Ve	Error	WN	FN	Vv	Error	WN	FN	RWN	Vn	Ve	Vn	Error	Ve	Error	Vv		Error
HERM	0.5028	61	54.2	12.5	7.9	6.8	6.4	20.4	16.3	9.7	1.1	35.1	30.6	15.4	1.0	14.96	11.63	39.24	12.50	-5.23	20.40	1.10	35.1	01OCT95-31DEC97
HERM	1.7370	433	87.2	4.9	4.2	11.7	72.4	6.2	10.9	14.6	0.7	5.2	14.8	12.0	1.0	14.96	11.63	72.24	4.90	60.77	6.20	0.70	5.2	01JAN98-30NOV99
MVO1	1.7753	609	22.6	1.7	3.4	3.9	3.0	2.8	7.6	6.7	7.8	3.1	13.6	7.2	1.0	14.95	11.60	7.65	1.70	-8.60	2.80	7.80	3.1	01JAN98-30NOV99
HERM	3.4658	992	68.3	3.7	3.4	18.1	56.8	4.4	7.4	22.1	-54.6	4.6	12.7	22.8	1.0	14.96	11.63	53.34	3.70	45.17	4.40	-54.60	4.6	01DEC99-12JUL03
MVO1	3.6110	1240	-5.6	1.1	3.0	5.0	16.4	1.6	6.7	7.5	-30.2	2.5	12.4	12.2	1.0	14.95	11.60	-20.55	1.10	4.80	1.60	-30.20	2.5	01DEC99-12JUL03
HERM	2.3041	664	24.2	6.1	4.8	19.8	29.1	6.0	10.1	19.4	18.8	4.1	16.0	12.2	1.0	14.96	11.63	9.24	6.10	17.47	6.00	18.80	4.1	13JUL03-01NOV05
MVO1	2.2932	725	30.1	1.3	3.5	3.5	6.2	2.5	7.1	7.8	17.9	3.0	12.7	9.2	1.0	14.95	11.60	15.15	1.30	-5.40	2.50	17.90	3.0	13JUL03-01NOV05
HERM	0.8658	230	12.8	3.9	6.5	3.9	7.8	7.4	15.3	7.1	-73.5	10.9	21.5	10.8	1.0	14.96	11.63	-2.16	3.90	-3.83	7.40	-73.50	10.9	02NOV05-14SEP06
MVO1	1.3945	337	-25.9	2.4	4.2	4.3	26.0	2.6	9.3	4.4	-55.8	3.2	15.5	5.1	1.0	14.95	11.60	-40.85	2.40	14.40	2.60	-55.80	3.2	02NOV05-01APR07
MVO1	1.5021	330	29.2	1.1	2.8	1.4	5.4	2.0	7.2	3.3	16.8	2.9	10.5	5.2	1.0	14.95	11.60	14.25	1.10	-6.20	2.00	16.80	2.9	01APR07-01OCT08
HERM ^e	0.8356	305	5.0	1.7	2.7	1.8	4.3	2.2	4.5	2.4	2.9	5.7	12.1	7.1	1.0	14.96	11.63	-9.96	1.70	-7.33	2.20	2.90	5.7	03OCT08-09OCT09
MVO1	2.5232	783	23.6	1.5	2.5	4.8	6.1	1.1	5.7	3.3	12.2	2.7	10.0	9.2	1.0	14.95	11.6	8.65	1.50	-5.50	1.10	12.20	2.7	01APR07-09OCT09
HERM	0.3178	96	91.8	20.5	4.6	6.8	-36.2	29.6	7.4	9.7	-287	48.2	13.9	15.4	1.0	14.96	11.63	76.84	20.50	-47.83	29.60	-287.40	48.2	10OCT09-02FEB10
MVO1	0.3178	107	-74.4	14.5	2.6	6.8	37.3	20.9	5.3	9.7	-135	33.7	10.7	15.4	1.0	14.95	11.6	-89.35	14.50	25.70	20.90	-134.90	33.7	10OCT09-02FEB10
HERM	0.8329	183	12.7	8.7	2.8	6.8	5.6	12.4	5.3	9.7	7.7	20	11.6	15.4	1.0	14.96	11.63	-2.26	8.70	-6.03	12.40	7.70	20.0	03FEB10-01JAN11
MVO1	0.8329	304	25.0	1.8	2.9	1.5	4.7	2.6	5.4	2.4	-21.2	6.2	10.8	6.6	1.0	14.95	11.6	10.05	1.80	-6.90	2.60	-21.20	6.2	03FEB10-01JAN11

a) Calculated site component velocities assuming linear motion. Vn = North, Ve = East, Vv = Vertical velocities and corresponding 1 sigma errors. WN = white noise, FN = flicker noise, and RWN = random walk noise components (Mao et al., 1999).
 b) Caribbean plate motion in ITRF05 from DeMets et al., 2007
 c) Linear site component velocities and 1 sigma errors after removal of fixed CAR motion in ITRF05.
 d) Epoch over which the linear velocities are calculated. The boundaries are demarked on time-series in Figs. 5.4a-e. Data are grouped by dome growth (blue) and little or no surface efflux (pink).
 e) Extended time series for HERM site represented by yellow and MVO1 represented by orange.

The top portion of the table is the velocities for the HERM and MVO1 sites calculated in GIPSY-OASIS II (ver. 4.0) and the bottom is the recalculated site velocities calculated in IGS08 from GOAII (ver. 6.1.2). Table includes the extended time series data.

4.5 HERM - A model of deformation due to dike emplacement

The HERM site, located ~1.6 km from the vent of SHV, has in the past been routinely omitted for use in the many models created to determine the cause of the long-term surface deformation recorded by GPS at SHV (see for example Mattioli et al., 2010). This is most likely due to the HERM site data not behaving in the same manner as rest of the GPS sites located on SHV. From personal conversations with G. S. Mattioli, it is to be understood that the HERM site is located on a wedge of land that sits at the peak of the volcano in between two valleys. These valleys are routinely the paths that pyroclastic flows, lahars, and debris avalanches follow when any activity occurs at SHV. Thus it is a reasonable to assume that the unconsolidated volcanic sediments that make up the edifice of SHV could show weakening with the continuous removal of sediment from these valleys. With the weakening in these valleys, the wedge of land between the two valleys in essence almost an island, and thus would not move as a whole with the rest of SHV. This decoupling could allow for the distinct deformation recorded at the HERM site.

Using the near vertical dike estimated by Mattioli et al. (1998), which was modeled to be one kilometer long and situated near the vent of SHV under the HERM site, we hope to show that the displacement of the surface due to the (> 1 meter) opening of this dike could indeed have cause this wedge of land to be pushed out away from the rest of the volcanic edifice. If this portion of the edifice is no longer coupled with the rest of SHV, it could deform in a much different way than the rest of the volcano. Figure 21 shows how this hypothesis might work.

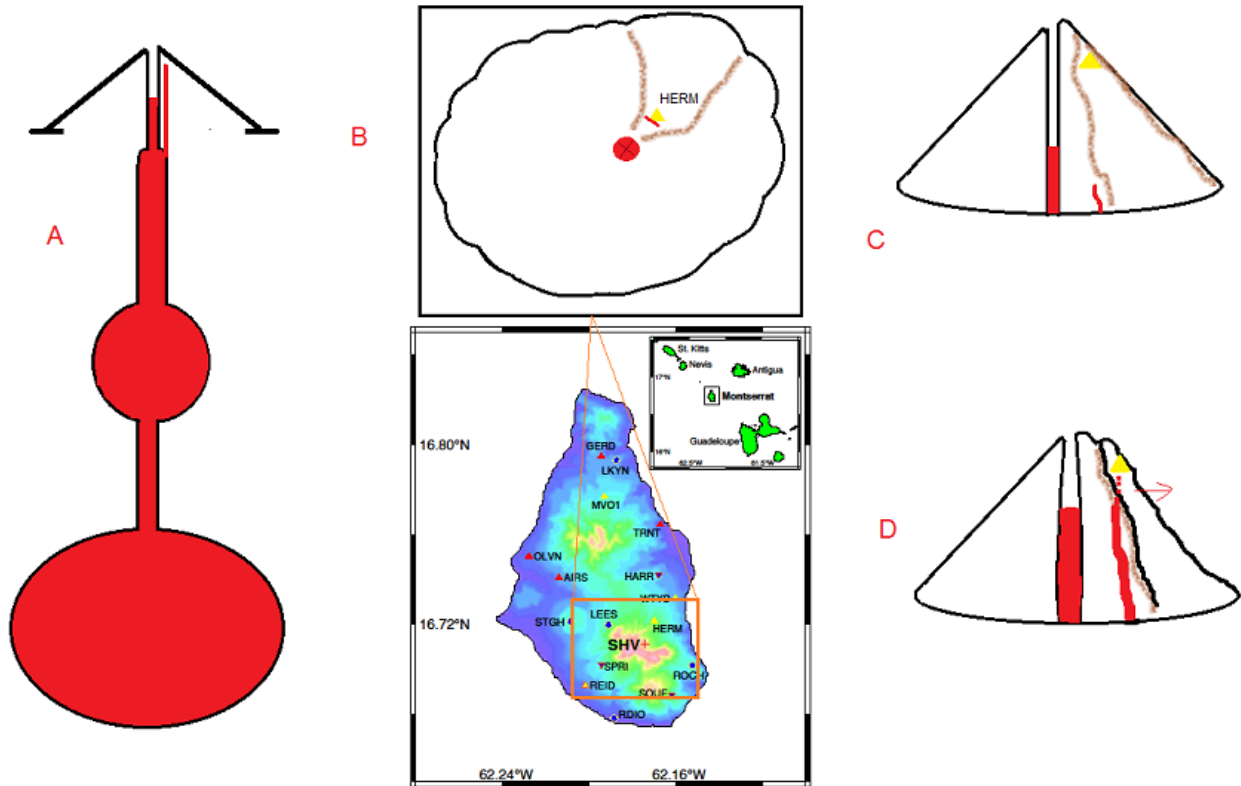


Figure 22 Dike Emplacement Hypothesis

A. Model of SHV magmatic system with hypothesized dike emplaced. **B.** Simplified view of SHV showing location of the vent, red circle with X, HERM site (yellow triangle) and dike (red line) in relation to the HERM site. **C.** Shows HERM site situated between two valleys (brown lines) before dike expansion. **D.** Dike expansion pushing the decoupled “wedge” of land HERM site is situated upon away from the rest of the edifice.

This hypothesis gives a very plausible explanation for why HERM does not show the more cyclic inflation and deflation periods that the rest of the sites record. It has been proposed that the dike began as a non-feeder dike that opened approximately in meter in width, as no surface efflux of lava was seen. When activity began in 1995 at SHV, the edifice began to inflate as magma was filling the upper magma chamber. A weakened area or crack in the edifice filled with magma but it did not reach the surface. The Voight et al. (1999) model proposed a rheologically stiffened magmatic plug forming in the conduit that stopped the magma from reaching the surface. This plug would cause pressure to build in the upper edifice of the volcano and could cause cracks to widen without having any magma being extruded. The location of the dike, being situated under an area that had thinner crust, located in the valleys, allowed for the wedge to be pushed out away from the rest of the edifice. According to Voight et al. (1999), hybrid

earthquake swarms during this inflation have been theorized to have caused hydrofracturing and allowed the pressurized gases to escape from the upper conduit, thus relieving pressure and deflation occurred with no magmatic effusive activity noted, often at a much quicker rate than inflation. The hybrid swarms began when inflations were underway and stopped near the peak of inflation or the start of deflation. Tiltmeters recorded surface deformation that indicated the pressure changes in the magma were located at shallow depths (<1 km). These earthquakes could have easily caused an already weakened area of the volcanic edifice, namely in the valleys, to fracture even more, causing this area to become more decoupled with each successive earthquake swarm.

Once the dike transitioned from a non-feeder dike to a feeder dike, with each new pulse of magma that was pushed through the dike, the area would undergo a small inflation, and when magma flow slowed, a small deflation. However, due to the initial opening of the dike causing the wedge to be pushed away from the edifice, it acts almost as a completely separate entity and does not show the larger scale inflations and deflations that SHV is undergoing.

Modeling done with MATLAB based Coulomb 3.3 (Toda et al., 2005; Lin and Stein, 2004), showed that the strain that a 1 kilometer dike opening up >1 meter beneath the HERM site causes a displacement of greater than 10.0 mm (see Figures 23-27). As the HERM site sits directly in the area most affected by the strain caused by this dike opening, the hypothesis of this causing the unique deformation recorded at this site, is justified. Greater opening of the dike, after several pulses of magma are pushed through for example, would cause even more strain to be imposed on the area. If for example the dike was opened to a width of ~3 meters, it can be seen from the model that this creates a much greater displacement of the edifice, especially in the area where the HERM site is situated (see Figures 28-32). While the deformation of the edifice is mostly controlled by the magma that is being pushed through the conduit leading from the magma chamber to the surface, the inflation of the magi source situated ~5 km below would also have an effect on the edifice as well. Further modeling should be done to couple the inflation of that magi source and the dike to determine just how much it would affect the HERM site.

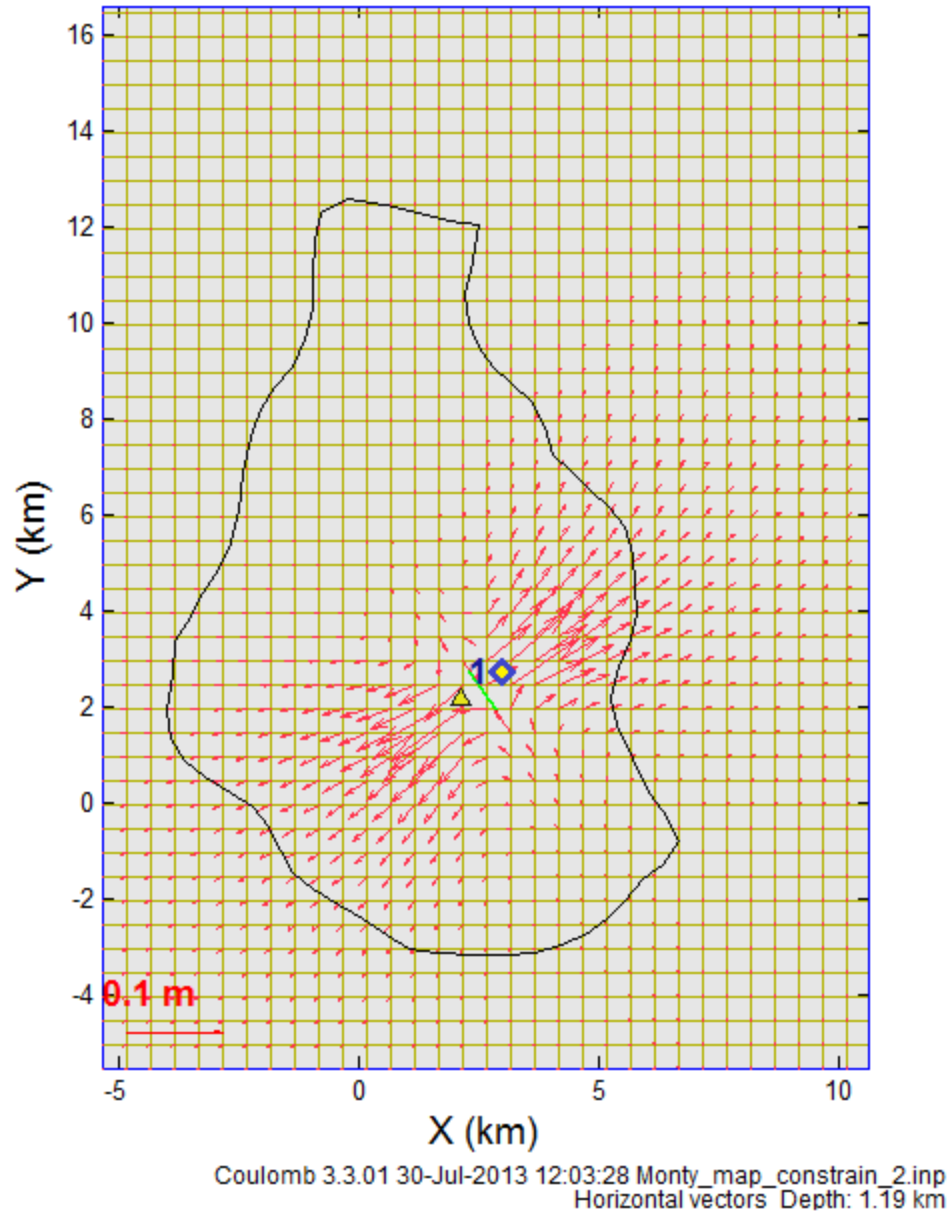


Figure 23 Horizontal Displacement Vectors for dike opening 1 meter

Yellow triangle is Coulomb 3.3 produced overlay of SHV vent according to known latitude and longitude measurements. Green line labeled with number 1 is the dike. HERM site is the yellow/blue diamond.

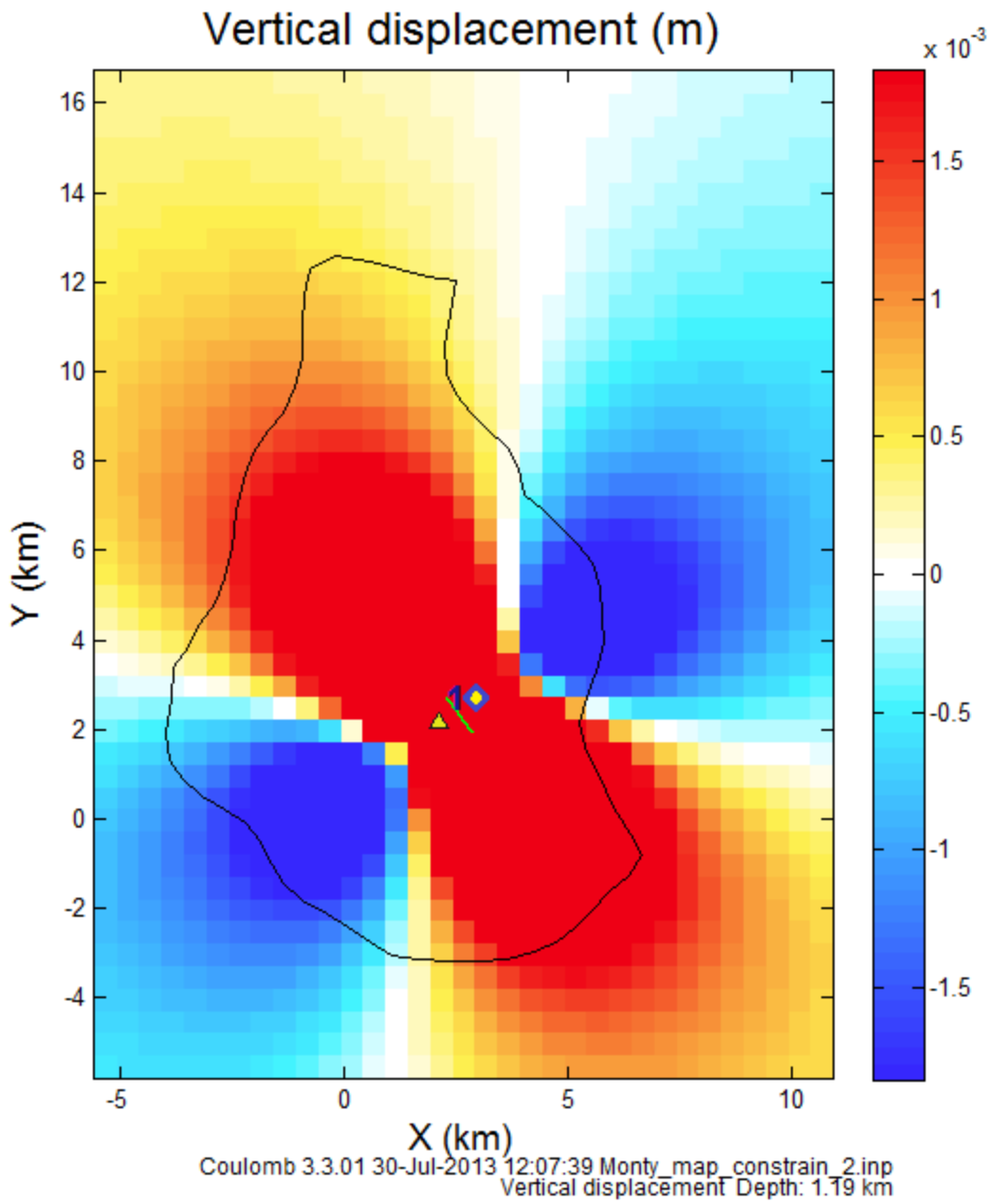
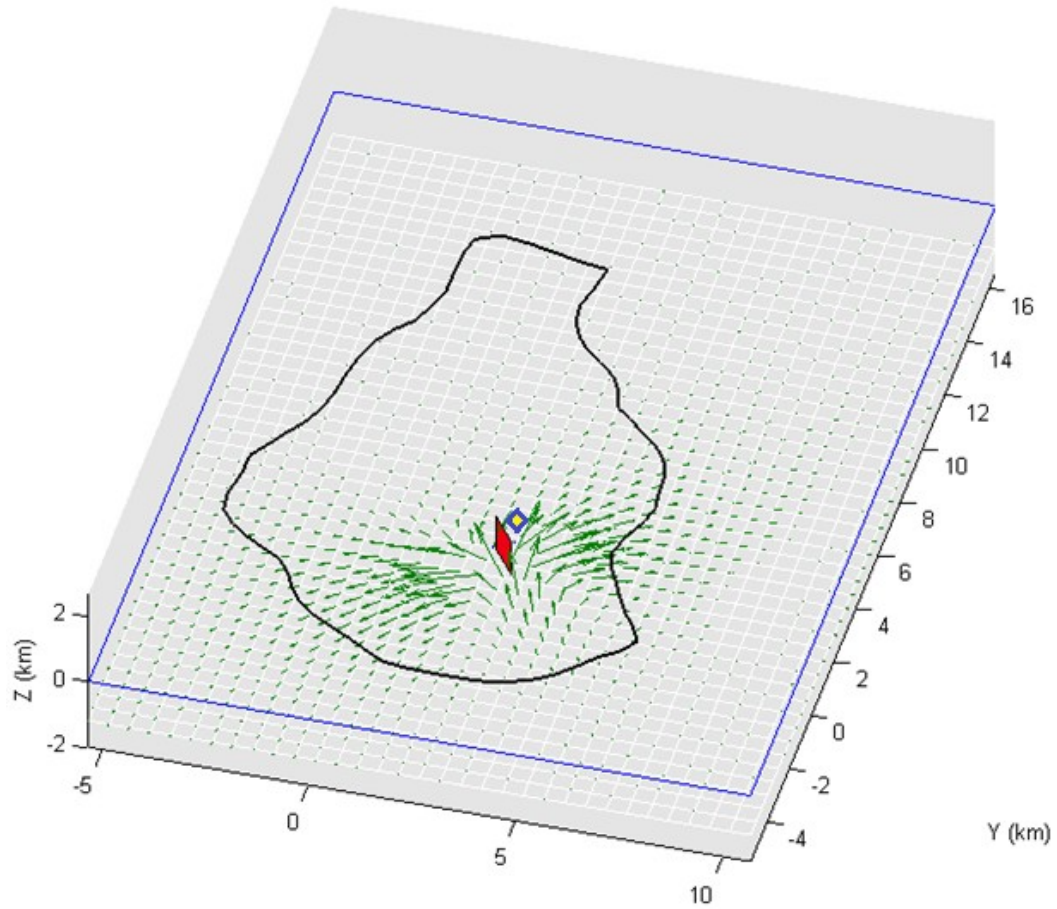


Figure 24 Vertical Displacement

Yellow triangle is Coulomb 3.3 produced overlay of SHV vent according to known latitude and longitude measurements. Green line labeled with number 1 is the dike. HERM site is the yellow/blue diamond.



X (km)
3D displacement vectors

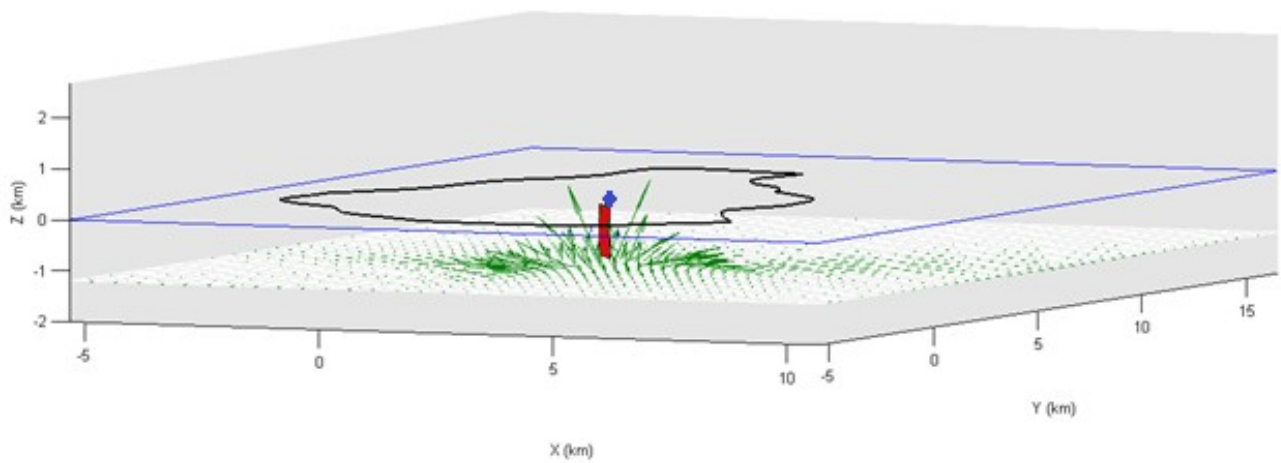


Figure 25 Vertical Displacement Vectors in 3D view

Green Arrows are vertical displacement for dike opening 1 meter. Red rectangle is the dike. HERM site is the yellow/blue diamond.

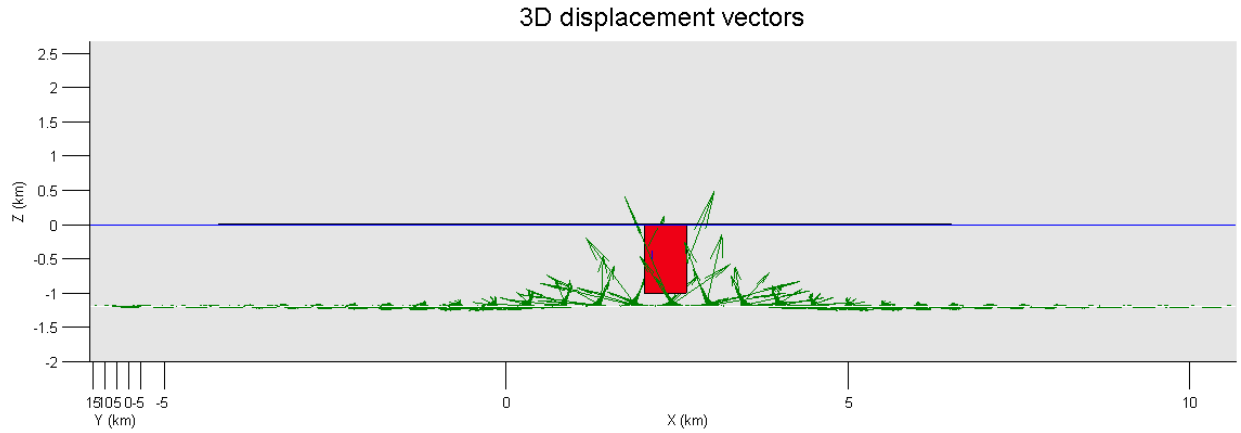


Figure 26 Horizontal view of Vertical Displacement vectors

Green Arrows are vertical displacement for dike opening 1 meter. Red rectangle is the dike.

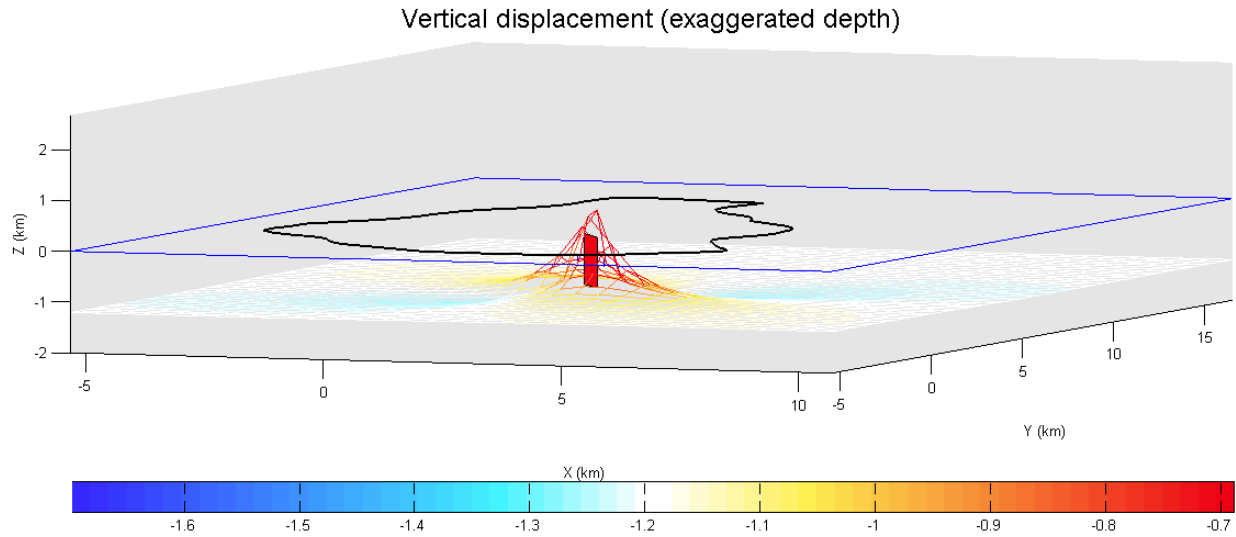


Figure 27 Vertical Displacement Wire Frame Drape

Red rectangle is the dike opening 1 meter. Vertical Exaggeration is X 10000.

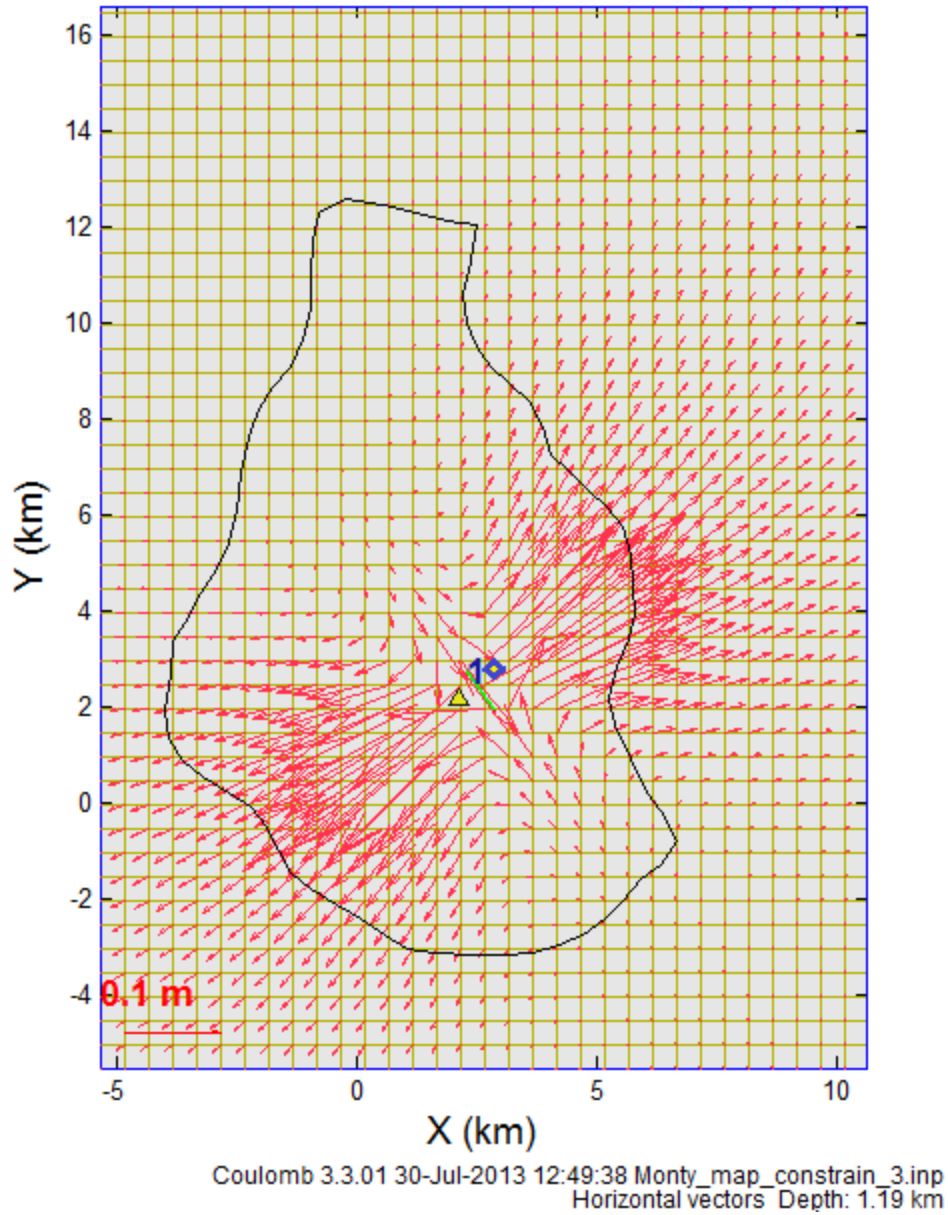


Figure 28 Horizontal Displacement Vectors for 3 meter dike opening

Yellow triangle is Coulomb 3.3 produced overlay of SHV vent according to known latitude and longitude measurements. Green line labeled with number 1 is the dike. HERM site is the yellow/blue diamond

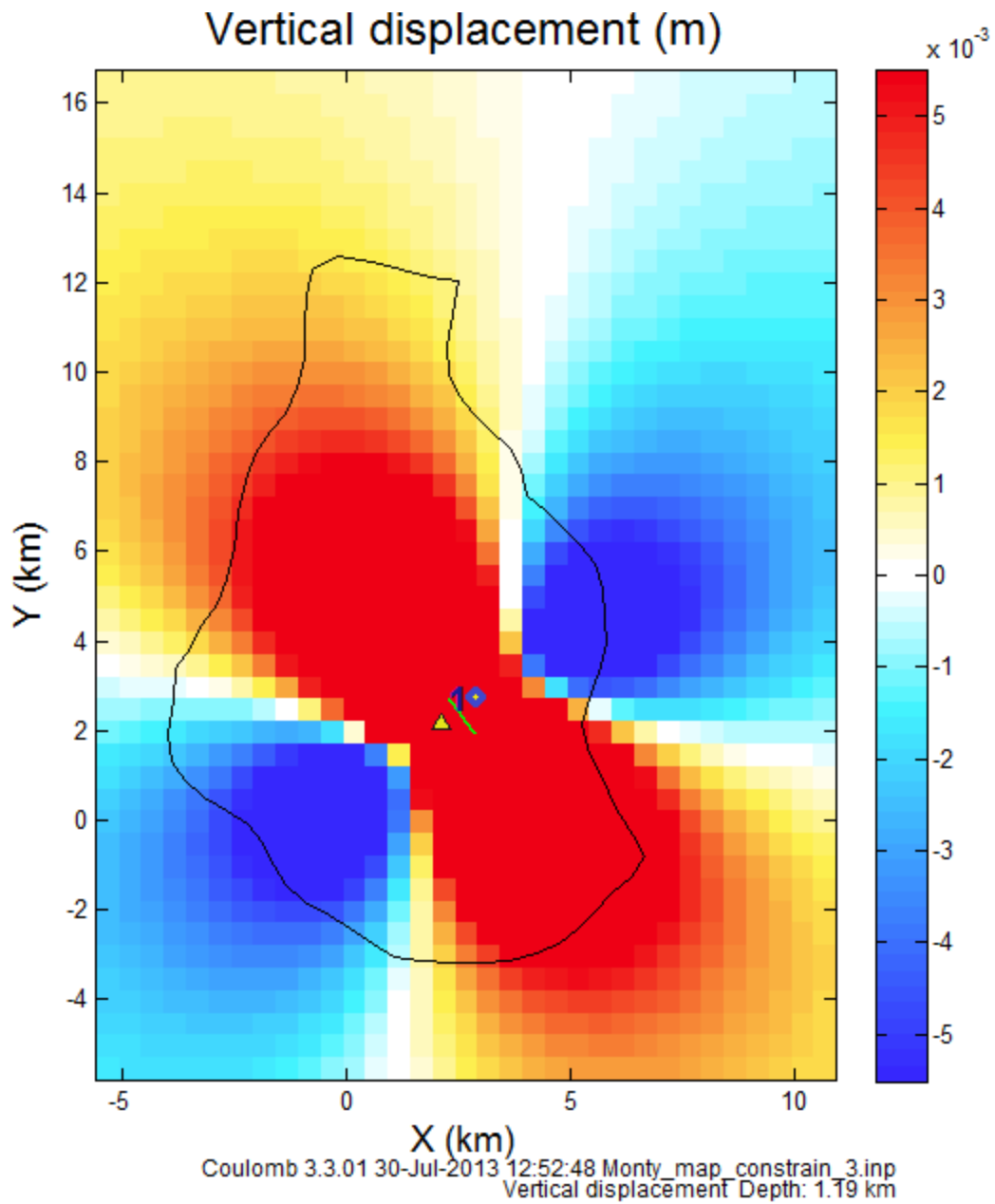
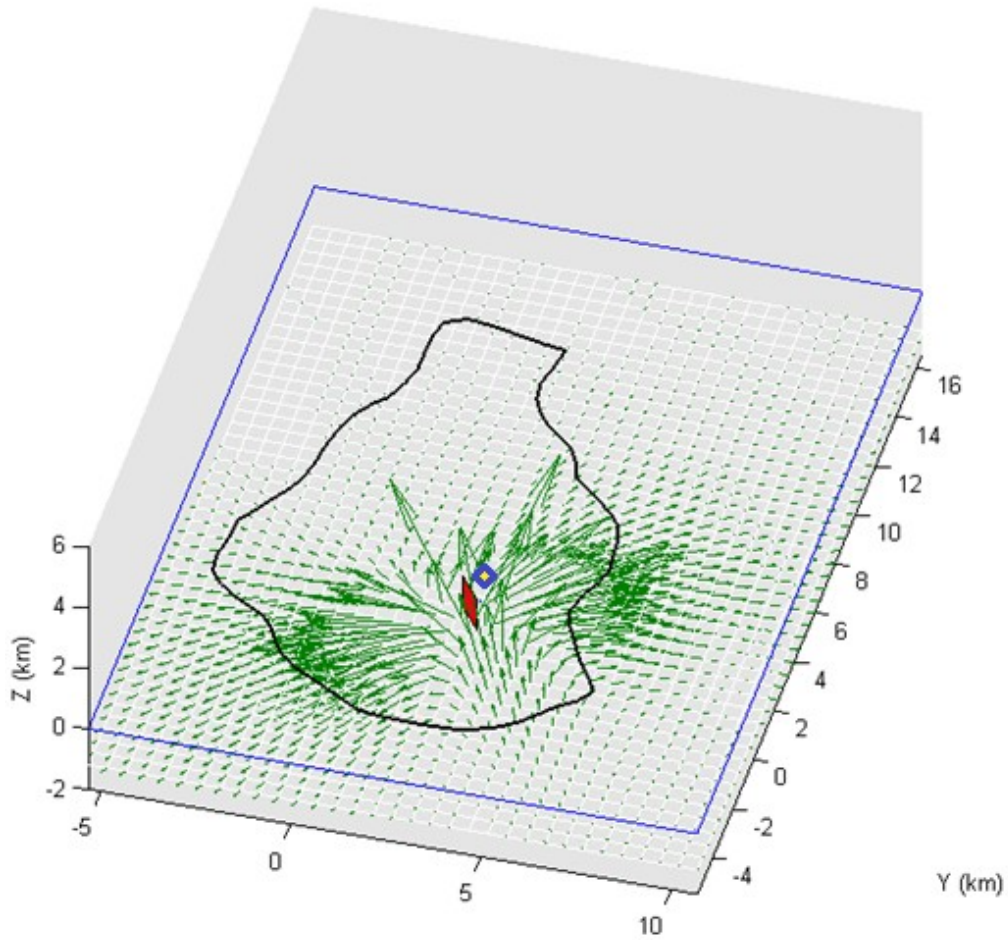


Figure 29 Vertical Displacement

Yellow triangle is Coulomb 3.3 produced overlay of SHV vent according to known latitude and longitude measurements. Green line labeled with number 1 is the dike. HERM site is the yellow/blue diamond



X (km)
3D displacement vectors

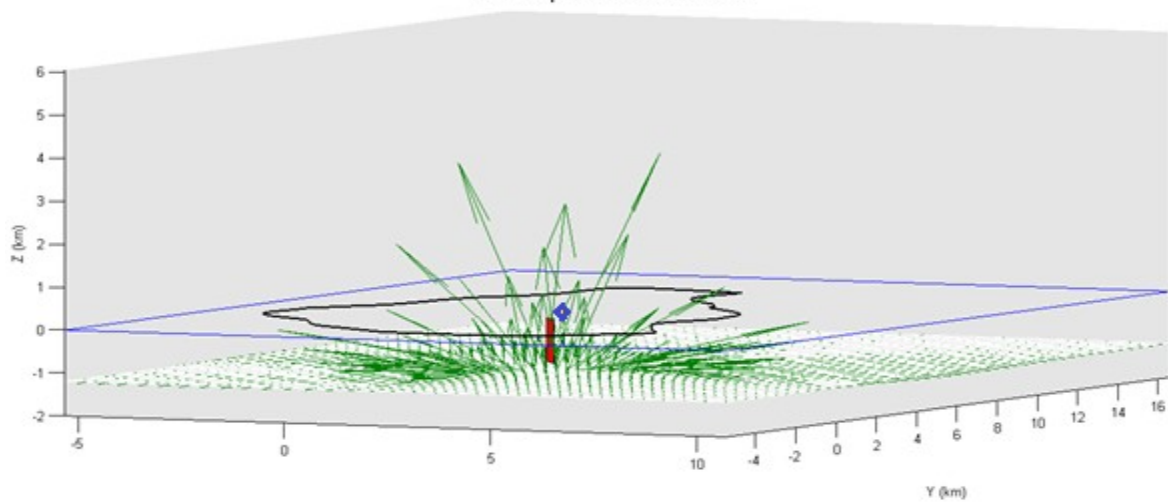


Figure 30 Vertical Displacement Vectors

Green Arrows are vertical displacement for dike opening 3 meters. Red rectangle is the dike. HERM site is the yellow/blue diamond.

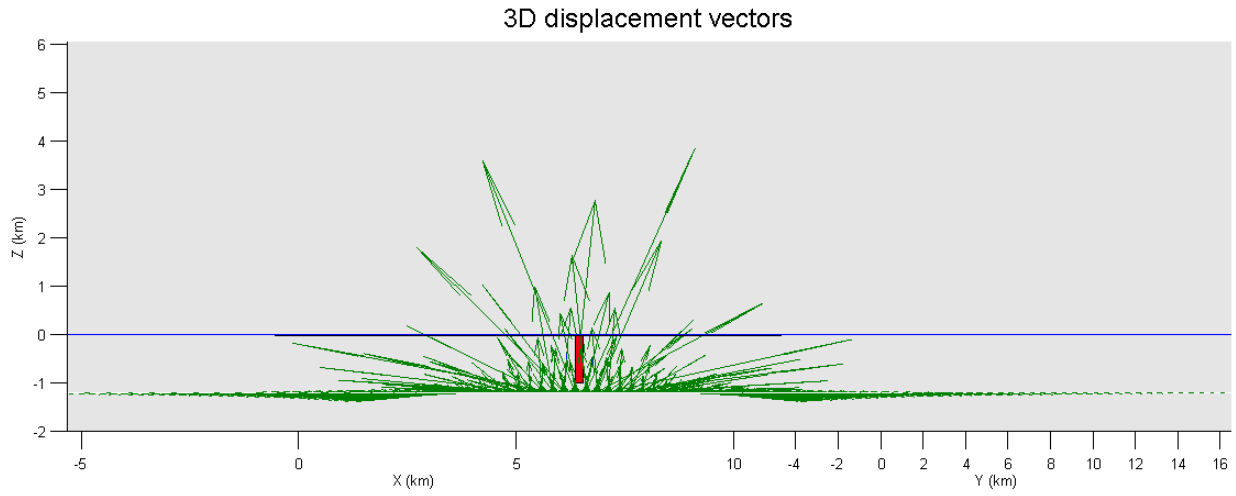


Figure 31 Horizontal View of Vertical Displacement Vectors

Green Arrows are vertical displacement for dike opening 3 meters. Red rectangle is the dike.

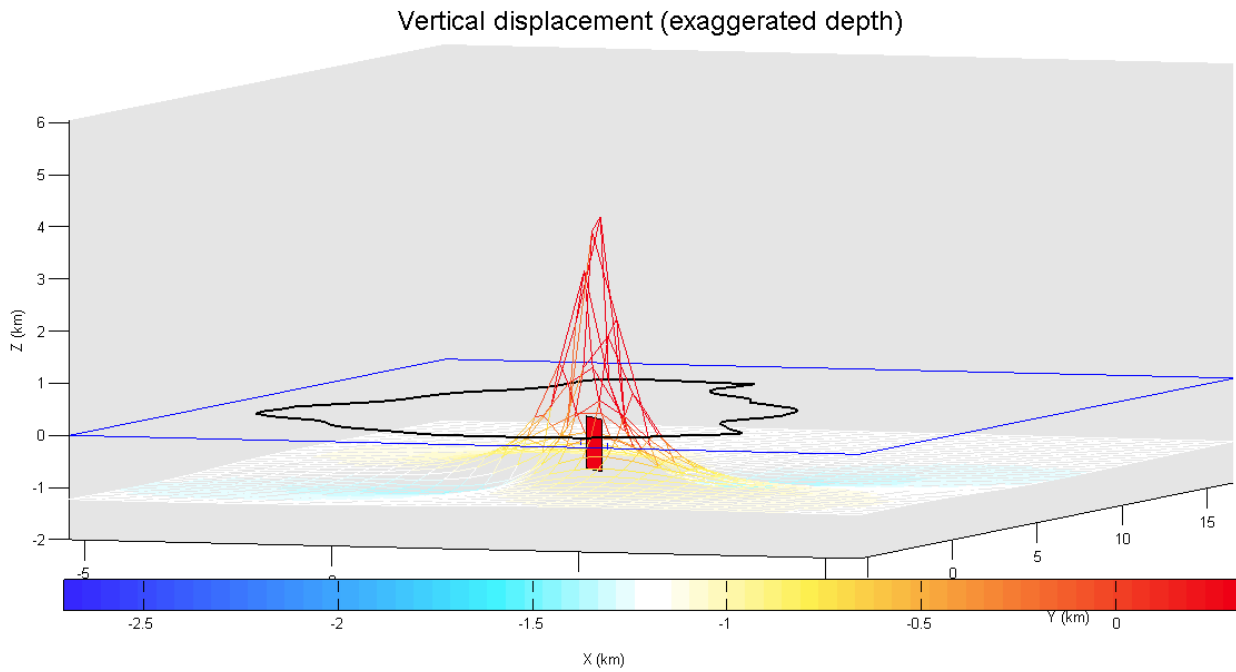


Figure 32 Vertical Displacement Wire Frame Drape

Red Rectangle is the dike opening 3 meters. Vertical displacement exaggerated by 10000.

4.6 Reprocessing using GOA-II (ver.6.2)

Near the end of this study, the Geodesy Lab received and updated its processing procedures and updated to latest version of GOA-II. Error estimates were also fixed in a program called SuperVel that is also used in the processing that had been causing errors to be overestimated in GOA-II (ver. 6.1.2). The reprocessing of the HERM data was run with single receiver ambiguity resolution on and off.

Reprocessing with ambiguity resolution on gives an even more precise daily point position for each day (see Appendix B). This allows for smaller variations in ground deformation to be noted in the time series.

After the reprocessing was completed with ambiguity resolution turned on, an amazing discovery was made. It appears that there is a possible third deformation signal in the MVO1 site that is super imposed on top of the short term signal detailed in this study. The short term signal that was first discovered with the GOA-II (ver. 6.1.2) reprocessing that was outlined in previous chapters now appears to show a near annual duration, with a period of 12-18, while the new signal has a much shorter duration of around 3-5 months. What was originally thought to be part of the second signal, showing shorter periods now appears to be this third signal.

Due to time constraints, only a qualitative analysis was done on this third signal. Figures 33-35 below show the third signal that is super imposed on top of the already known short term signal. The figures show the clearer approximately annual period for the second deformation signal and the shorter period signal overlaying it. The green and blue lines used to highlight the individual signals are drawn in by hand into the figures, based off of personal observations and may not be a true representation of the signal. In some periods the new third signal is harder to decipher in all three plots of the time series, as it is sometimes closely following the longer duration signal, but in others it is quite clear (see Figure 35). As for the causation of this very short term signal, one could only hazard a guess at this point. It could be unloading of unconsolidated volcanic debris from the edifice due to lahars, and rock falls associated with seismicity, very short lived inflations due to small period dome growth and venting. This theory could also account for the periods of time when the third signal is not as easily defined or nearly follows the second signal. During periods of quiet on SHV where little to no seismicity is occurring and only small amounts of rain fall occurs would lead to period of little to no unloading of surface debris being recorded, and thus the signal is not is weak to not present.

The reasoning behind the theory that there are two separate signals and not just one is due to the lack of the third signal reaching the same level of deflation noted in the longer second signal. This can be most clearly seen in Figure 33 where the cyclic movement is easily noted in the north component of the time series. In the largest second signal period here, denoted by the green line, it is seen at the beginning of this period the inflation period began at approximately -9 mm in mid July of 2000. The deflation returns it to almost the same position of -9 mm in late June of 2002. However it is noted that the edifice of SHV, during the smaller inflations and deflations that occur in between these two points of time, fails to deflated to that original position, and only obtains a deflation of around -2 to -4 mm. This trend can be seen throughout the time series in all three directional plots. This trend is what led to the determination that there was likely a third signal being recorded here at SHV.

Another thing of interest to note from the reprocessing with ambiguity resolution on is that the BGGY site which was used in this study as a site that showed little variation in movement as a comparison for the SHV sites now shows slight cyclic movement as well. While the movement is nowhere near as dramatic as the SHV sites, it does have implications of its own. This site was previously believed to be a relatively stable site that only underwent small surface deformations and generally showed the same movement as the Caribbean plate. So with these new results, gives rise to new questions? Is this type of movement associated with more sites in the Caribbean? Is this a localized phenomenon, or does this cyclic movement occurs on more if not all of the Lesser Antilles Arc islands? Perhaps if more GPS data sets for the islands in the Lesser Antilles Arc are reprocessed with GOA-II (ver. 6.2) new light can be shed on the movement of complicated Caribbean plate. The signal noted here at the BGGY site opens thought to a new theory to try and explain the third signal noted at the MVO1 site on SHV. Could this third signal possibly be a common mode noise, created by movement of the entire Caribbean plate? The BGGY site was chosen as a stable site to compare SHV sites to because it is not situated on or near any active volcano, and thus the movement recorded there is thought to be due to Caribbean plate movement. The signal duration recorded at BGGY closely mirrors the signal at MVO1 (Figure 36), especially in the east panel of the BGGY time series, thus lending credence to the theory that they could be caused by the same movement, (*i.e.* Caribbean plate movement).

MVO1 Residual Coordinate changes - IGS08 stacovs used AMB

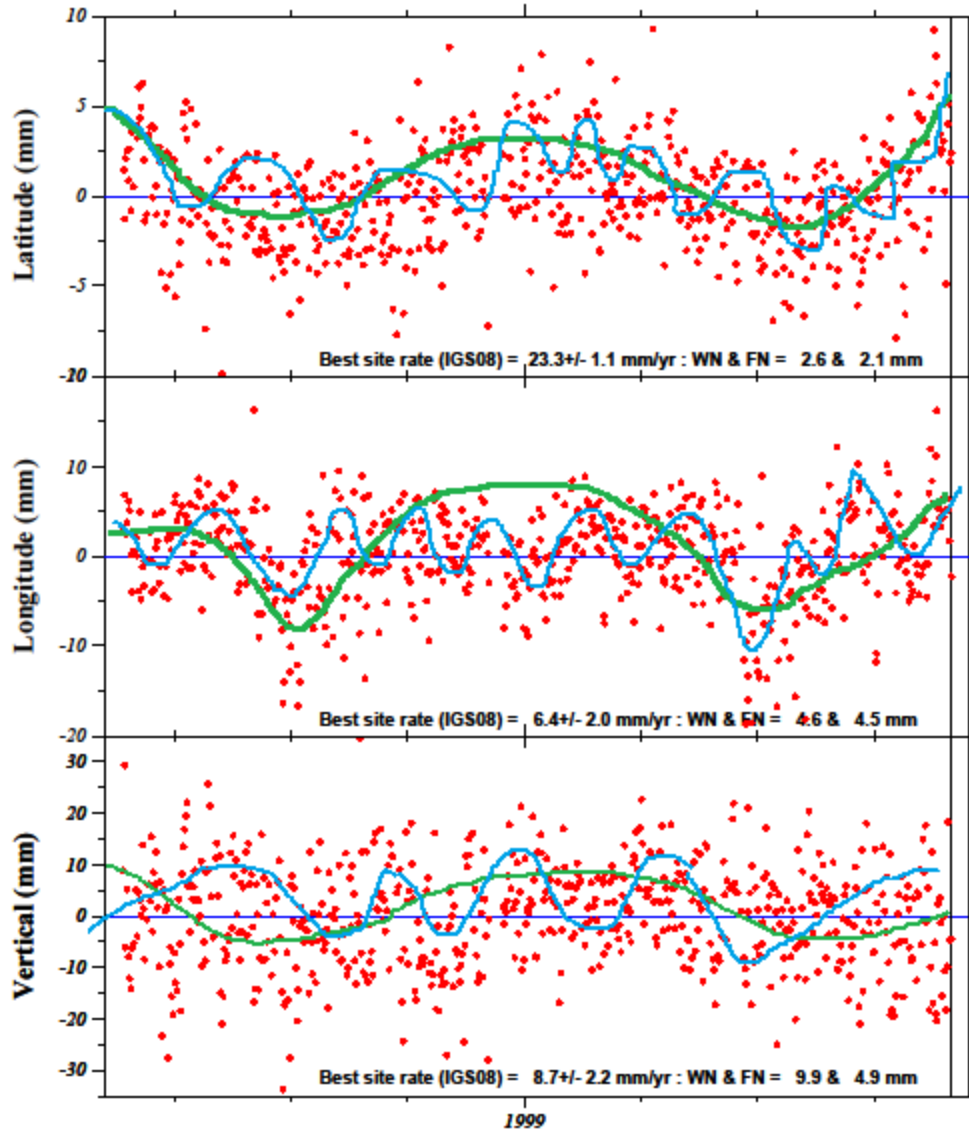


Figure 33 Possible Third Deformation Signal

The third signal that is superimposed on top of short term signal is shown here. The hand drawn green line represents the reanalyzed short term signal described in this text and the hand drawn blue line represents the possible third signal discovered when data were reprocessed with GOA-II (ver. 6.2).

MVO1 Residual Coordinate changes - IGS08 stacovs used AMB

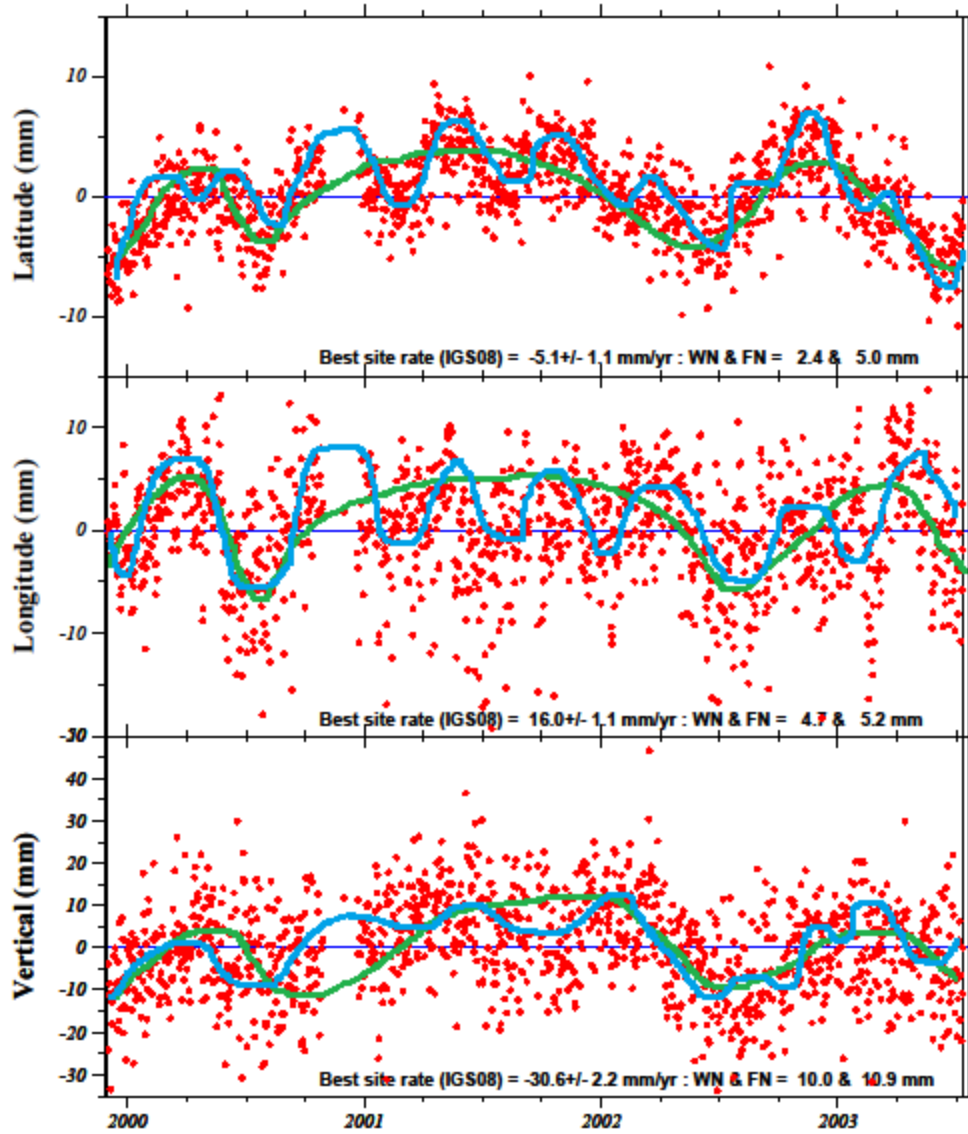


Figure 34 Possible Third Deformation Signal (2)

The third signal that is superimposed on top of short term signal, the hand drawn green line represents the short term signal described in this text. The hand drawn blue represents the possible third signal discovered when data were reprocessed with GOA-II (ver. 6.2).

MVO1 Residual Coordinate changes - IGS08 stacovs used AMB

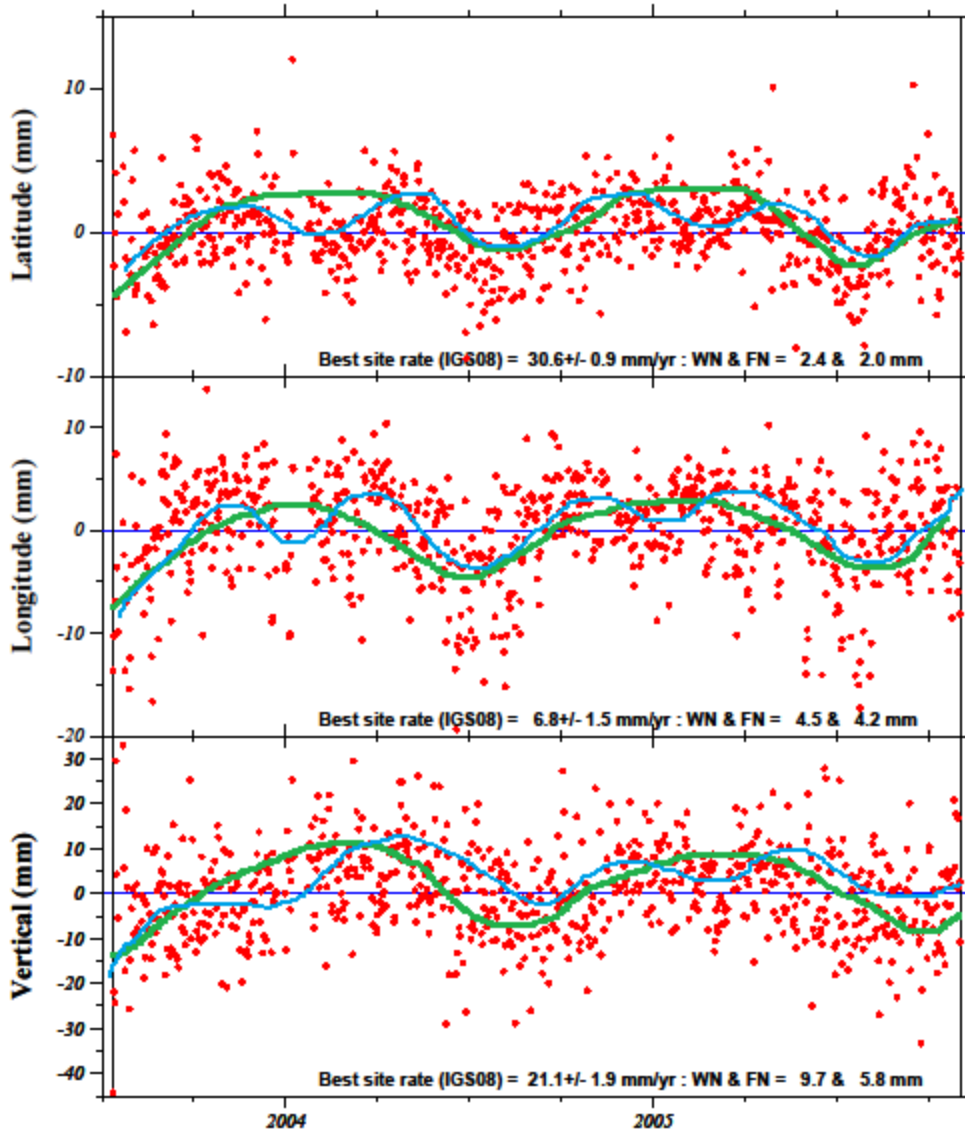
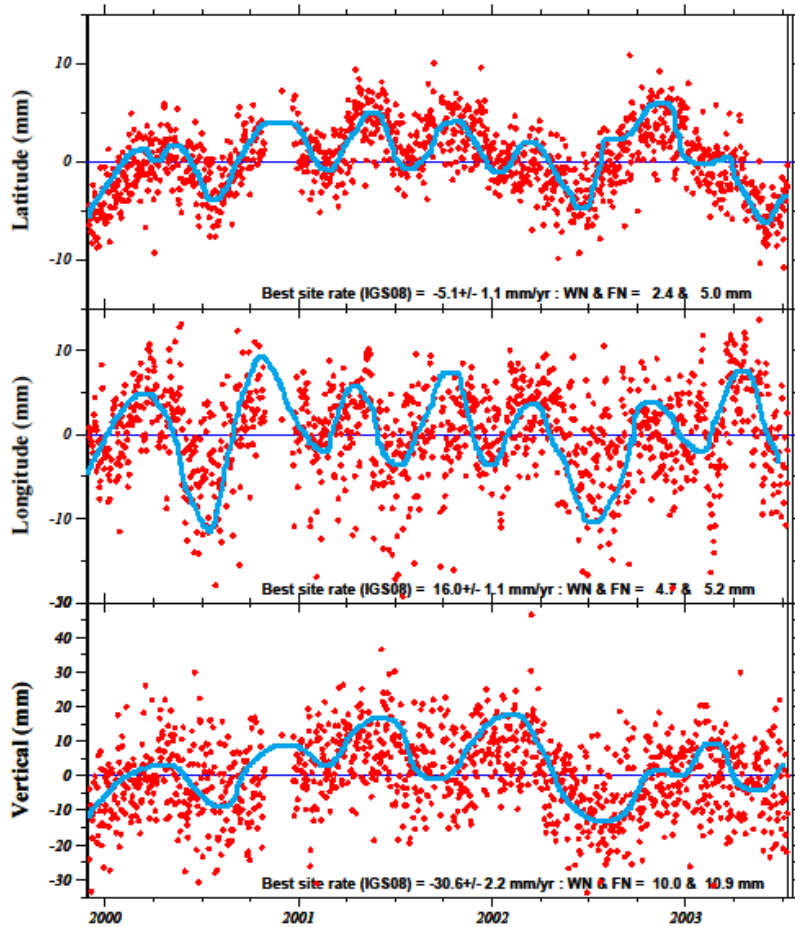


Figure 35 Possible Third Deformation Signal showing little variation

The possible third signal that is superimposed on top of short term signal, the hand drawn green line is the short term signal described in this text. The hand drawn blue is the possible third signal discovered when data were reprocessed with GOA-II (ver. 6.2) This epoch the new signal shows only a small amount of variation from the longer signal.

MVO1 Residual Coordinate changes - IGS08 stacovs used AMB



BGGY Residual Coordinate changes - IGS08 stacovs used AMB

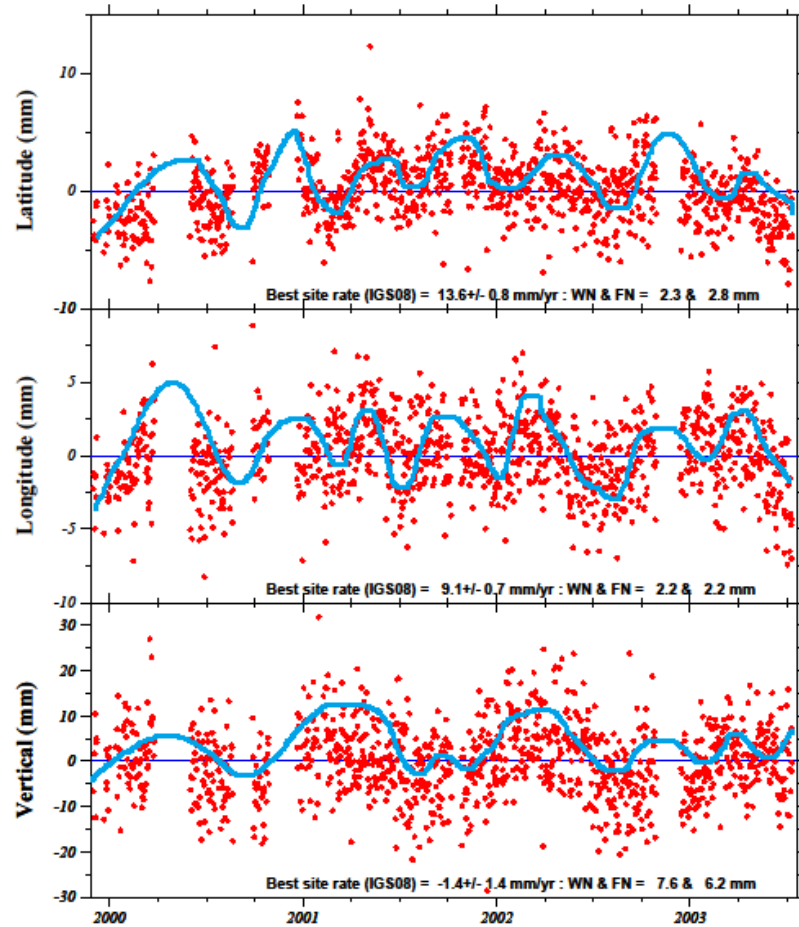


Figure 36 Possible third signal at MVO1 correlated with signal at BGGY

Hand drawn blue line represents possible third signal seen at MVO1 & similar signal noted at BGGY site, data reprocessed with GOA-II (ver. 6.2).

Chapter 5

Conclusions

Short term deformations signals are often overlooked when trying to get a complete, large scale idea of the workings of a volcano. However, when GPS data are processed with the latest, most advanced software, a greater understanding of the daily activity that is occurring at a volcano may be obtained. Reprocessing the Soufriere Hills Volcano GPS data for the two continuous sites HERM and MVO1 has yielded astonishing results. The greater precision of daily point positions has illuminated not only a high frequency, short term surface deformation signal that is super imposed on top of the long term deformation signal but also allowed for the surface deformations recorded by GPS to be correlated with known events that have occurred on SHV. The short term signal shows that even small events, those lasting for days to a few weeks are seen to have a recordable effect on the edifice of the volcano. Knowing how the volcanic edifice reacts to even small loading or unloading events could help with volcanic hazard planning and potentially save lives some day.

The reprocessing of the data, with the extension of the time series have shown that surface deformation at SHV may in fact be damping down and be nearing the end of this long lived eruption cycle, to yet again go dormant. If the flux rate for magma into the chambers is indeed decreasing significantly, and if it follows the Denlinger and Hoblitt (1999) model, the volcano is likely to show little to no oscillations in the future with new dome growth and repose periods. However, if the third cycle is in fact still in the inflation period and has yet to undergo a true deflation period, this volcano may be active for years to come. Continued analysis of the ongoing recording of GPS data from this volcano is vital to trying to understand if and when activity here may cease. Knowledge of this kind can help in future eruptions to determine when an area might be potentially safe for either habitation to return and/or clean up or recovery to take place. So much more study can still be done on Soufriere Hills Volcano, using the data already collected more intense modeling of the "hitch" that occurs during the inflations and deflation periods in each cycle could be done to try and determine causation. Is this caused by a new pulse of magma being injected into an upper magma chamber from a lower one? What other knowledge could

be gained from modeling the data collected here? Reprocessing of the other continuous GPS sites located around SHV may also garner greater knowledge of this volcano's internal workings.

Modeling the HERM site with a proposed dike showed that it is possible that the portion of the edifice that the HERM site is situated on is indeed decoupled with the rest of the volcano. As magma is moves up through the conduit from the magmatic sources, and the dike is filled and opened, it pushes the block of land further and further from the rest of the edifice, thus causing it to act as a unique entity and show an all together different deformation pattern than the rest of SHV. More modeling of this process should be done to determine if the inflation of the proposed magmatic sources beneath the SHV would cause more deformation to occur if the magmatic source and dike were to simultaneously inflate and open. It is likely that this is the case however, with the magmatic sources being modeled at a depth of ~5-6 km below the vent of SHV it may in fact have only a small affect on the HERM site.

With the discovery of a possible third deformation signal at SHV, that seems to be closely mirrored by the BGGY site on Antigua, has opened an even greater opportunity to study and continue modeling this remarkable volcano as well other sites in the area and could lead to an even greater understanding of the movement of the Caribbean plate. If the data could be obtained from the MVO from January 2011 to present, much more knowledge could be obtained about the complete eruption cycle of an andesitic volcano, and thus could lead to a greater understanding of this type of magmatic system as a whole. With a better understanding of how a long lived andesitic eruption may act it is feasible that strategic planning for other systems similar to SHV around the world could benefit from this knowledge and less lives be lost.

Appendix A
GOA-II (Ver. 6.1.2) Time Series

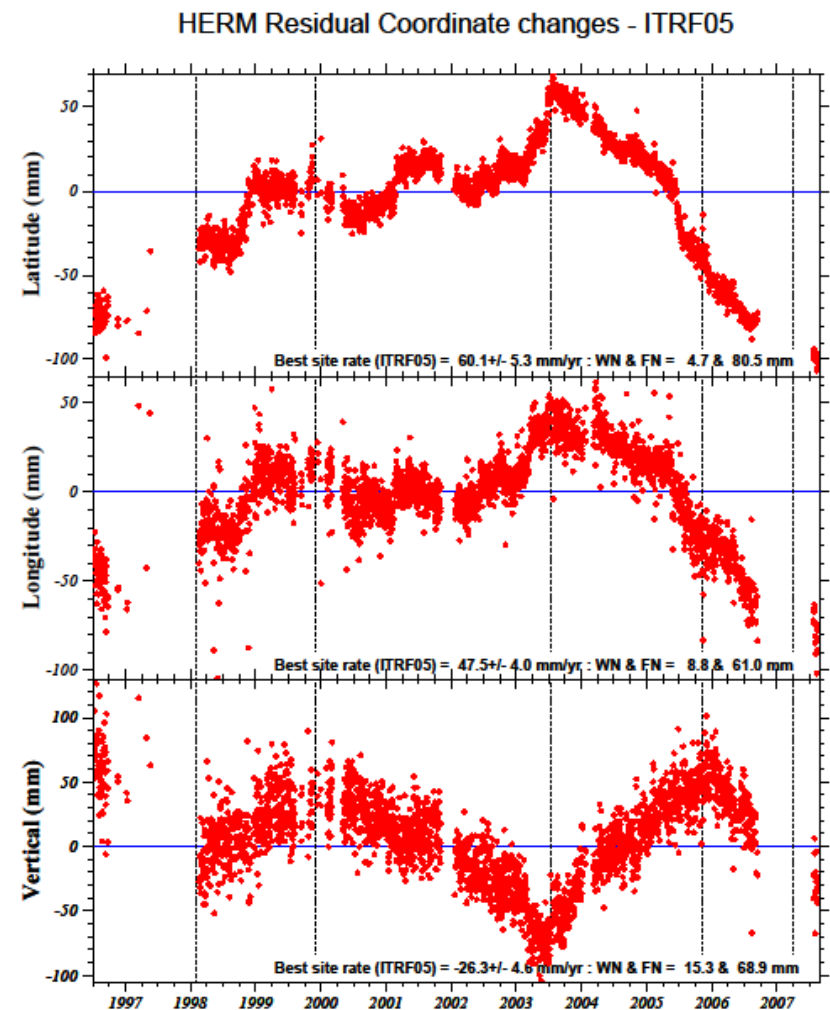
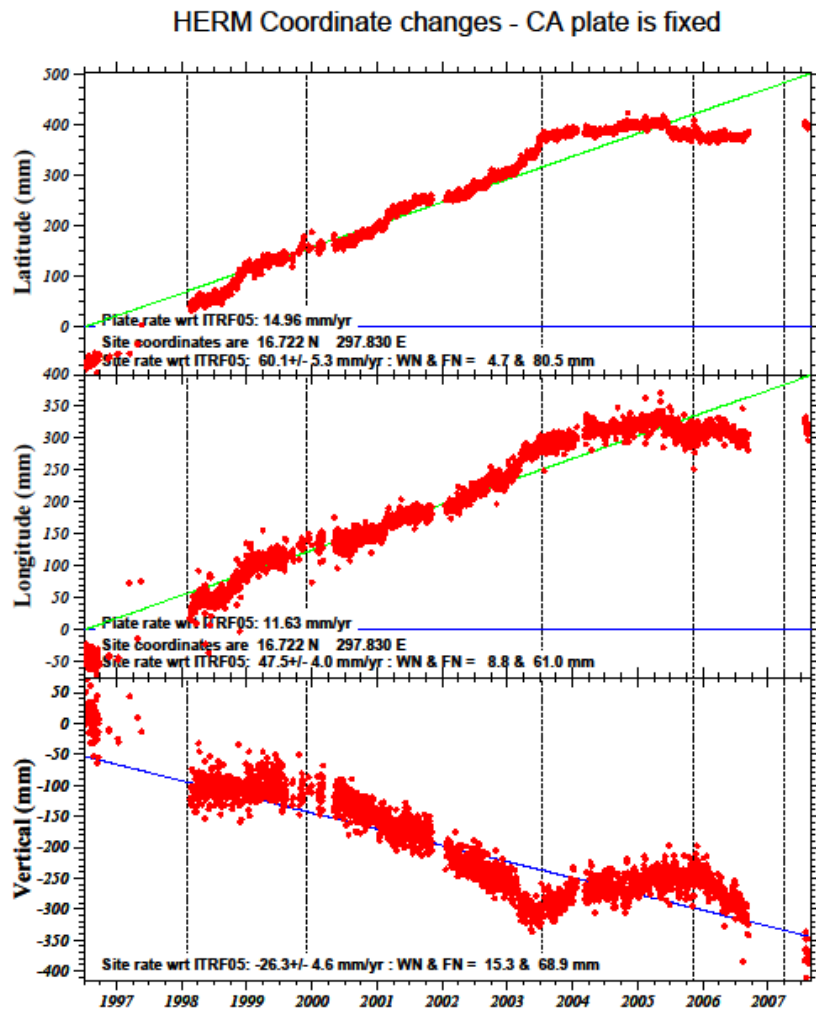
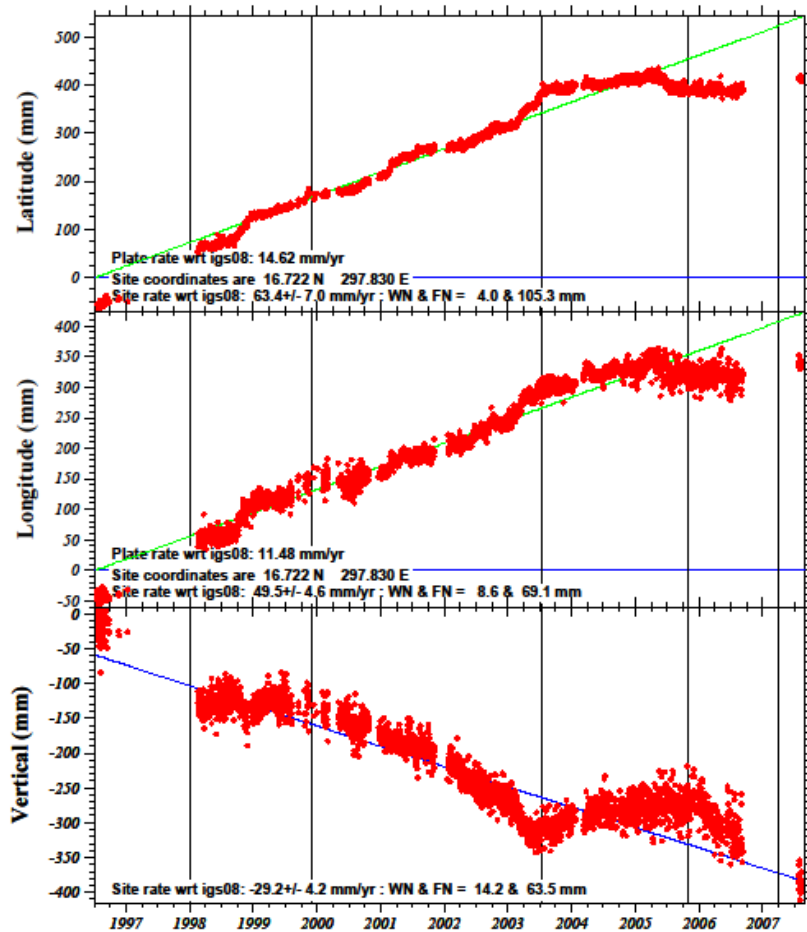


Figure 37 HERM time series in GOA-II (ver. 4.0).

Red dots are UTC daily position solutions. The blue lines are the predicted Caribbean plate rates in ITRF05 held fixed (horizontal). The green lines are the least squares best fit site rates in IGS08. WN = white noise, FN = flicker noise

HERM Coordinate changes - CA plate is fixed



HERM Residual Coordinate changes - igs08

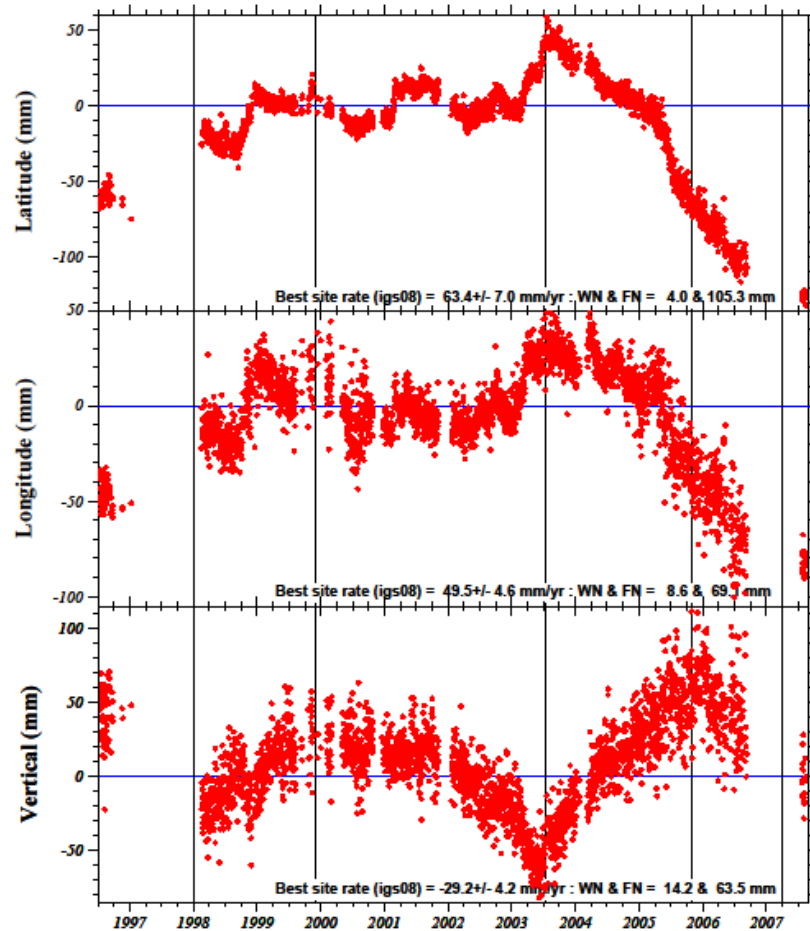
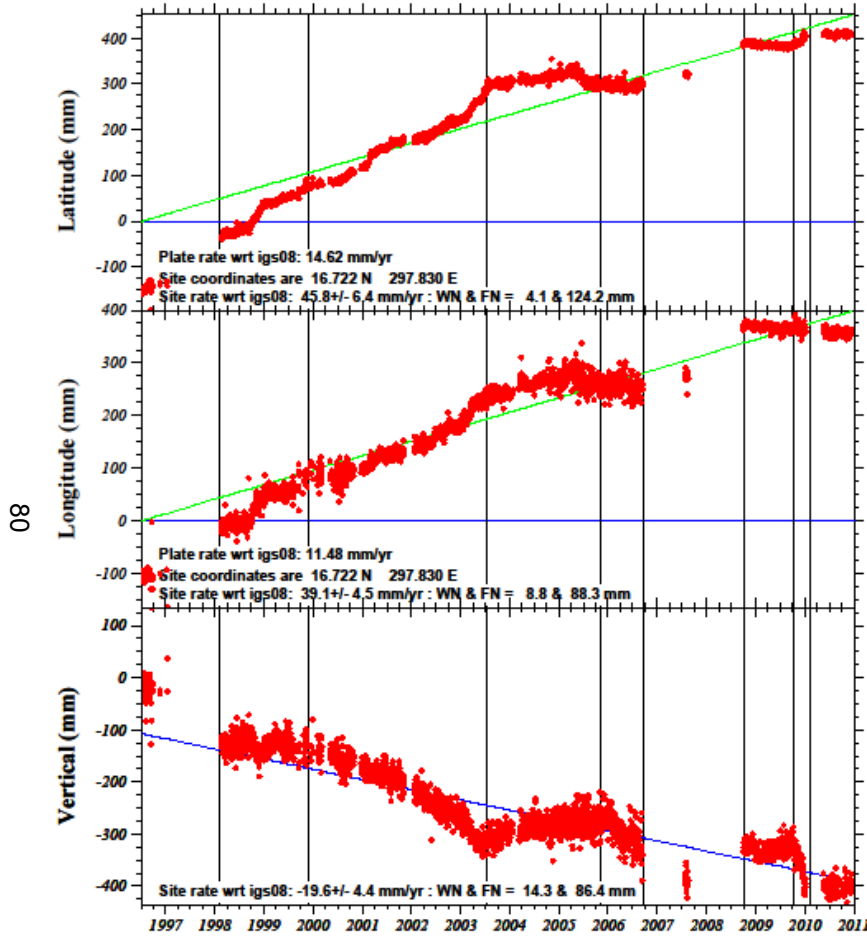


Figure 38 HERM time series processed with GOA-II (v. 6.1.2).

Red dots are UTC daily position solutions. The blue lines are the predicted Caribbean plate rates in IGS08 held fixed (horizontal). The green lines are the least squares best fit site rates in IGS08. WN = white noise, FN = flicker noise.

HERM Coordinate changes - CA plate is fixed



HERM Residual Coordinate changes - igs08

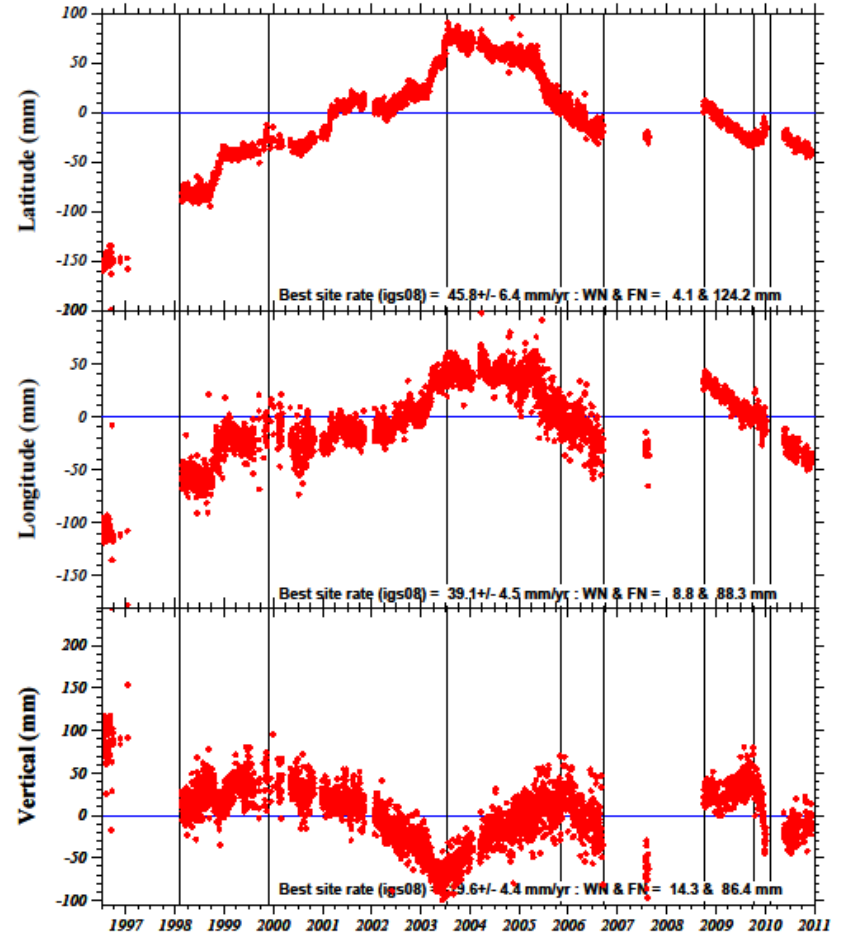
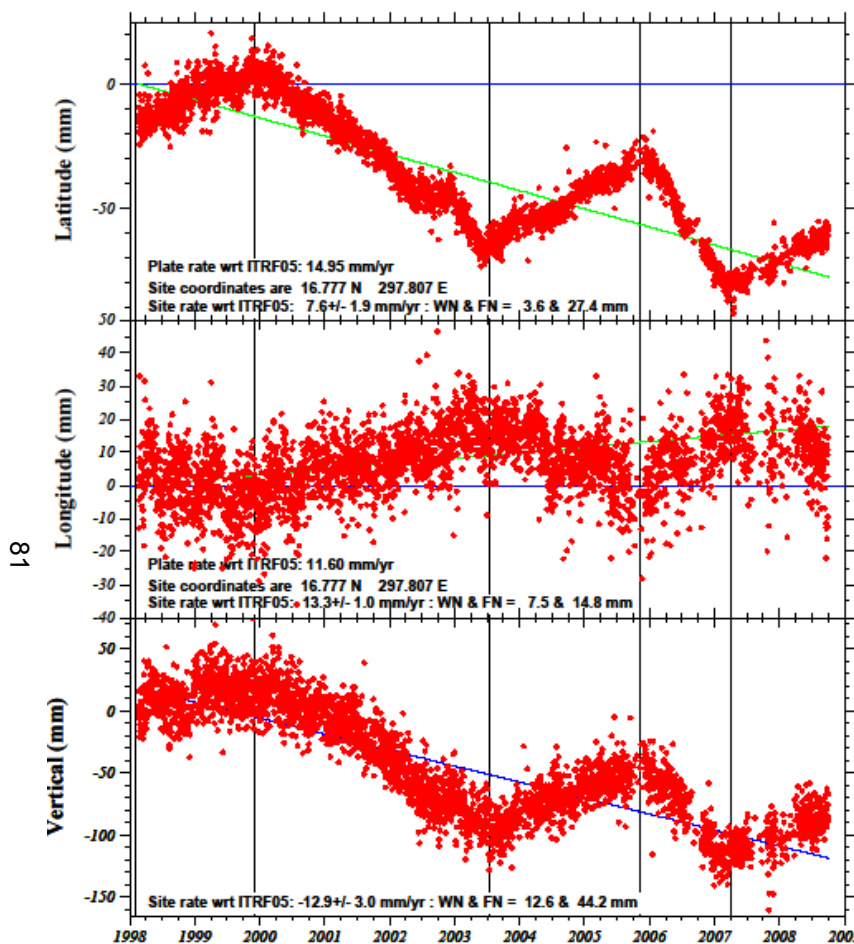


Figure 39 Extended HERM time series reprocessed with GOA-II (v. 6.1.2).

Red dots are UTC daily position solutions. The blue lines are the predicted Caribbean plate rates in IGS08 held fixed (horizontal). The green lines are the least squares best fit site rates in IGS08. WN = white noise, FN = flicker noise. The first line after the large break in data from (late 2006 – Oct. 3, 2008) represents a manual alteration to the data to fix an offset due to an antenna change.

MVO1 Coordinate changes - CA plate is fixed



MVO1 Residual Coordinate changes - ITRF05

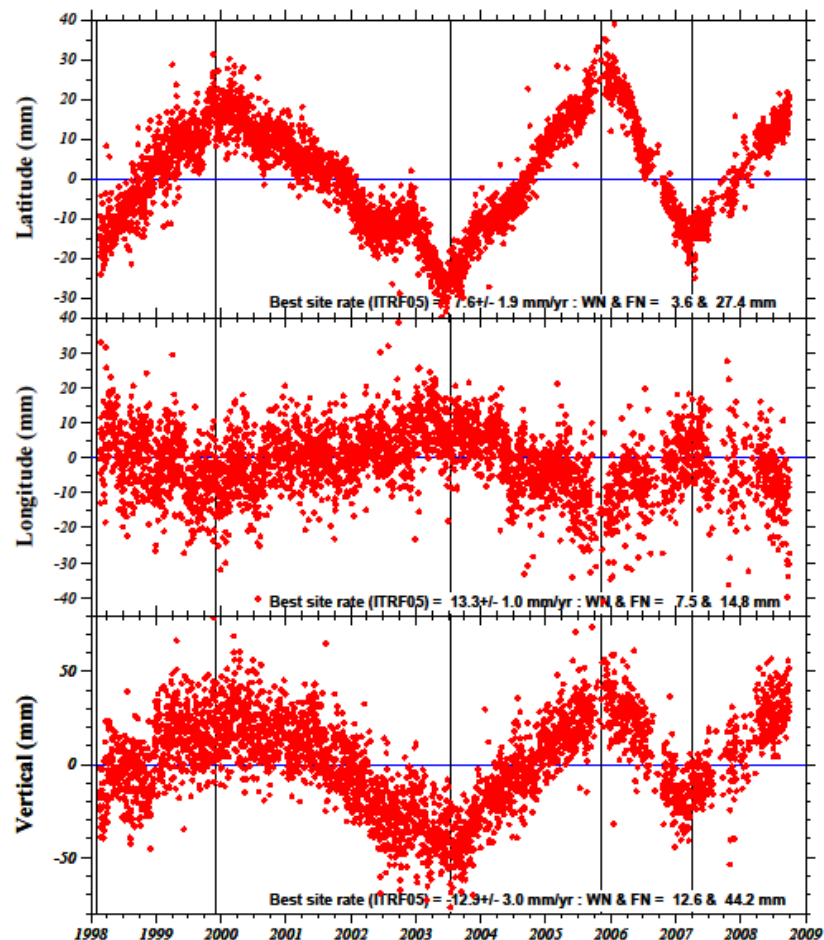
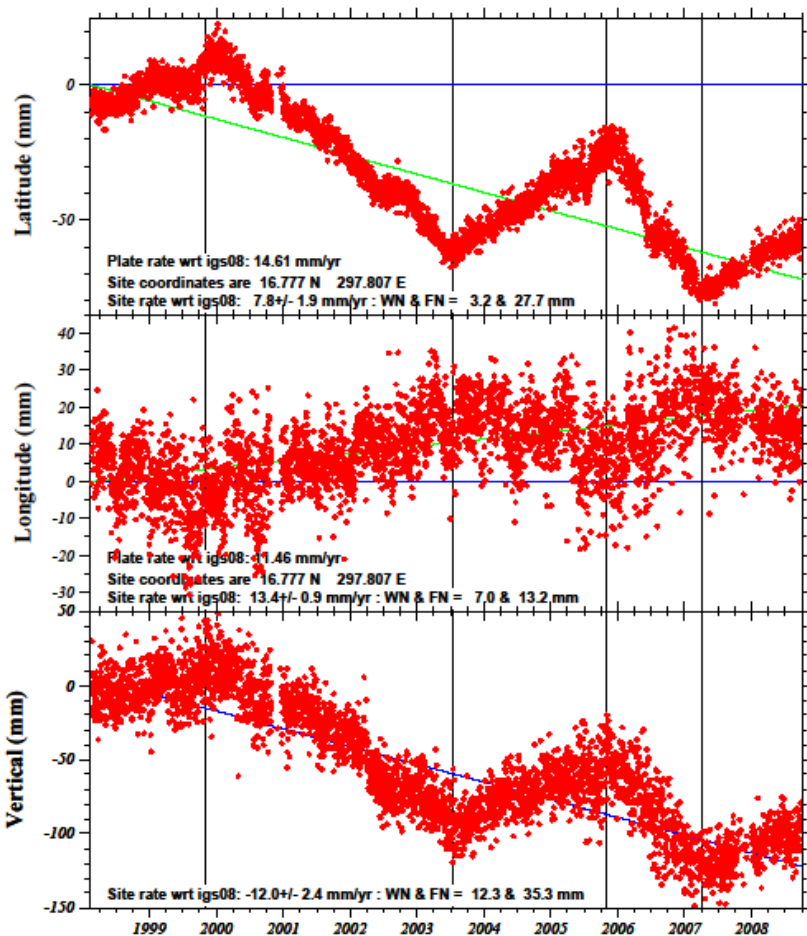


Figure 40 MVO1 time series processed in GOA-II (ver. 4.0).

Red dots are UTC daily position solutions. The blue lines are the predicted Caribbean plate rates in ITRF05 held fixed (horizontal). The green lines are the least squares best fit site rates in IGS08. WN = white noise, FN = flicker noise.

MVO1 Coordinate changes - CA plate is fixed



MVO1 Residual Coordinate changes - igs08

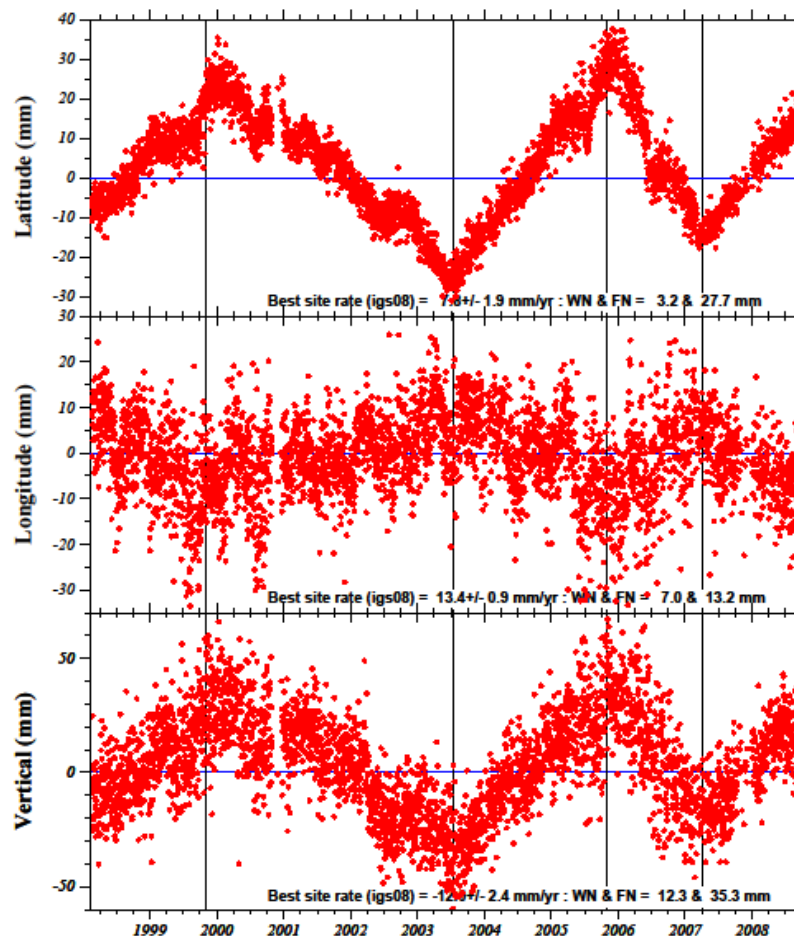
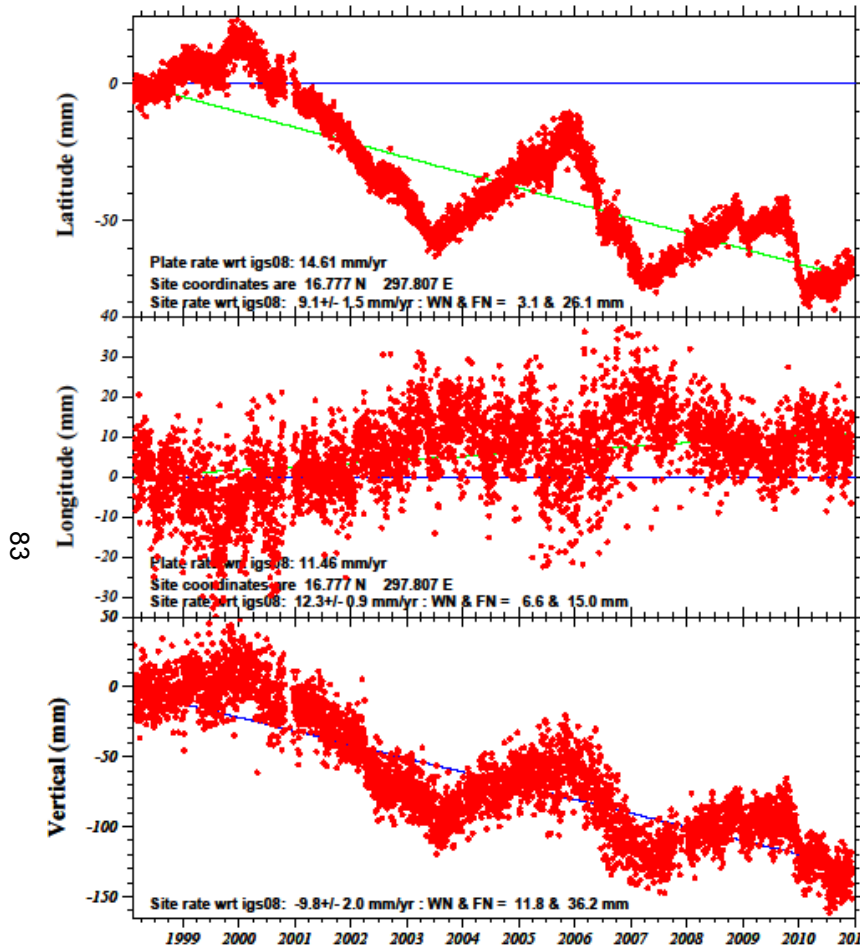


Figure 41 MVO1 time series reprocessed in GOA-II (ver. 6.1.2).

Red dots are UTC daily position solutions. The blue lines are the predicted Caribbean plate rates in IGS08 held fixed (horizontal). The green lines are the least squares best fit site rates in IGS08. WN = white noise, FN = flicker noise.

MVO1 Coordinate changes - CA plate is fixed



MVO1 Residual Coordinate changes - igs08

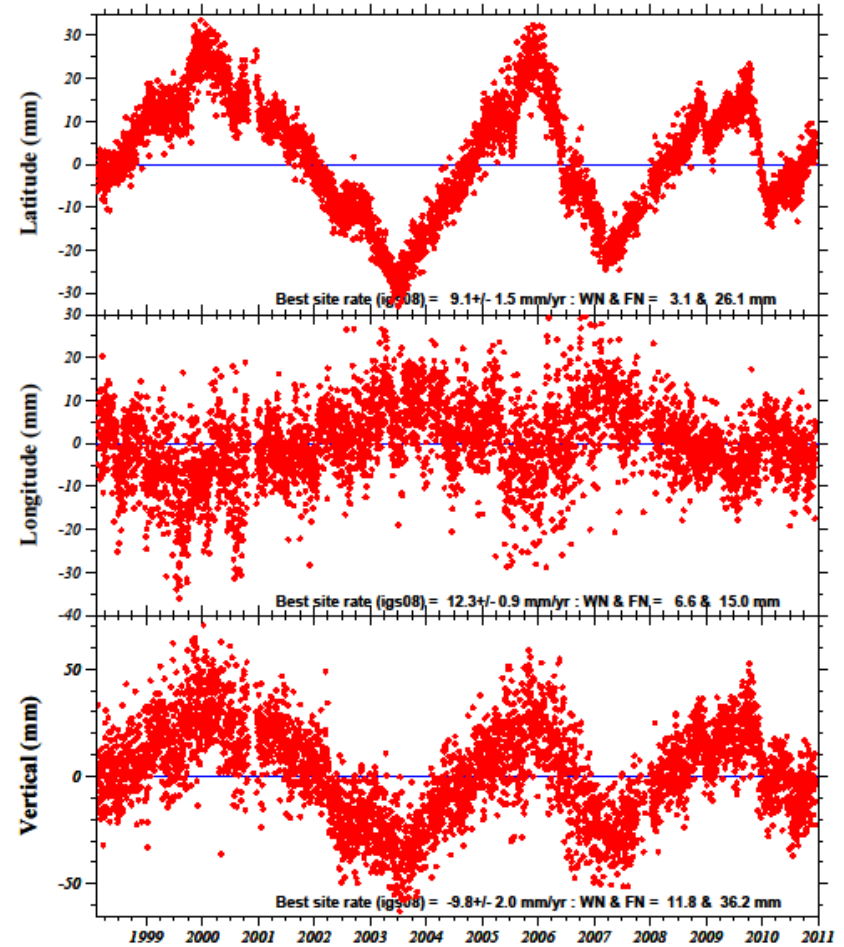


Figure 42 Extended time series for continuous site MVO1 site reprocessed using GIPSY (ver. 6.1.2).

Red dots are UTC daily position solutions. The blue lines are the predicted Caribbean plate rates in IGS08 held fixed (horizontal). The green lines are the least squares best fit site rates in IGS08. WN = white noise, FN = flicker noise. The last dotted line in the vertical component presents a manual alteration to the data to fix an offset due to an antenna change.

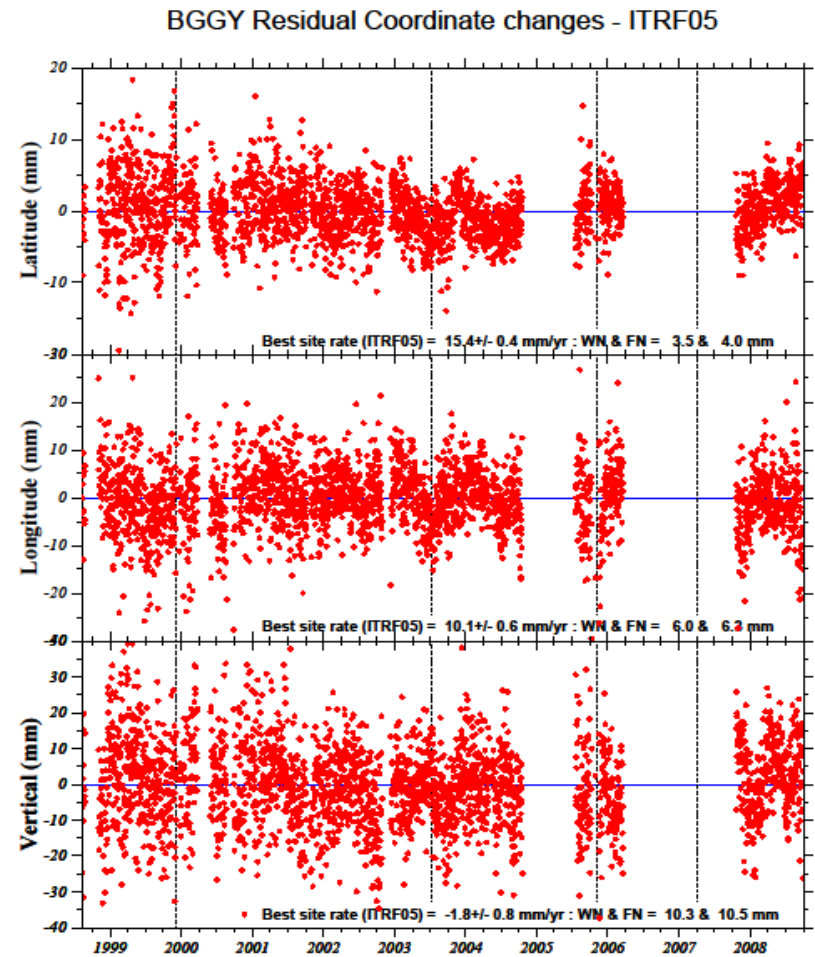
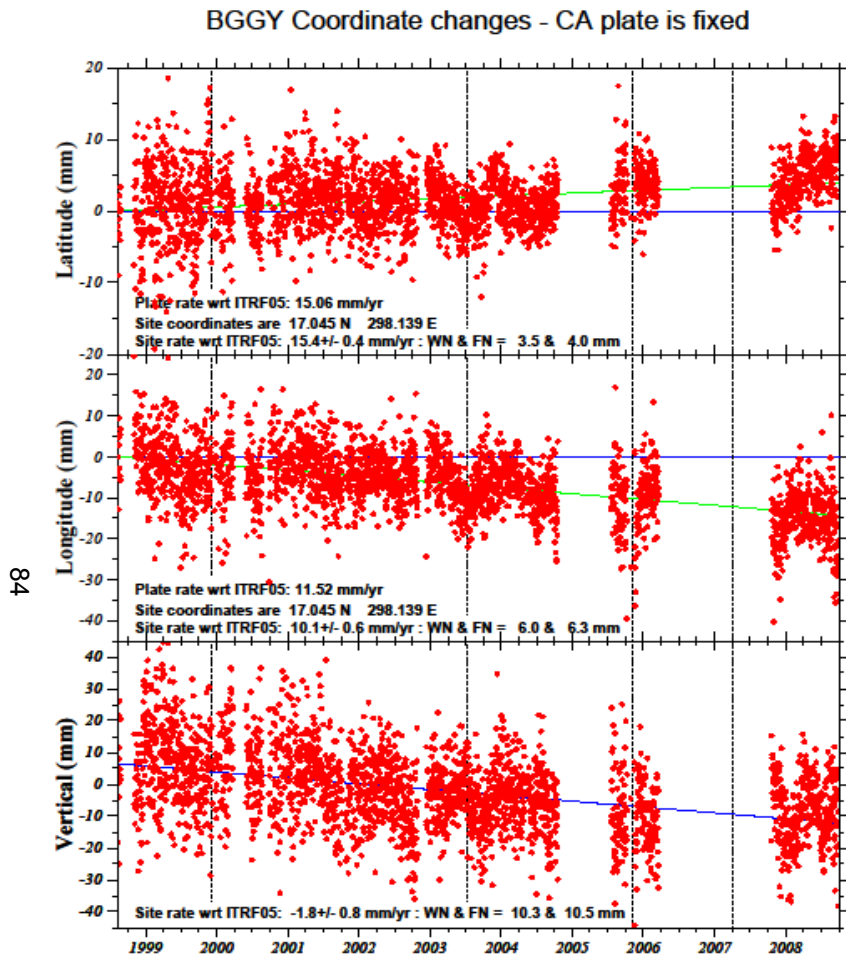
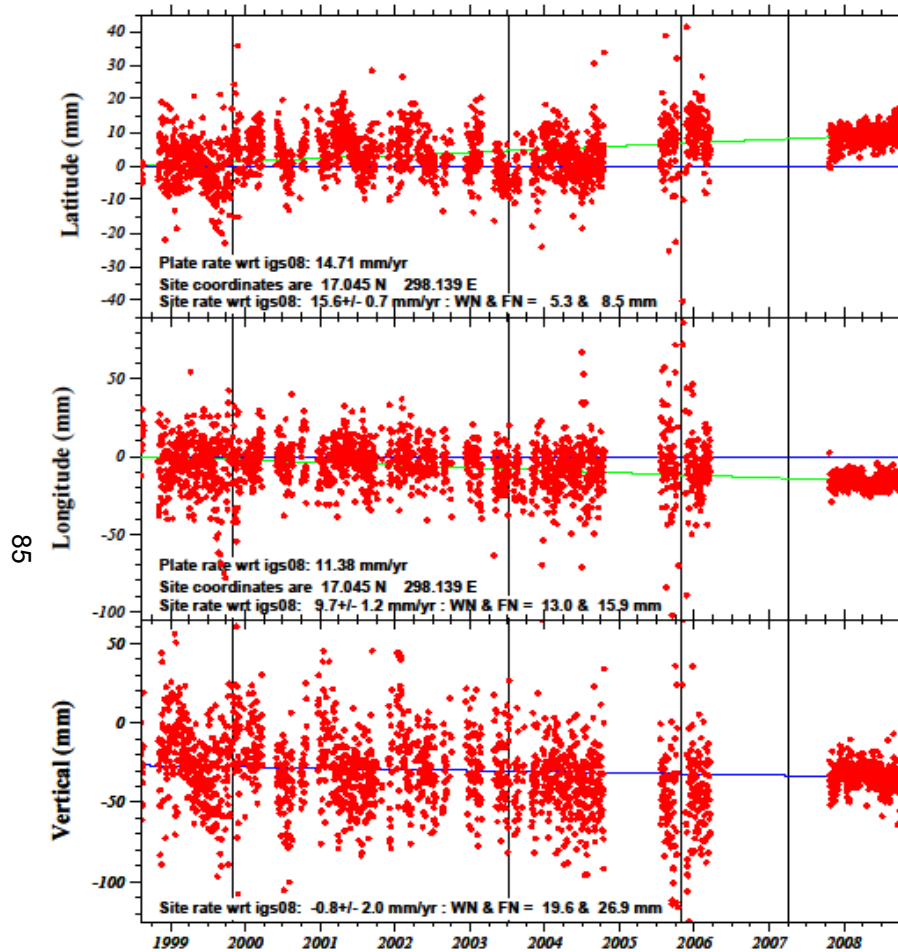


Figure 43 Time series for continuous site BGGY site reprocessed using GIPSY (ver. 4.0).

Red dots are UTC daily position solutions. The blue lines are the predicted Caribbean plate rates in IGS08 held fixed (horizontal). The green lines are the least squares best fit site rates in IGS08. WN = white noise, FN = flicker noise.

BGGY Coordinate changes - CA plate is fixed



BGGY Residual Coordinate changes - igs08

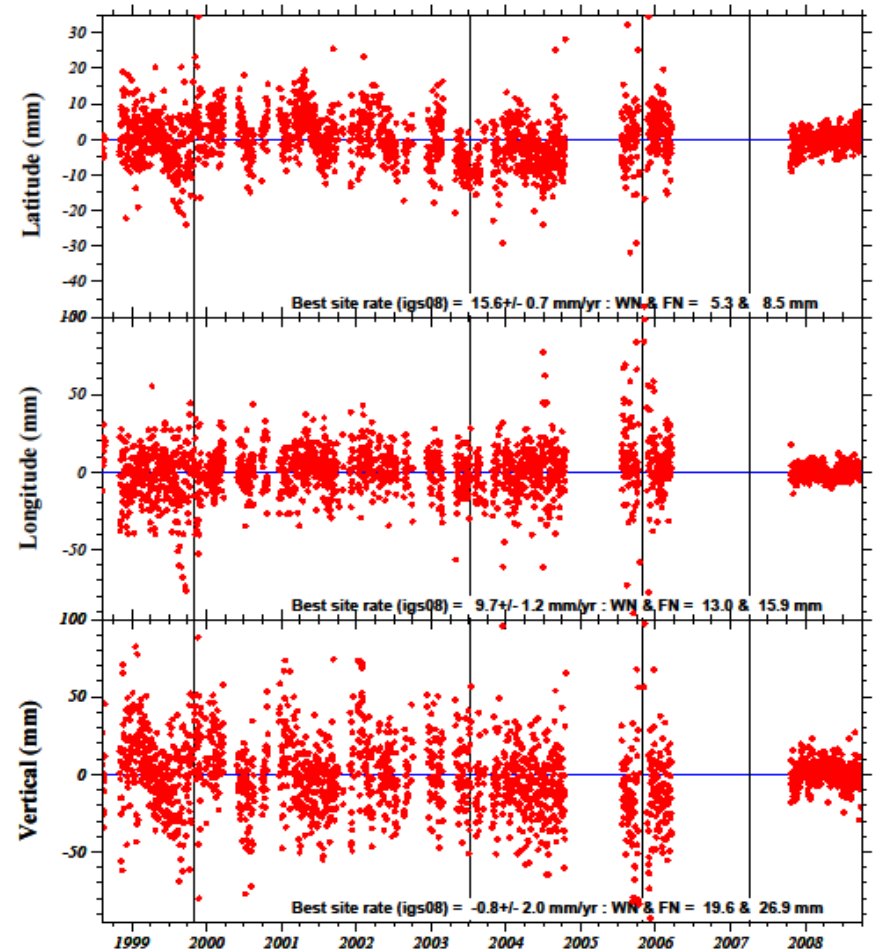


Figure 44 Time series for continuous site BGGY site reprocessed using GIPSY (ver. 6.1.2).

Red dots are UTC daily position solutions. The blue lines are the predicted Caribbean plate rates in IGS08 held fixed (horizontal). The green lines are the least squares best fit site rates in IGS08. WN = white noise, FN = flicker noise.

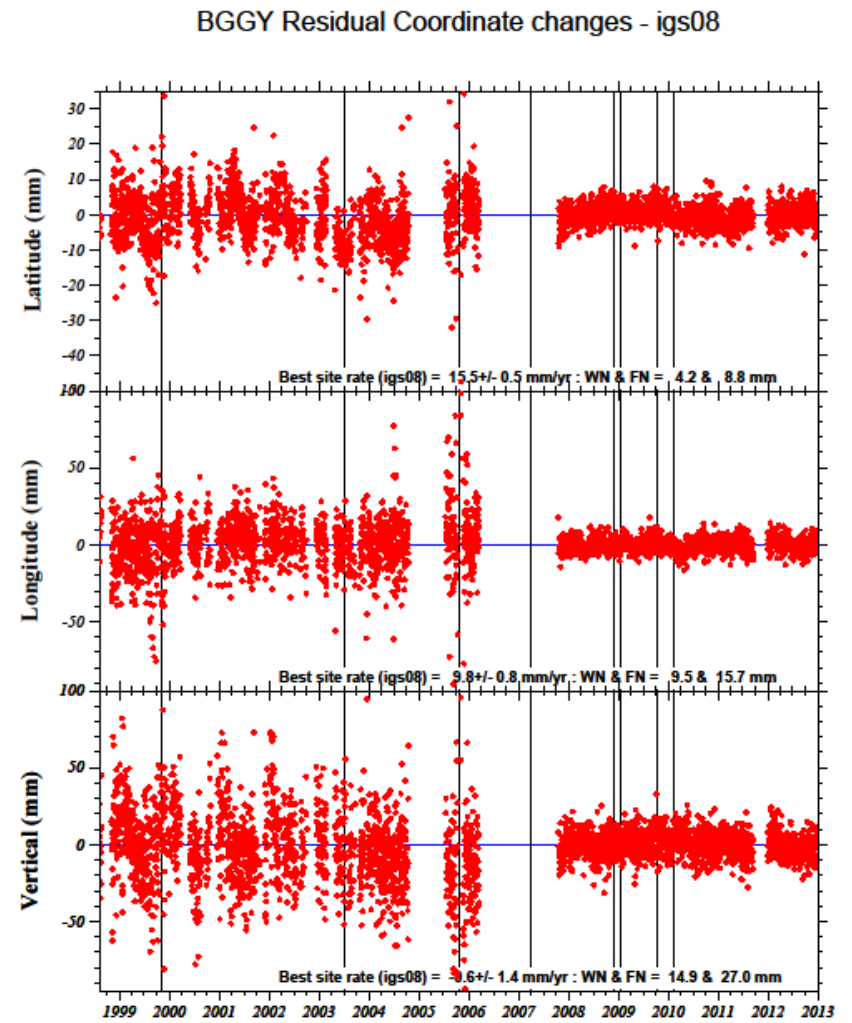
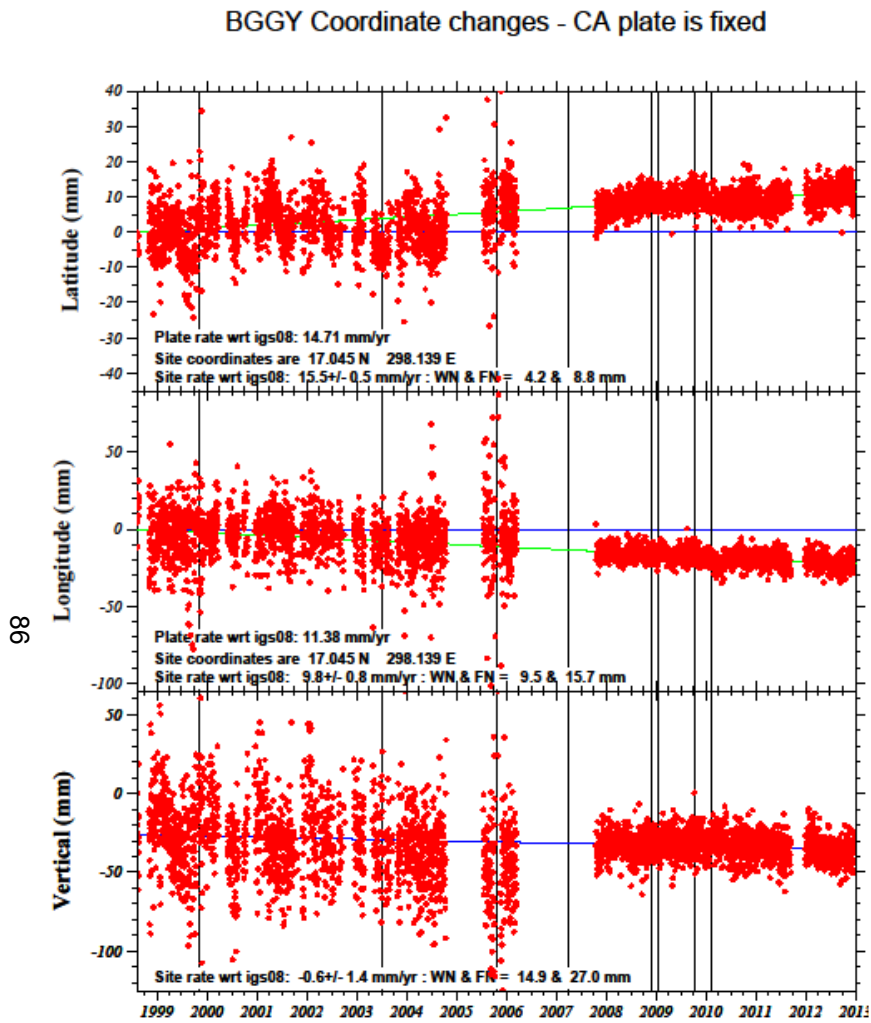


Figure 45 Extended time series for continuous site BGGY site reprocessed using GIPSY (ver. 6.1.2).

Red dots are UTC daily position solutions. The blue lines are the predicted Caribbean plate rates in IGS08 held fixed (horizontal). The green lines are the least squares best fit site rates in IGS08. WN = white noise, FN = flicker noise.

Appendix B
GOA-II (Ver. 6.2) Time Series

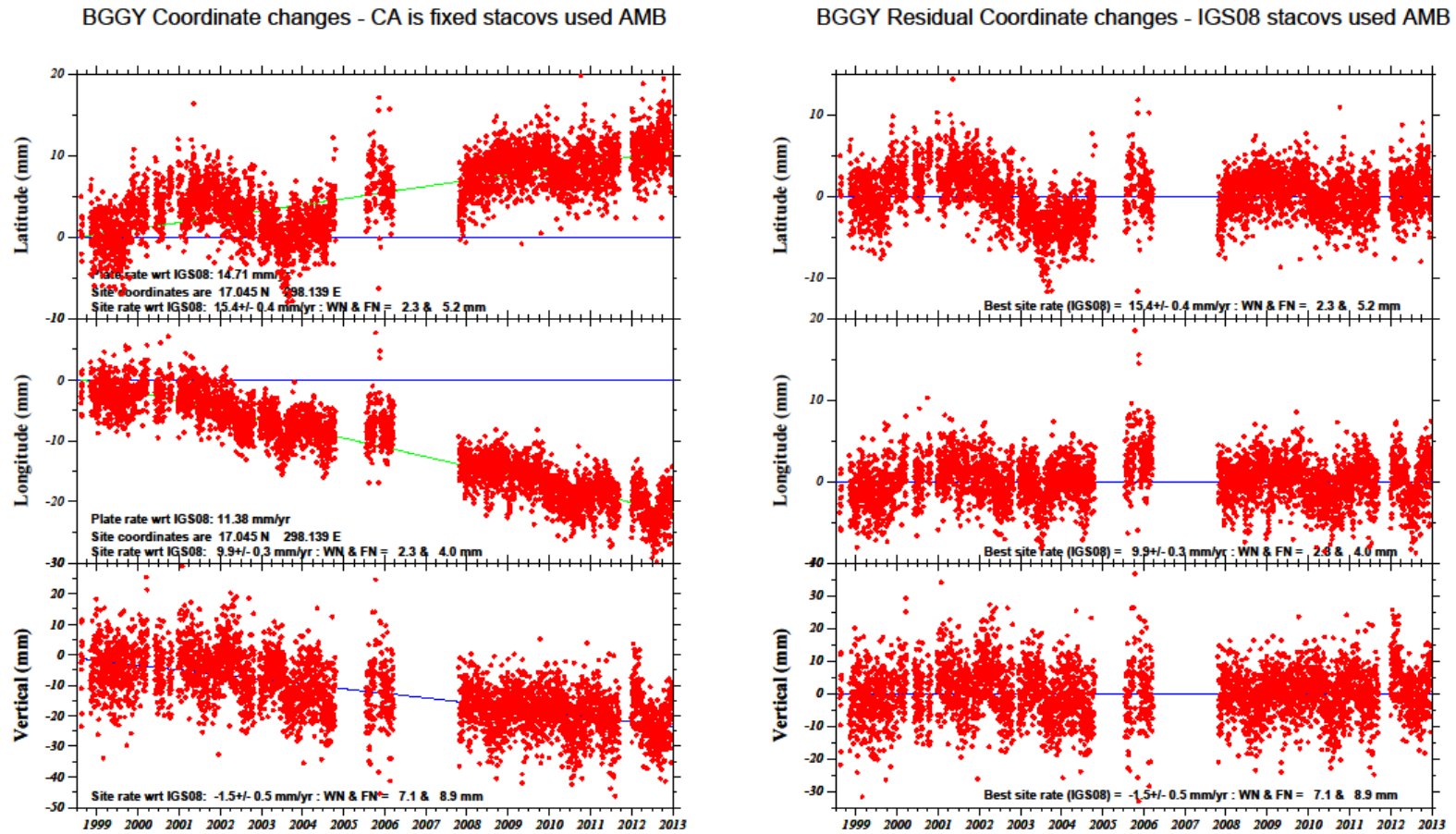


Figure 46 BGGY time series in GOA-II (ver. 6.2) with ambiguities

Red dots are UTC daily position solutions. The blue lines are the predicted Caribbean plate rates in IGS08 held fixed (horizontal). The green lines are the least squares best fit site rates in IGS08. WN = white noise, FN = flicker noise

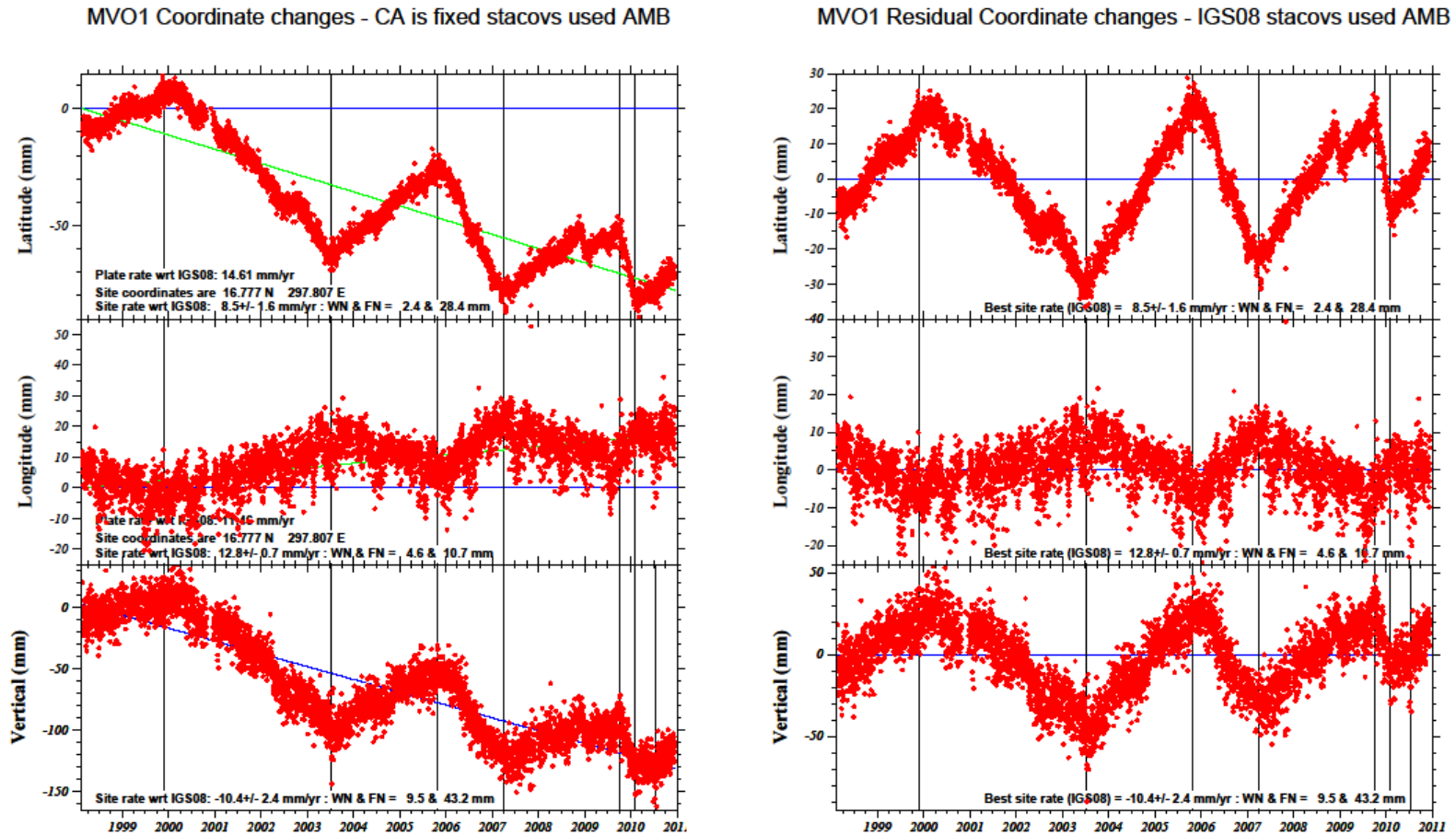
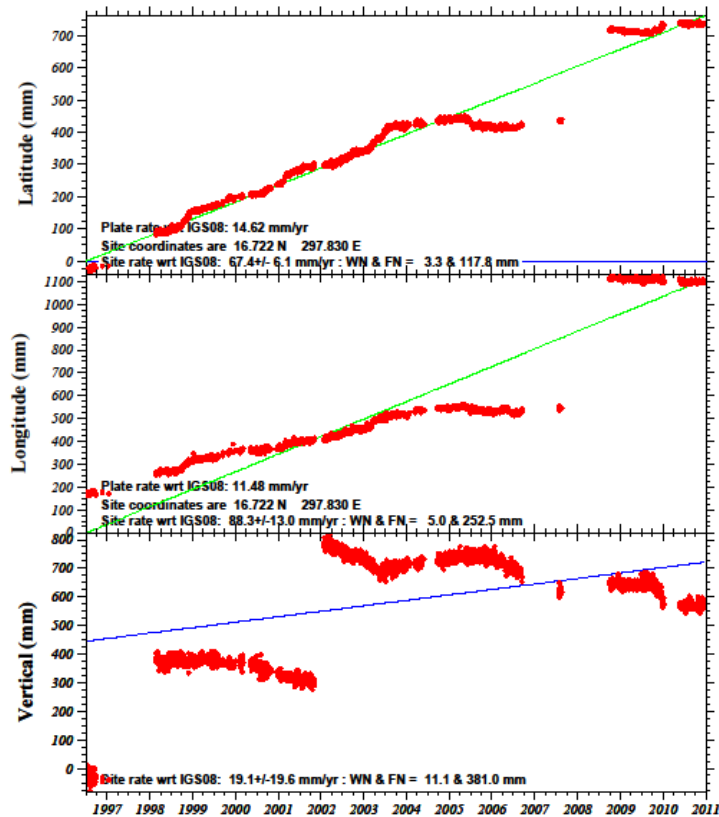


Figure 47 MVO1 time series in GOA-II (ver. 6.2) with ambiguities

Red dots are UTC daily position solutions. The blue lines are the predicted Caribbean plate rates in IGS08 held fixed (horizontal). The green lines are the least squares best fit site rates in IGS08. WN = white noise, FN = flicker noise

HERM Coordinate changes - CA is fixed stacovs used AMB



HERM Residual Coordinate changes - IGS08 stacovs used AMB

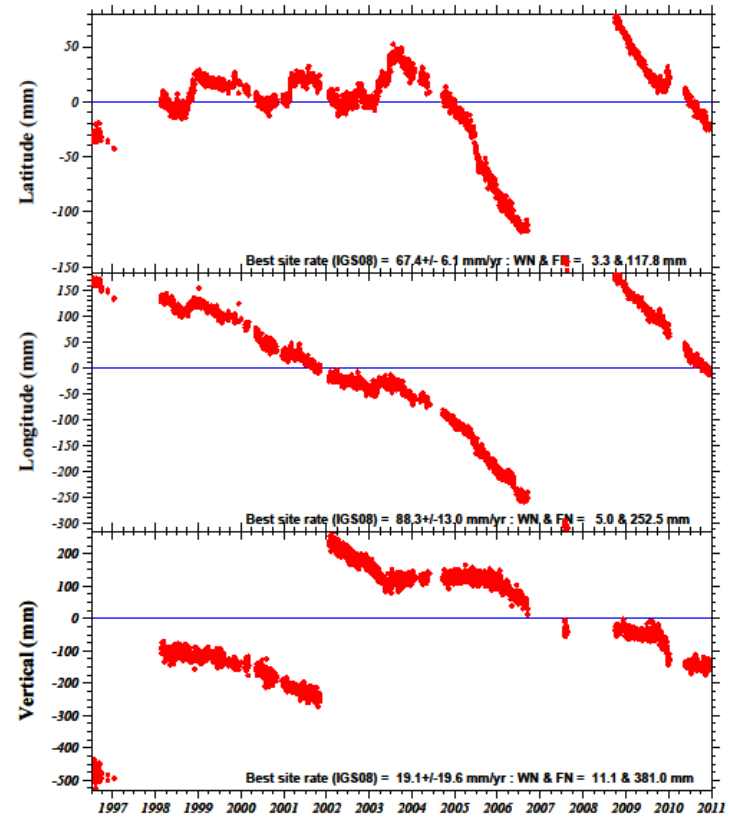


Figure 48 HERM time series in GOA-II (ver. 6.2) with ambiguities

Red dots are UTC daily position solutions. Ignore the offset of the data height, needs to be corrected in the server. Blue lines are predicted Caribbean plate rate, IGS08 held fixed (horizontal). Green line, the least squares best fit site rate, IGS08. WN = white noise, FN = flicker noise.

References

- Altamimi, Z., X. Collilieux, J. Legrand, B. Garayt, and C. Boucher, 2007, ITRF2005: A new release of the International Terrestrial Reference Frame based on time series of station positions and Earth Orientation Parameters, *Journal of Geophysical Research*, 112, B09401, doi:10.1029/2007JB004949.
- Bevington, P.R., 1969, *Data Reduction and Error Analysis for the Physical Sciences*, McGraw-Hill, New York, 336 p.
- Benford, B., C. DeMets, and E. Calais, 2012, GPS estimates of microplate motions, northern Caribbean: evidence for a Hispaniola microplate and implications for earthquake hazard, *Geophysical Journal International*, 191, 481–490, doi: 10.1111/j.1365-246X.2012.05662.x
- Bird, D. E., S. A. Hall, and J. F. Casey, P. S. Milligan, 1993, Interpretation of magnetic anomalies over the Grenada Basin, *Tectonics*, vol.12, p.1267-1279.
- Blewitt, G., 1993, Advances in Global Positioning System technology for geodynamics investigations: 1978-1992, in Smith, D. and D. Turcotte, eds., *Contributions of space geodesy to geodynamics*, *Geodynamics Series*, vol.25, p. 195-213.
- Burke, K. 1988, Tectonic Evolution of the Caribbean, *Annual Review of Earth and Planetary Sciences*, 16, 201-230.
- Demets, C., P. Jansma, G. Mattioli, T. Dixon, F. Farina, R. Bilham, E. Calais, and P. Mann, 2000, GPS geodetic constraints on Caribbean-North American plate motion: Implications for plate rigidity and oblique plate boundary convergence, *Geophysical Research Letters*, vol.27. p. 437-27,440.
- Den Doelder, C. F. J., Koopmans, R. J., Molenaar, J., and Van de Ven, A. A. F., 1998. Comparing the wall slip and the constitutive approach for modeling spurt

- instabilities in polymer melt flows. *Journal of Non-Newtonian Fluid Mechanics*, v. 75, p. 25–41.
- Denlinger R.P., and R. P. Hoblitt, 1999. Cyclic eruptive behavior of silicic volcanoes. *Geology*. Vol. 27, p 459-462
- Desai, S D, Bertiger, W, Haines, B, Harvey, N, Selle, C, Sibthorpe, A, Weiss, J P. 2011 Results from the Reanalysis of Global GPS Data in the IGS08 Reference Frame. Abstract G53B-0904 presented at 2011 Fall Meeting, AGU, San Francisco, Calif., 5-9 Dec.
- Draper, G., T. A. Jackson, S. K. Donovan, 1994. Geological Provinces of the Caribbean Region, in S. K. Donovan and T. A. Jackson (editors), *Caribbean geology: An introduction*, Kingston, Jamaica, University of West Indies Publisher's Association, pp. 3-12.
- Dzurisin, D., 2007, *Volcano Deformation – Geodetic Monitoring Techniques*, Berlin, Springer, Springer-Praxis Books in Geophysical Sciences, 441.
- Elsworth D., Mattioli GS, Taron J, Voight B, Herd R. 2008. Implications of Magma Transfer Between Multiple Reservoirs on Eruption Cycling *Science*. Vol. 322, P. 246-248.
- Estey L.H., and C.M. Meertens, 1999. TEQC: The multi-purpose tool for GPS/GLONASS Data, *GPS Solution*, Vol. 3, No.1, pp. 42-49.
- Fink, L. K. and C. G. A. Harrison, 1972. Paleomagnetic investigations of selected lava units on Puerto Rico: *Caribbean Geological Conference Transactions*, No.6, pp. 669-673.
- Foroozan, R., D. Elsworth, B. Voight, and G.S. Mattioli, 2010. Dual reservoir structure at Soufriere Hills Volcano inferred from continuous GPS observations and

- heterogeneous elastic modeling. *Geophysical Research Letters*. Vol. 37, L00E12, doi: 10.1029/2010GL042511.
- Fox, P. J., and B. C. Heezen, 1975. Geology of the Caribbean Crust, in A.E.M. Nairn, and F. G. Stehli (editors), *The Ocean basins and margins*, v.3. The Caribbean and the Gulf of Mexico, New York, Plenum Press, pp. 421-466.
- Geshi N, Kusumoto S, and Gudmundsson A. 2010. Geometric differences between non-feeder and feeder dikes. *Geology*. Vol. 38, No. 3, p. 195-198. Doi: 10.1130/G30350.1
- Ghosh N., S. A. Hall, J.F. Casey, K. Burke, 1994. Magnetic stripes of the Caribbean ocean floor: formation at the Farallon-Phoenix-Pacific triple junction: *EOS*, v. 75, pp. 594.
- GPSY 5.0 Release Notes, Jet Propulsion Laboratory, California Institute of Technology, June 2, 2008
- GPSY 6.1.2 Release Notes, Jet Propulsion Laboratory, California Institute of Technology, January 18, 2012.
- Harford, C.L., M.S. Pringle, R.S.J. Sparks, and S.R. young (2002), The volcanic evolution of Montserrat using 40AR/39AR geochronology, Druitt, T.H. and Kokelaar, B.P., eds. *Geological Society Memior No 21: The Eruption of Soufriere Hill Volcano, Montserrat, from 1995-1999*, London, 93-133.
- Hautmann, S, Gottsmann J, Sparks RSJ, Mattioli GS, Sacks IS, and Strutt MH. 2010. Effect of mechanical heterogeneity in arc crust on volcano deformation with application to Soufrière Hills Volcano, Montserrat, West Indies. *Journal of Geophysical Research*. Vol. 115. B09203. Doi: 10.1029/2009JB006909
- Introduction to gd2p.pl (GPS Data 2 Position), Jet Propulsion Laboratory, California Institute of Technology, GPSY User Group Meeting/Class, December 14, 2008

- Lichten, S. and J. Border, 1987. Strategies for high-precision global positioning system orbit determination, *Journal of Geophysical Research*, vol. 92, pp. 12751-12762.
- Lin, J. and R.S. Stein (2004), Stress triggering in thrust and subduction earthquakes, and stress interaction between the southern San Andreas and nearby thrust and strike-slip faults, *Journal of Geophysical Research*. 109, B02303, doi:10.1029/2003JB002607.
- Lindsay, J., Robertson, R., Shepherd, J. and Ali, S. (Editors), 2005. Volcanic Hazard Atlas of the Lesser Antilles. Seismic Research Unit, University of the West Indies, St. Augustine, 279 pp.
- MacGregor, A.G. 1938. The Royal Society expedition to Montserrat, B.W.I. The volcanic history and petrology of Montserrat with observations on Mt Pele in Martinique. *Philosophical Transactions of the Royal Society*, **B229**, 1-90.
- Mann, P. and K. Burke, 1984. Neotectonics of the Caribbean *Reviews of Geophysical and Space Physics*, v. 22, No. 4, pp. 309-362.
- Mattioli GS, Dixon TH, Farina F, Howell ES, Jansma PE, and Smith AL. 1998. GPS measurement of surface deformation around Soufriere Hills volcano, Montserrat from October 1995 to July 1996. *Geophysical Research Letters*. Vol. 25, No. 18, pg. 3417-3420.
- Mattioli, G.S., S.R. Young, B. Voight, S.J. Sparks, E. Shalev, S. Sacks, P. Malin, A. Linde, W. Johnston, D. Hidayat, D. Elsworth, P. Dunkley, R. Herd, J. Neuberg, G. Norton, and C. Widiwijayanti (2004), Prototype PBO Instrumentation of CALIPSO Project Captures World-Record Lava Dome Collapse on *Montserrat* Volcano, *EOS, Transactions, AGU*, 85 (34),317,323.
- Mattioli, G.S., R.A. Herd, M.H. Strutt, G. Ryan, C. Widiwijayanti, and B. Voight, 2010, Long term surface deformation of Soufriere Hills Volcano, Montserrat from GPS

geodesy: inferences from simple elastic inverse models. GPS Network Topology, Observations, and Processing Supplemental Online Information.

Maury, R.C., G.K. Westbrook, P.E. Baker, P.H. Bouysse, D. Westercamp, 1990. Geology of the Lesser Antilles, *The Geological Society of America The Geology of North America*, Vol. H, The Caribbean Region, pp. 141-163.

Miller, A.D., R.C. Stewart, R.A. White, R. Luckett, B.J. Baptie, W.P. Aspinall, J.L. Latchman, L.L. Lynch, and B. Voight (1998), Seismicity associated with dome growth and collapse at the Soufriere Hills Volcano, Montserrat, *Geophysical Research Letters*, 25,3401-3404.

Molnar, P., and L. R. Sykes, 1969. Tectonics of the Caribbean and Middle American Regions from focal mechanisms and seismicity, *Geological Society of America Bulletin* 59, pp. 801-854.

Montserrat Volcano Observatory, 2013. www.mvo.ms.

Norton, G.E., Watts, R.B., Voight, B., Mattioli, G., Herd, R.A., Young, S.R., Aspinall, W.P., Bonadonna, C., Baptie, B., Edmonds, M., Harford, C.L., Jolly, A.D., Loughlin, S.C., Luckett, R., and R.S.J. Sparks, 2002, Pyroclastic flow and explosive activity of the lava dome of Soufriere Hills volcano, Montserrat, during a period of virtually no magma extrusion (March 1998 to November 1999), in *The Eruption of Soufriere Hills Volcano, from 1995 to 1999, Geological Society of London, Memoirs*, 21, 467-481.

Odbert, H.M., G.A. Ryan, G.S. Mattioli, S. Hautmann, J. Gottsman, N. Fournier, R. Herd, and A. Linde, 2012, Volcano geodesy at Soufrière Hills Volcano: a review, submitted October 2011 and Revised in 2012 to the *The Eruption of Soufriere Hills Volcano, 15 years on, Geological Society of London, Memoir* (G. Wadge, ed.).

- Owen S. and Segal P. 2000. Rapid deformation of Kilauea Volcano: Global Positioning System measurements between 1990 and 1996. *Journal of Geophysical Research*. Vol 105. No.88. P 18983-18998.
- Roobol M.J. and Smith A.L. 1998. Pyroclastic stratigraphy of the Soufriere Hills Volcano, Montserrat - Implications for the present eruption. *Geophysical Research Letters*, Vol. 25, NO. 18, p. 3393-3396. Doi: 10.1029/98GL00643.
- Segal P and Davis JL. 1997. GPS applications for geodynamics and earthquake studies. *Annual Review Earth Planetary Science*. Vol. 25 p.301–36.
- Shepard, J.B., Tomblin, J.F. and D.A. Woo (1971), Volcano-seismic crisis in Montserrat, West Indies 1966-67, *Bulletin of Volcanology*, 35,143-163.
- Simkin, T., and Siebert, L., 1994, Volcanoes of the World. *Geosciences Press*, Tucson, Arizona, 349 p.
- Smith, A. L., Roobol M, J., Quifiones E., and Mattioli G. S. 1997. Volcanic history of Soufriere Hills, Montserrat, *IA VCEI General Assembly*, Abstracts, Puerto Vallarta, Mexico, p. 109.
- Smith A. L., Roobol M. J., Schellekens J. H., and Mattioli G. S. 2007. Prehistoric Stratigraphy of the Soufriere Hills–South Soufriere Hills Volcanic Complex, Montserrat, West Indies. *The Journal of Geology*, volume 115, p. 115–127.
- Sparks, R.S.J. and S. R. Young, 2002. The Eruption of Soufriere Hills Volcano, Montserrat (1995-1999): Overview of scientific results, Druit, T.H., and Kokelaar, B.P. eds. Geological Society Memior No 21: The Eruption of Soufriere Hills Volcano, Montserrat, from 1995-1999, London, 45-69.
- Sykes, L. R., and M. Ewing, 1965. The seismicity of the Caribbean region, *Journal of Geophysical Review*, v.70, pp. 5065-5074.

- Sykes, L. R., W. R. McCann, A.L. Kafka, 1982. Motion of Caribbean plate during the last 7 Million year and implications for earlier Cenozoic Movements, *Journal of Geophysical Review*, v. 87, No. B13, pp. 10,656-10,676.
- Toda, S., R. S. Stein, K. Richards-Dinger and S. Bozkurt (2005), Forecasting the evolution of seismicity in southern California: Animations built on earthquake stress transfer, *Journal of Geophysical Research.*, B05S16, doi: 10.1029/2004JB003415.
- Tomblin, J. F., 1975. The Lesser Antilles and Aves Ridge: in Nairn, AEM and Stehli, F. G., *The Ocean Basins and Margins, v.3, The Gulf of Mexico and The Caribbean*, pp. 467-500.
- Turner III, Henry L., 2003. Strain/slip partitioning along the Middle American Trench in Nicaragua constrained by GPS geodesy, M.S. August, 2003, University of Arkansas, 91p.
- Voight B, Sparks RSJ, Miller AD, Stewart RC, Hoblitt RP, Clark a, Ewart J, Aspinall WP, Baptie B, Calder ES, Cole P, Druitt TH, Hartford C, Herd RA, Jackson P, Lejeune AM, Lockhart AB, Loughlin SC, Luckett R, Lynch L, Norton GE, Robertson R, Watson IM, Watts R, and Young SR. 1999. Magma flow instability and cyclic activity at Soufriere Hills Volcano, Montserrat, British West Indies *Science*. Vol 283. P 1138-1141.
- Wadge, G. 1994. The Lesser Antilles, in S.K. Donovan, and T.A. Jackson (editors), *Caribbean Geology: An Introduction, Kingston, Jamaica, University of West Indies Publisher's Association*, pp. 167-178.
- Wadge, G., and J. B. Shepherd, 1984. Segmentation of the Lesser Antilles subduction zone, *Earth and Planetary Science Letters*, vol. 71, p. 297-304.

- Wadge G., and M.C. Isaacs (1988), Mapping the Volcanic Hazards from Soufriere Hills Volcano, Montserrat, West Indies using an image processor, *Journal of the Geological Society*, London, 145, 541-555.
- Wadge, G, Mattioli GS, Herd RA. 2006. Ground deformation at Soufriere Hills Volcano, Montserrat during 1998-2000 measured by radar interferometry and GPS. 2006. *Journal of Volcanology and Geothermal Research*. Vol 152. P 157-173.
- Wylie JJ, Voight B, Whitehead JA. 1999. Instability of Magma Flow from Volatile-Dependent Viscosity *Science*. Vol 285. No. 5435. Pp. 1883-1885.
- Young, Simon R; Sparks, R Steven J; Aspinall, Willy P; Lynch, Lloyd L; Miller, Angus D. Overview of the eruption of Soufriere Hills Volcano, Montserrat, 18 July 1995 to December 1997 *Geophysical Research Letters* 25. 18 (Sep 15, 1998): 3389-3392.
- Zumberge, J., M. Heflin, D. Jefferson, M. Watkins, and F. Webb, 1997. Precise point positioning for the efficient and robust analysis of GPS data from large networks: *Journal of Geophysical Research*, vol. 102, p. 5005-5017.

Biographical Information

Erin Elizabeth McPherson is non-traditional student who returned to school after starting a family. She has been married for over ten years to her wonderful husband Mark and is raising two wonderful boys while continuing her schooling. Erin received her Bachelor of Science in Geology from the University of Texas at Arlington in 2011, her Masters in Geology in 2013, and looks forward to earning her PhD in Geology in the near future.

Erin's ultimate goal is to teach Geology at a University and share her love for this amazing science with future generations to come. Erin's research interests lie in many areas of geology but her true passion is micropaleontology and bio-stratigraphy. She hopes to one day teach invertebrate paleontology like her mentors, Drs. Merlynd and Galina Nestell.

Erin's other interests include, reading, drawing, horseback riding, and she has an avid love for animals. She hopes to one day soon, once again have enough time to enjoy those other interests, when schooling becomes less time consuming.